Understanding interfaces in metal-oxide/organic-acid hybrid materials from first-principles calculations

Vom Promotionsausschuss der
Technischen Universität Hamburg

zur Erlangung des akademischen Grades

Doktor(in) der Naturwissenschaften (Dr. rer. nat.)

genehmigte Dissertation

von
Kai Sellschopp

aus
Braunschweig

2021

Gutachter(innen): Prof. Dr. Stefan Müller
Prof. Dr. Robert Meißner
Prof. Dr. Lucio Colombi Ciacchi

Tag der mündlichen Prüfung: 23. September 2021

Abstract

Interfaces between metal oxides and organic acids play an important role in a wide range of applications, such as catalysis, waste-water treatment, and hybrid materials with exceptional mechanical properties. Enhancing our understanding of these interfaces has the potential to decrease the environmental impact of various industries and guide the development of new materials with unprecedented property combinations. In this work, two transition metal oxides, magnetite (Fe_3O_4) and titania (TiO_2), and their interfaces with carboxylic acids ($R{-}COOH$) are studied, because they perform well in several of the aforementioned applications. Furthermore, the interaction of hydrohalic acids (HX, where $X = F, Cl, Br, I$) with titania nanoparticles is investigated to identify and understand their shape-controlling effects. Hybrid materials made from magnetite or titania nanoparticles linked by organic acids have the ability to combine the special magnetic, catalytic, optical or mechanical properties of the two transition metal oxides with an increased fracture toughness and additional functionality provided by the organic molecule.

Many of the important properties of interfaces are determined by their structure on the atomic scale, the corresponding binding energies, and the electronic structure. First-principles density functional theory (DFT) calculations, which only employ the natural laws of physics without using empirical parameters, can accurately predict these features. However, a thorough sampling of the configurational space is often necessary in order to find the most stable adsorption configurations. Therefore, a new software tool named <u>Co</u>nfiguration space <u>de</u>termination and <u>Red</u>uction (`CodeRed`) is developed in this thesis. It combines chemical intuition for the creation of a wide range of configurations, with unbiased machine learning for an efficient sampling of the configuration space.

As a first application, the new tool is employed to study the adsorption modes of formic acid (HCOOH) on the most important magnetite surfaces, corresponding to the $\{001\}$ and $\{111\}$ facets of magnetite nanoparticles. Combining DFT calculations for different possible structures of the magnetite/carboxylic-acid interface with ab-initio thermodynamics and theoretical vibrational spectra, provides an in-depth view on this system, and enables a direct comparison with experimental data. Thereby, this work explains the lifting of the $(\sqrt{2} \times \sqrt{2})\mathrm{R}45^\circ$ reconstruction of the (001) surface of magnetite upon formic acid adsorption, which is predicted to be accompanied by a strengthening of the interface. On the (111) surface, the thorough structure search reveals two stable adsorption modes, a chelating and a quasi-bi-dentate mode, and indicates a stabilisation of iron vacancies on the surface. Comparison of the calculated vibrational spectra with experimental data shows that both modes are observed on real surfaces.

In the synthesis of nanoparticles, the surface and interface energies can determine the shape of the particles, which affects the performance of the final material. Therefore, the influence of hydrohalic acids on the shape of anatase TiO_2 nanoparticles is studied in this work. Ab-initio thermodynamics confirm the formation of platelet-shaped particles in environments containing HF, and yield a new explanation for the formation of cuboid- or rod-shaped particles in environments containing HCl. The other hydrohalic acids support the formation of bi-pyramid-shaped particles, which is also preferred for carboxylic acids. Studying the competitive adsorption of hydrohalic and carboxylic acids rationalises why fluoride is detected experimentally even after several washing steps, while other halides are more easily replaced by carboxylic acids.

Finally, the mechanical properties of interfaces between anatase TiO_2 nanoparticles and carboxylic acids are investigated by simulating the response to tensile and compressive strain for different binding modes and facets with DFT. The {001} facets, which dominate platelet-shaped particles, are shown to form the interfaces with the highest elastic constants and strengths, in accordance with experiments on hybrid materials made from TiO_2 nanoparticles of different shapes. Furthermore, the calculations examine the fracture mechanisms of the interface, which turn out to be more complicated than a simple de-bonding of the molecule. Instead, interface failure is often caused by the rupture of bonds within the surface, indicating that both the adhesion of molecules on the particle and the cohesion within the particle should be considered for an optimisation of the mechanical properties of hybrid materials.

In its entirety, this thesis provides insights from the viewpoint of computational materials science, enhancing our understanding of hybrid materials made from metal-oxides and organic acids. The results presented here will not only help to improve existing and develop new materials, but also enable the multi-scale modelling of hybrid materials by providing links to methods on larger scales.

Contents

1

Introduction

Materials science is, as the name suggests, the science of understanding existing materials and of finding new materials with interesting properties. The periodic system of elements (see Figure 1.1) gives rise to a practically infinite amount of possible materials through combination of different elements. Sets of combinations can, however, be grouped into classes of materials that have similar properties. Organic materials, for example, typically combine hydrogen, carbon, oxygen, nitrogen, phosphorus, and sulphur to form larger molecules. Metallic alloys, on the other hand, usually consist of one main element with smaller amounts of additives and typically form crystalline structures.

The class of transition metal oxides, of which two examples are studied in this thesis, combines metallic elements from the centre of the periodic table with oxygen. These materials are naturally formed when metals corrode, but transition metal oxides are far more than just a product of corrosion[1]. They also form a significant part of the class of ceramic materials, which are not only known for their strength and hardness, but also for their catalytic performance and ionic conductivity. The two transition metal oxides studied in this thesis, magnetite and titanium dioxide, have particularly interesting current and possible future applications.

Magnetite (Fe_3O_4) nanoparticles are used to treat waste water [1], as well as in several biomedical applications ranging from contrast agents to drug delivery [2]. Their small size in the nanometre to micrometre range ($1\,\mathrm{nm} = 10^{-3}\,\mu\mathrm{m} = 10^{-9}\,\mathrm{m}$) drastically increases the specific surface area, and allows them to move around freely. Furthermore, the tunable magnetic properties and the vast amount of possibilities to functionalise magnetite nanoparticles make them interesting for these kind of applications. For example, organic molecules that are tuned to perform well on some task at hand, can be bound to the magnetite particles via an organic acid linker group. The magnetism of the particle then makes it possible to recover the nanoparticles after use, steer them to an area of interest or even heat them up [2]. Additionally, magnetite catalyses the water-gas shift reaction [3] and Fischer-Tropsch synthesis routes [4]. Both play an important role in the chemical industry, and for the

---

[1] A popular example is iron oxide, commonly known as rust, the corrosion product of iron, and a very versatile material.

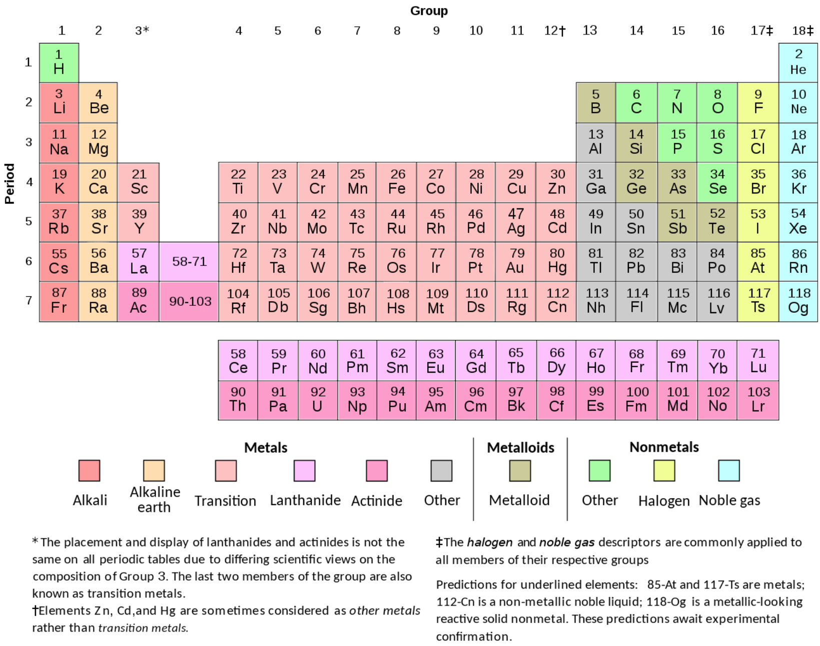

*The placement and display of lanthanides and actinides is not the same on all periodic tables due to differing scientific views on the composition of Group 3. The last two members of the group are also known as transition metals.

†Elements Zn, Cd,and Hg are sometimes considered as *other metals* rather than *transition metals.*

‡The ***halogen*** and ***noble gas*** descriptors are commonly applied to all members of their respective groups

Predictions for underlined elements: 85-At and 117-Ts are metals; 112-Cn is a non-metallic noble liquid; 118-Og is a metallic-looking reactive solid nonmetal. These predictions await experimental confirmation.

Figure 1.1: Periodic system of elements (source: wikimedia commons[2]). The different elements are sorted by their atomic number, which corresponds to their number of protons in the atomic core, the period, which corresponds to the principal quantum number of the highest occupied atomic orbital, and the group number, which is related to similar occupation states of the s-, p- and d-orbitals.

creation of a circular economy that does not depend on fossil fuels. Recently, magnetite also became an interesting material for the emerging field of single-atom catalysis, where catalytic activity is increased dramatically by reducing the size of the catalyst to one single atom [5]. In this field, magnetite is interesting, because its {001} facets support the adsorption of single transition metal atoms [6].

Nanoparticles made from titanium dioxide (TiO_2) are widely used in industry. They are found in cosmetic products, such as sunscreen or creams, but also in paint [7]. TiO_2 is ideal for these applications, because it has a

---

[2] The image was downloaded from `https://commons.wikimedia.org/wiki/File:Taxonomic_PT_wth_halogens_SVG.svg`, where it was published by the user Giftson under the Creative Commons Attribution-Share Alike 4.0 International license, and is printed here without any changes.

band gap of 3.0 eV or 3.2 eV, depending on the crystal structure [8], which is perfectly suited to absorb light in the ultra-violet range and reflect light in the visible range. Furthermore, its band gap and abundance also makes TiO_2 an interesting candidate for photo-catalysis [9, 10]. One major goal in this field is to produce fuels, such as hydrogen (H_2) or methane (CH_4), from water (H_2O), carbon dioxide (CO_2), and sunlight [11, 12]. The process can also be turned around to oxidise larger organic pollutants into CO_2 and H_2O. However, despite the fact that the possibility of applying TiO_2 as a photo-catalyst for water splitting has been known since the 1970s [9], it is still not yet widely used, because the efficiency is quite low and the band structure needs to be tuned through combination with other materials [13–15].

1.1 Motivation

Even though this thesis contributes to the understanding of the aforementioned applications of magnetite and titanium dioxide, the original motivation for this work stems from the field of hierarchical hybrid materials, as studied and developed by the SFB986 "Taylor-<u>M</u>ade <u>M</u>ulti-scale <u>M</u>aterials (M^3)".[3] Inspired by nature, these materials are characterised by similar structures on different length scales as shown in Figure 1.2. At the lowest scale, ceramic nanoparticles (e.g. magnetite or titanium dioxide) are covered with organic acids. Then, they are assembled in a super crystal, and functional groups within the organic acids allow the particles to interlink [16]. This assembly is referred to as the first level of hierarchy and already shows promising mechanical properties [17–19]. Covering the super-crystalline particles with another organic layer and assembling them into a brick-and-mortar-like structure then forms the next level of hierarchy [16]. In principle, this idea can be continued on to an arbitrary number of hierarchy levels. The main goal is to create a hybrid material which makes use of the high fracture toughness of the organic component, while retaining as much of the high strength of the ceramic component as possible. Moreover, varying the constituents of the different levels of hierarchy may also allow to add other special properties, such as magnetism, self-healing or electrical conductivity, to the material [20].

From Figure 1.2 it becomes obvious that the final material will have an enormous interface area between the ceramic nanoparticles and the surrounding organic phase. Hence, for a full comprehension and optimisation of these materials, it is crucial to understand and investigate the interfaces first. Due to the small size of the nanoparticles, the interfaces need to be studied at the atomic scale with a combination of theoretical and experimental methods. This thesis addresses the theoretical part through quantum mechanical simulations, but the computational results are combined with and compared to results from experiments performed by colleagues within the SFB986 and

---

[3] *SFB* stands for *Sonderforschungsbereich*, which translates to *Collaborative Research Center*, and is one of the largest funding schemes of the German Research Council. It provides funding for several connected, often interdisciplinary projects. For more information on the SFB986 visit `https://www.tuhh.de/sfb986/`

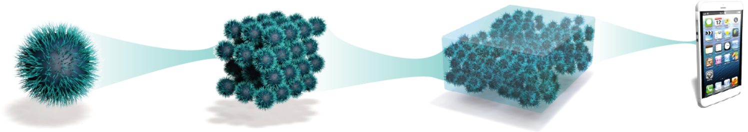

Figure 1.2: Illustration of the general idea of area A of the SFB986. Ceramic nanoparticles covered with organic acids are assembled in three-dimensional structures on different levels of hierarchy. (Printed with permission from the SFB986 – M3, source: `https://www.tuhh.de/sfb986/`)

other scientists. First-principles calculations based on density functional theory (DFT) have become the standard for simulating atomic structures on the quantum-mechanical level in the past decades. They allow to model assemblies of up to a few hundred atoms with reasonable computational resources and very high accuracy without needing experimentally determined parameters. Furthermore, DFT gives access to the electronic structure, and allows to predict the breaking and formation of chemical bonds. Therefore, DFT calculations are ideally suited to study interfaces and the adsorption of small and medium sized molecules on surfaces.

The main research question underlying this thesis is: *How can the properties of hybrid materials be improved?* In order to answer this question, though, further sub-questions have to be answered first. What is the atomic structure of the interface between the organic acid and the oxide nanoparticles? How strong is the binding of the interface and which mechanisms lead to a failure? How can we influence the shape of the nanoparticles through different surfactants, and which effect has the shape on the final properties? This thesis addresses all these questions with the help of DFT calculations and through comparison with existing experimental data. However, it should be noted that this thesis can only be another piece in the challenging and interesting puzzle of understanding this versatile class of materials.

1.2 Outline of the thesis

In order to answer the posed research questions, first the atomic structures of the interfaces between the crystalline transition metal oxides and the organic molecules have to be known. Finding these structures usually proves to be more difficult than just applying chemical intuition, and modern atomic scale surface science experiments need computational results to help with the interpretation of their data. Therefore, after introducing the research methods in Chapter 2, Chapter 3 describes the development of a new software tool to efficiently find the most stable interface structure. The name of the new tool written in the python programming language is `CodeRed`, which stands for Configuration space determination and Reduction. Its purpose is to create many different possible starting structures for DFT calculations, while including the existing knowledge about the system. In order to make this sampling of the configuration space more efficient, selection algorithms based on machine learning techniques are implemented. Thereby, `CodeRed` combines selection based on chemical intuition and machine learning with a systematic sampling of the configurational space.

The next step for understanding the aforementioned hybrid materials is to investigate interfaces between magnetite and carboxylic acids. Surprisingly, little is known about these interfaces on the atomic scale so far, even though they play a role in a range of applications. As the smallest representative of the carboxylic acid family, formic acid (HCOOH) is studied here. Insights from DFT calculations on the adsorption of formic acid on different facets of magnetite nanoparticles are presented in Chapter 4 and discussed in terms of the binding strength. Techniques that go beyond DFT, such as ab-initio thermodynamics and density functional perturbation theory (DFPT), further allow to predict the most stable structures and vibrational modes in experimental conditions, enabling a direct comparison with experiments and identification of the interface structure in real world conditions. Interestingly, the interaction of formic acid with magnetite is found to change the underlying surface structure, which has a direct impact on the strength of the interface.

The adsorption of carboxylic acids on titanium dioxide nanoparticles was already investigated in previous works. However, during synthesis concurring adsorption phenomena with hydrohalic acids (HX, where $X = F, Cl, Br, I$), that are created in the process, play a role. Therefore, the adsorption of all hydrohalic acids is studied in Chapter 5, employing DFT calculations. Ab-initio thermodynamics then enable a prediction of how difficult it is to replace the hydrohalic acids with the carboxylic acid linkers. Furthermore, shape-controlling effects that go beyond the already well-known platelet-stabilising effect of solutions containing fluoride are elucidated. Comprehending these effects and how to adjust the reaction conditions to obtain different shapes is important for experimentalists, since the shape impacts other properties, such as mechanical strength, fracture toughness, and thermal conductivity.

In order to really understand the impact of different interface structures on the mechanical properties of hybrid materials, these properties have to be modelled at least for some relevant limiting cases. Hence, a virtual mechanical testing device for interfaces is created in Chapter 6, and applied to different titanium-dioxide/carboxylic-acid interfaces. The results link the elastic properties of hybrid materials made from particles with different shapes to the elastic properties of the corresponding interfaces. Furthermore, they provide insight into the fracture mechanism of the interface, which makes it possible to improve the atomic structure of interfaces in the future. Last, but not least, the virtual mechanical testing on the level of DFT calculations can be used in the future to parametrise computational models on larger scales, such as classical molecular dynamics (MD) simulations or continuum mechanics models, enabling a true multi-scale modelling.

Each chapter ends with concluding remarks, which summarise the contents of the chapter and give an outlook on possible future research in the corresponding field. The last chapter of the main part contains a full summary and conclusion of the whole thesis, putting the results into a bigger context, and developing ideas for research that might be inspired by this work. Further helpful information and computational details are provided in the appendix. Non-printable supplementary material, such as animations of vibrational modes and of the structural evolution of hybrid interfaces under tensile load, can be downloaded from the internet, if desired[4]. The digital version of this thesis is available at `https://doi.org/10.15480/882.3791`, which can be accessed by scanning the QR code on the left.

SCAN ME

---

[4] Visit `https://doi.org/10.15480/336.3408` for obtaining the online supporting material. The link can also be accessed by scanning the QR code at the beginning of Appendix D.

2

Methodology

This chapter introduces the methods applied in the rest of the thesis. In general, a basic knowledge of physics (especially quantum mechanics), chemistry, and materials science is expected, since a complete introduction to all the details would be beyond the scope of this work. A general introduction to solid state physics and materials science can be found in the books by C. Kittel [21] and G. Gottstein [22], respectively. For a basic introduction to quantum physics, the Feynman lectures on physics [23] are a good starting point, while the book on theoretical surface science by A. Gross [24] is recommended for obtaining a deeper understanding of the background of the methodology relevant for this thesis.

The notation in this work follows the symbols and expressions commonly used in physics. Particularly, vectors are written with an arrow on top ($\vec{\square}$), while matrices are written in bold font ($\boldsymbol{\square}$). Furthermore, quantum mechanical operators are indicated by a hat ($\hat{\square}$), and the bra-ket notation ($\langle\square|$, $|\square\rangle$) is used for quantum states at some points. The remaining special symbols and expressions will be introduced in the text when they are used.

This chapter is structured according to the length scales of the different methods: First, the fundamentals of electronic structure calculations, and especially density functional theory (DFT), are explained. Then, the practical aspects of implementing DFT into computer code are discussed briefly. While the former should give the reader an idea of the physical accuracy of the underlying theory, the intention of the latter is to shine light on the numerical accuracy of DFT calculations performed in this work. The focus is then shifted towards calculating an optimised atomic structure and vibrational properties, enabling the comparison with experimental data. Next, the computational modelling of surfaces and their interaction with different chemical environments is introduced. Finally, arriving at the largest length scale relevant for this thesis, the last section of this chapter explains the prediction of nanoparticle shapes with the Wulff construction.

2.1 Electronic structure calculations

Formation enthalpies to compare the thermodynamic stability of different phases, binding modes of molecules on surfaces, band gaps of materials, and many more properties can be derived from electronic structure calculations. Hence, electronic structure calculations are one of the key elements to understand materials on the atomic, but also on larger length scales. For many properties it is enough to know the electronic ground state of a given system, i.e. the state with the lowest energy. In order to find the ground state $|\psi\rangle$, and its corresponding energy E, one would have to solve the famous static Schrödinger equation

$$\hat{H}\,|\psi\rangle = E\,|\psi\rangle\,, \tag{2.1}$$

where $\hat{H}$ is the Hamilton operator (or *Hamiltonian*) of the system. It can be written as a sum of the kinetic energy operators $\hat{T}_e$ and $\hat{T}_c$ of the electrons and the atomic core, respectively, and the different contributions to the Coulomb energy of the charged particles, namely the electron-electron interaction operator $\hat{V}_{e-e}$, the electron-core interaction operator $\hat{V}_{e-c}$, and the core-core interaction operator $\hat{V}_{c-c}$:

$$\hat{H} = \hat{T}_e + \hat{T}_c + \hat{V}_{e-e} + \hat{V}_{e-c} + \hat{V}_{c-c} \tag{2.2}$$

In most cases, the kinetic energy of the atomic cores is much lower than the kinetic energy of the electrons. Therefore, the atomic cores can be considered as fixed on their positions $\mathbf{R} = \left(\vec{R}_1, \ldots, \vec{R}_M\right)$. This is called the *Born-Oppenheimer approximation.* It allows to solve the electronic part of the problem separately for a fixed configuration of atoms and then to adjust the positions of the atoms according to the calculated forces acting on them. The electronic Schrödinger equation is then given by

$$(\hat{T}_e + \hat{V}_{e-e} + \hat{V}_{c-e})\,|\psi\rangle = E_e\,|\psi\rangle\,. \tag{2.3}$$

However, solving this equation for many-electron systems proves difficult for several reasons. The main reason is the dimensionality of the wave function $|\psi\rangle$. For one electron, $|\psi\rangle$ is a three-dimensional function (for example, depending on the three cartesian coordinates x, y, z). As such, sampling this function with 10 points in every dimension would result in 10^3 data points, occupying roughly 8 kByte of disk space on a computer. The problem with describing more particles, is that each additional particle adds three additional dimensions to the wave function. Sampling the wave function of a single oxygen atom containing 8 electrons with 10 points in every dimension would therefore already result in 10^{24} data points, which could not be stored, because it would exceed the current data storage capacity of the entire world. Obviously, a different theory framework is needed to perform materials simulations.

Density Functional Theory

In 1964 and 1965, P. Hohenberg, W. Kohn, and L.J. Sham found that the electron density of the ground state completely determines the Hamiltonian of the system, and hence also the wave function and energy of the ground state [25, 26]. In other words, all the information needed to calculate the observables of the system is already included in the electron density. Therefore, one only needs to store this 3-dimensional function instead of the complex $3N$-dimensional wave function. In contrast to the wave function, which is a mathematical construct, the electron density $\rho(\vec{r})$ is an observable that describes the probability of finding an electron at a certain position $\vec{r}$, and therefore, can be measured experimentally. However, in order to calculate the electron density and resulting observables of the ground state, the Hamilton operator has to be expressed as a functional of the density, which proves to be very difficult and is a remaining challenge in density functional theory research.

As a starting point, the interaction between the atomic cores and the electrons $\hat{V}_{c-e}$ can be written as the density functional

$$V_{c-e}[\rho] = \langle\psi|\,\hat{V}_{c-e}\,|\psi\rangle = \int \mathrm{d}^3r\, v_c(\vec{r})\rho(\vec{r}), \tag{2.4}$$

where v_c is the coulomb potential created by the atomic cores. Typically, point charges are used to describe the cores, which yields

$$v_c(\vec{r}) = -\frac{e^2}{4\pi\varepsilon_0}\sum_{i=1}^{M}\frac{Z_i}{\left|\vec{r}-\vec{R}_i\right|}, \tag{2.5}$$

where e is the elemental charge, ε_0 is the dielectric constant, and Z_i is the atomic number of core i at position $\vec{R}_i$. Since this is the only point where the positions of the atomic cores directly contribute to the energy, the remaining functionals for the kinetic energy $T_e[\rho]$ and the electron-electron interaction $V_{e-e}[\rho]$ should be universal for all possible electron densities. Unfortunately, there is no analytical expression available for these functionals. In order to circumvent this problem, Kohn and Sham used the concept of describing the system with the help of a single electron interacting with the charge density of all electrons. In this single electron description, the density functional of the kinetic energy is still unknown, but it can be calculated now from the single particle wave functions $\phi_n(\vec{r})$ via

$$T_e[\phi_n[\rho]] = \sum_{\substack{n=1\\ occ}}^{N} -\frac{\hbar^2}{2m_e}\int \mathrm{d}^3r\,\phi_n^*(\vec{r})\nabla^2\phi_n(\vec{r}), \tag{2.6}$$

where $\hbar$ is the reduced Planck's constant, m_e is the mass of an electron, and the sum runs only over the occupied states of the system. Technically, the single particle wave functions are also a density functional, but even though the density is defined by

$$\rho(\vec{r}) = \sum_{\substack{n=1\\occ}}^{N} |\phi_n(\vec{r})|^2, \tag{2.7}$$

there is no analytical way to invert this definition to obtain $\phi_n[\rho]$. The density functional for the classical Coulomb energy of the charge density, on the other hand, can be expressed analytically as

$$V_{cl}[\rho] = \frac{1}{2}\frac{e^2}{4\pi\varepsilon_0}\int \mathrm{d}^3r \int \mathrm{d}^3r' \, \frac{\rho(\vec{r})\rho(\vec{r}')}{|\vec{r}-\vec{r}'|} = \frac{1}{2}\int \mathrm{d}^3r \, v_{cl}(\vec{r})\rho(\vec{r}). \tag{2.8}$$

This means, however, that the single electron is not only interacting with the other electrons, but also with itself, leading to a self-interaction error. Moreover, there are non-classical interactions between electrons that are not included in these functionals. Since the electrons are identical (Pauli principle), an exchange of two electrons should not change the observables. Also, as quantum objects, electrons affect the movement of other electrons in non-classical ways, which is called correlation. All these contributions are captured in an unknown exchange-correlation functional

$$E_{xc}[\rho] = T_e[\rho] - T_e[\phi_n[\rho]] + V_{e-e}[\rho] - V_{cl}[\rho]. \tag{2.9}$$

Applying the variational principle to the whole electron energy density functional $E_e[\rho] = T_e[\phi_n[\rho]] + V_{cl}[\rho] + V_{c-e}[\rho] + E_{xc}[\rho]$, one arrives at the Kohn-Sham equations for the determination of the single particle wave functions:

$$\left[-\frac{\hbar^2}{2m_e}\nabla^2 + v_{eff}(\vec{r})\right]\phi_n(\vec{r}) = E_n\phi_n(\vec{r}) \tag{2.10}$$

The effective one particle potential $v_{eff}(\vec{r})$ includes the potential energy contributions discussed before

$$v_{eff}(\vec{r}) = v_c(\vec{r}) + v_{cl}(\vec{r}) + v_{xc}(\vec{r}), \tag{2.11}$$

with the exchange-correlation potential $v_{xc}(\vec{r}) = \frac{\delta E_{xc}[\rho]}{\delta\rho(\vec{r})}$ derived from the corresponding functional. Since the effective potential has to be calculated from the density, which in turn has to be calculated from the single-particle wave functions, solving the Kohn-Sham equations (2.10) is an iterative process. Starting from a first guess, for example from atomic orbitals, the density and potential are calculated. Then, the solution of (2.10) yields new single-particle wave functions, resulting in a new density and a new potential. The process is continued until the density, and therefore also the energy, does not change significantly any more.

Density Functional Approximations

As previously stated, the problem of the unknown exchange-correlation functional $E_{xc}[\rho]$ still remains. Luckily, there are ways to approximate this functional, so that it fulfils certain conditions that the exact functional must satisfy as well. The simplest, yet still quite successful approach, is to use the exchange-correlation functional of the homogeneous electron gas. Since this approximation assumes that the density is varying slowly on a local scale, it is named Local Density Approximation (LDA). The exchange part of the LDA potential can be expressed analytically, while the correlation part can be calculated separately to an arbitrary accuracy with the quantum-Monte-Carlo method [27]. Therefore, the LDA XC-functional is free from any parameters. On the other hand, binding energies are typically overestimated in the LDA, as a result of the stronger de-localisation of electrons [28].

Exchange-correlation functionals in the Generalised Gradient Approximation (GGA) aim to improve the accuracy by including the influence of density gradients on the exchange-correlation energy. There are, however, several possible ways to include the influence of gradients, resulting in a wide variety of GGA XC-functionals with different parametrisations. The most popular of these, according to a poll among theoretical chemists [29], is the functional by J. Perdew, K. Burke, and M. Ernzerhof (PBE, [30]), which is also used in Chapter 4. The GGA results in less overbinding than the LDA, but the correction is too strong in some cases, leading to an underestimation of binding energies [28].

Further improvements in accuracy can be achieved by meta-GGA (mGGA) functionals, which take the concept of the generalised gradient approximation further, and include second order derivatives of the density, corresponding to the kinetic energy density τ. One prominent candidate from this class, the Strongly Constrained and Appropriately Normed (SCAN) functional [31], is the first mGGA functional to obey all known exact constraints for this class. In summary, the different approximations can be written as:

$$E_{xc}^{\mathrm{LDA}}[\rho] = \int \mathrm{d}^3r\, \rho(\vec{r})\epsilon_{xc}(\rho) \tag{2.12}$$

$$E_{xc}^{\mathrm{GGA}}[\rho] = \int \mathrm{d}^3r\, \rho(\vec{r})\epsilon_{xc}(\rho, \nabla\rho) \tag{2.13}$$

$$E_{xc}^{\mathrm{mGGA}}[\rho] = \int \mathrm{d}^3r\, \rho(\vec{r})\epsilon_{xc}(\rho, \nabla\rho, \tau) \tag{2.14}$$

Even higher accuracy can be achieved by mixing in exact exchange or using methods beyond DFT. However, increasing the accuracy and including more contributions to the XC-functional also increases the computational costs. Therefore, a trade-off between accuracy and cost is necessary in practice.

The locality in the definition of not only LDA, but also GGA and mGGA, makes it difficult for these functionals to accurately describe the long-ranged van-der-Waals interactions. There are different possibilities to circumvent this problem. The solution used for some calculations in this work, is to add a nonlocal correlation functional [32], and then re-parametrise the underlying XC-functional in order to correct for the additional local correlation [33]. It has to be noted, though, that the re-parametrisation is based on an optimisation of the mean average error with respect to a small database of weakly interacting bio-organic compounds. Nevertheless, some representatives from this class of optGGA-vdW functionals were shown to also reproduce the lattice constants, bulk moduli, and atomisation energies of several metals, semiconductors, and insulators with high accuracy [34].

Another issue with DFT calculations is the description of strong correlations, that lead to the localisation of d- and f-electrons, for example. In order to account for these correlations without a drastic increase in computational costs, an on-site correction can be applied to the density functional for the supposedly strongly correlated orbitals [35]. This correction can be interpreted as an additional energy barrier against the de-localisation of d- and f-electrons, meaning that these orbitals are more likely to be either fully occupied or fully unoccupied. It introduces at least one additional parameter, named Hubbard U (after its inventor), that scales the height of the barrier. The parameter can be obtained from calculations with higher order methods or fitted to match experimental results.

2.2 Implementation in computer code

In this thesis, the Vienna Ab-initio Simulation Package (VASP [36, 37], version 5.4.4) is used to perform electronic structure calculations. Since it is designed for solid state systems, VASP employs periodic boundary conditions representing the translational symmetry of crystalline materials. In this section, different technical aspects for the computation of DFT solutions as they are implemented in VASP, are explained briefly. For a more detailed overview of the features and background of VASP, please refer to its manual[1] and the references therein. The detailed computational settings used for the different parts of this work are documented in Appendix A.

Integration in reciprocal space

In a periodic potential, the Bloch theorem applies to the single particle wave functions ϕ_n calculated from the Kohn-Sham equations (2.10). Therefore, they can be expressed as the product

$$\phi_{n,\vec{k}}(\vec{r}) = u_{n,\vec{k}}(\vec{r}) \cdot \mathrm{e}^{i\vec{k}\vec{r}}, \tag{2.15}$$

where $u_{n,\vec{k}}(\vec{r})$ is a function with the same periodicity as the potential, and $\mathrm{e}^{i\vec{k}\vec{r}}$ is a plane wave with wave vector $\vec{k}$. It follows that the wave functions and band

---

[1] The VASP manual is available at `https://www.vasp.at/wiki/index.php/The_VASP_Manual` and also contains links to lectures, workshops, and tutorials on DFT and its implementation in VASP.

structure $E(\vec{k})$ are periodic in the reciprocal space[2], meaning that they do not change when the wave vector $\vec{k}$ is translated by a reciprocal lattice vector $\vec{G}$. Hence, the single particle wave functions only need to be calculated for wave vectors lying in the first Brillouin zone (BZ)[3]. The quantities needed to solve the Kohn-Sham equations then follow from an integration in reciprocal space. The electron density as the core property of DFT, for example, is calculated as

$$\rho(\vec{r}) = \frac{1}{\Omega} \sum_{\substack{n=1 \\ occ}}^{N} \int_{1^{\text{st}}\ \text{BZ}} \mathrm{d}^3k \left| \phi_{n,\vec{k}}(\vec{r}) \right|^2, \tag{2.16}$$

with the integration only running over the first BZ having the volume Ω. The wave function varies slowly with respect to the wave vector. Therefore, the integral can be approximated by a weighted sum over a discrete set of points in reciprocal space, called *k-points.* In continuation of the example above, equation (2.16) is approximated by

$$\rho(\vec{r}) \approx \sum_{\substack{n=1 \\ occ}}^{N} \sum_{\vec{k}}^{1^{\text{st}}\ \text{BZ}} w_{\vec{k}} \left| \phi_{n,\vec{k}}(\vec{r}) \right|^2. \tag{2.17}$$

The k-points to sum over can be chosen as an equally spaced mesh in the reciprocal space. The mesh is then reduced based on the symmetry of the system, yielding a set of irreducible k-points. The weights $w_{\vec{k}}$ are then determined from the number of symmetrically equivalent k-points that appeared in the first BZ during the reduction. Of course, the approximation is improved when more irreducible k-points are used to replace the integral, but on the other hand, computational costs also increase with the number of k-points. Therefore, convergence tests are performed in practice to balance accuracy and cost.

Plane wave basis sets

Even though the data storage problem was drastically reduced by DFT, since only N 3-dimensional wave functions have to be stored on disk, the question of how to store these functions remains. Typically, the one particle wave functions are expanded in a set of orthonormal basis functions, and the expansion coefficients are stored on the computer. The set of basis functions is usually chosen depending on the system. Modelling localised systems, such as

---

[2] The Fourier transform of the real space is usually referred to as *reciprocal space.* Therefore, a periodic crystal lattice in real space (with base vectors $\vec{a}_1, \vec{a}_2, \vec{a}_3$) results in a corresponding reciprocal lattice with the base vectors $\vec{b}_1 = \frac{2\pi}{V}\vec{a}_2 \times \vec{a}_3, \vec{b}_2 = \frac{2\pi}{V}\vec{a}_3 \times \vec{a}_1, \vec{b}_3 = \frac{2\pi}{V}\vec{a}_1 \times \vec{a}_2$, where V is the volume of the unit cell in real space. In analogy to the lattice translation vector in real space $\vec{T} = h\vec{a}_1 + k\vec{a}_2 + l\vec{a}_3$ $(h, k, l \in \mathbb{Z})$, reciprocal lattice vectors $\vec{G}$ are multiples of the reciprocal base vectors $(\vec{G} = h\vec{b}_1 + k\vec{b}_2 + l\vec{b}_3)$.

[3] The first Brillouin zone is a special primitive unit cell in reciprocal space, constructed in the same way as the Wigner-Seitz cell in real space.

molecules and gas phase reactions, is simplified by employing localised basis sets, for example atomic orbitals described by Gaussian functions. Periodic systems, such as bulk crystals and surfaces, however, are usually modelled employing a plane waves basis set, which simplifies the calculation of these systems drastically. Therefore, in this thesis a plane waves basis set is employed for the expansion of the one particle wave functions, yielding

$$\phi_{n,\vec{k}}(\vec{r}) = \frac{1}{\sqrt{\Omega}} \sum_{\vec{G}} C_{\vec{G},n,\vec{k}} \mathrm{e}^{i\left(\vec{G}+\vec{k}\right)\vec{r}}. \tag{2.18}$$

In theory, the summation runs over all possible reciprocal lattice vectors $\vec{G}$, which means that an infinite amount of expansion coefficients $C_{\vec{G},n,\vec{k}}$ would have to be stored. Luckily, most properties of interest converge fast with respect to the maximum kinetic energy of the plane waves in the basis set. Therefore, a cut-off energy E_{cut} that limits the amount of reciprocal lattice vectors to sum over via the relation

$$\left|\vec{G}+\vec{k}\right| < \frac{\sqrt{2m_e E_{\mathrm{cut}}}}{\hbar}, \tag{2.19}$$

can be defined. Higher cut-off energies result in more reciprocal lattice vectors to sum over and hence, a higher accuracy of the representation, but also more coefficients to calculate and store. Consequently, a balance between cost and accuracy has to be found for E_{cut} as well, with the help of convergence testing.

Pseudopotentials

The limitation to a maximum kinetic energy of the functions in the basis set causes problems in the description of strongly localised states. Describing these states close to the atomic core would require plane waves with a short wavelength, i.e. larger wave vectors, and hence, higher cut-off energies. VASP combines two techniques to circumvent this problem. The first one is the frozen core approximation. It assumes that the localised states close to the core are not affected much by changes in the outer shell or valence states. Therefore, they can be calculated beforehand, and only the valence electrons are treated explicitly during the electronic optimisation. Secondly, pseudopotentials are used to replace the real potential close to the core. It should be noted, though, that there are also alternatives to the pseudopotential approach implemented in VASP and many other electronic structure codes. The Linearised Augmented Plane Wave (LAPW) method [38], for example, employs the muffin-tin approximation, which includes all electrons, but treats the core and valence electrons differently, resulting in decreased computational costs.

There are different flavours of pseudopotentials in electronic structure calculations, but the underlying idea is always the same. The diverging Coulomb potential of the atomic core is replaced by a finite pseudopotential, that approaches the original potential at a cut-off radius r_c, and matches the original

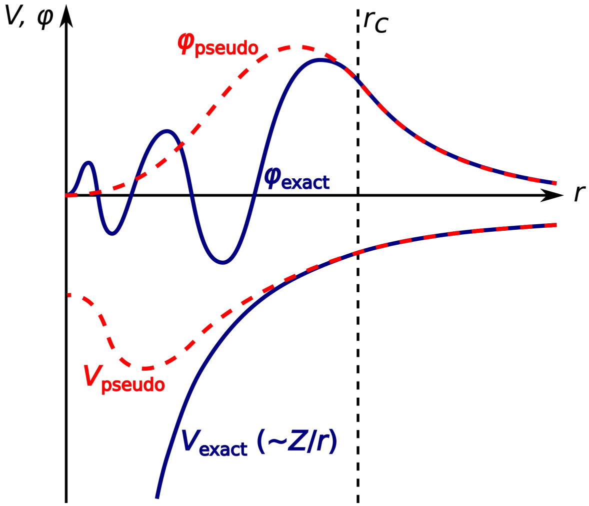

Figure 2.1: Illustration of the pseudopotential method. The exact potential (V_{exact}, bottom blue line) is replaced by a pseudopotential (V_{pseudo}, bottom red dashed line) that equals the exact potential above the cut-off radius r_c. The resulting pseudo-orbital (φ_{pseudo}, top red dashed line) also equals the exact orbital (φ_{exact}, top blue line) above r_c, but can be described with less plane waves in the basis set, due to the reduced number of nodes.

potential exactly for $r > r_c$ (see Figure 2.1). This design ensures that the resulting pseudo-wave function also approaches the real wave function at r_c and becomes the exact real wave function for $r > r_c$. In general, this would still lead to different eigenvalues, and the pseudo-wave function and pseudo density would have a different norm than the original one. A solution is to use the projector augmented wave (PAW) method [39], which uses projections of the pseudo-orbitals onto the real, pre-calculated all-electron orbitals to reproduce the eigenvalue spectrum. In order to correct the norm-error, a compensation charge is introduced in the region of the pseudopotential. As a result, the total energy is reproduced with high accuracy using PAW pseudopotentials, while the computational costs are reduced significantly, since much less plane waves are needed in the basis set in order to describe the system.

2.3 The atomic structure

DFT solves the problem of finding the electronic ground state of a given atomic configuration. However, if that configuration is far away from any real atomic structure, the predictions from DFT calculations are not very meaningful.

Since every system tends to minimise its energy due to the laws of thermodynamics, it makes sense to not only minimise the electronic energy, but also the energy of the atomic structure. This minimisation of the total energy with respect to the atomic positions then yields the ground state of the whole system. The ground-state configuration usually gives a good first approximation for the real world structure of a system, considering that energy differences between dissimilar configurations can easily be much larger than the thermal energy. Nevertheless, small deviations from the ground state configuration arise due to the temperature and other perturbations, leading to specific vibrations that can be detected experimentally. Both the relaxation of the structure to the ground state and calculating vibrational properties following perturbations are introduced in this section.

Forces on atoms and the ground state configuration

Minimising the energy with respect to the atomic positions $\mathbf{R} = (\vec{R}_1, \ldots, \vec{R}_M)$ is equivalent to finding a force-free state, because the force acting on an atom i is given by the gradient $\vec{F}_i = -\frac{\partial \langle E \rangle}{\partial \vec{R}_i}$, which becomes zero at the minimum. Therefore, this process is also called *relaxation*. Calculating the root of the forces numerically with, for example, conjugate gradient or Newton algorithms, is an efficient way to find the ground state configuration. However, in general these minimisation algorithms will usually relax towards a nearby local minimum, which is not necessarily the global minimum energy structure. More information on this topic and one way to tackle the problem is presented in Chapter 3. Apart from structural relaxations, calculating the forces is also interesting for other types of calculations, such as ab-initio molecular dynamics or the analysis of vibrational modes.

With the electronic ground state made available from DFT calculations (within the aforementioned approximations), one can now come back to the full Hamiltonian in Equation (2.2), including the atomic cores and their positions $\mathbf{R}$. According to the Hellman-Feynman theorem, the forces on each atom can be directly computed from the full Hamiltonian $\hat{H}$ and the wave function of the ground state ψ:

$$\vec{F}_i = - \langle \psi | \frac{\partial \hat{H}}{\partial \vec{R}_i} | \psi \rangle \tag{2.20}$$

The gradient only has contributions from the core-electron interaction $\hat{V}_{c-e}$, and the core-core interaction $\hat{V}_{c-c}$, which depend explicitly on the atomic positions:

$$\langle \psi | \frac{\partial \hat{H}}{\partial \vec{R}_i} | \psi \rangle = \langle \psi | \frac{\partial \hat{V}_{c-e}}{\partial \vec{R}_i} | \psi \rangle + \langle \psi | \frac{\partial \hat{V}_{c-c}}{\partial \vec{R}_i} | \psi \rangle \tag{2.21}$$

In a classical description of the atomic cores, the contribution from the core-core interactions can be calculated analytically from the Coulomb potential

$$v_{c-c}(\mathbf{R}) = \frac{e^2}{4\pi\varepsilon_0} \sum_{i=1}^{M} \sum_{j=i+1}^{M} \frac{Z_i Z_j}{\left|\vec{R}_i - \vec{R}_j\right|}. \tag{2.22}$$

As mentioned before, DFT does not yield the wave function of the ground state, but only some single particle wave functions ϕ_n with the same density as ψ. Nevertheless, the expectation value of the core-electron potential gradient can also be calculated from the electron density as

$$\langle\psi| \frac{\partial \hat{V}_{c-e}}{\partial \vec{R}_i} |\psi\rangle = \int \mathrm{d}^3 r \, \rho(\vec{r}) \frac{\partial v_c(\vec{r})}{\partial \vec{R}_i}. \tag{2.23}$$

In conclusion, the forces can be calculated directly from the electronic ground state density and the current atomic positions. In practice, the relaxation procedure starts from an initial configuration, performs a DFT calculation, evaluates the forces, and then changes the configuration accordingly. The procedure is repeated until the forces or the change in energy between two steps are close to zero, as defined by a convergence criterium.

Calculation of vibrational modes

For comparison with experimental results, not only the ground state, but also the reaction of the system to small perturbations plays a role. In infrared (IR) spectroscopy, for example, the incoming light triggers small vibrations around the ground state configuration. The frequency and intensity of the light absorption depends on the associated energy and dynamical dipole moment of the vibration. Therefore, in principle, the vibrational spectrum can be obtained from electronic structure calculations.

When the configuration consisting of M atoms is close to a minimum-energy structure with atomic positions $\mathbf{R}^{(0)} = (\vec{R}_1^{(0)}, \ldots, \vec{R}_M^{(0)})$, the harmonic approximation applies and the total energy can be expanded with respect to a small displacement $\mathbf{u} = \mathbf{R} - \mathbf{R}^{(0)} = (\vec{u}_1, \ldots, \vec{u}_M)$

$$E\Big(\mathbf{R}^{(0)} + \mathbf{u}\Big) \approx E\Big(\mathbf{R}^{(0)}\Big) + \frac{1}{2} \sum_{i=1}^{M} \sum_{j=1}^{M} \vec{u}_i^{\mathsf{T}} \left. \frac{\partial^2 E}{\partial \vec{u}_i \partial \vec{u}_j} \right|_{\mathbf{R}^{(0)}} \vec{u}_j. \tag{2.24}$$

Here, the linear term in $\mathbf{u}$ was dropped, because it vanishes for the minimum energy structure, as discussed before. Small vibrational displacements can be expressed as a set of orthonormal vibrational patterns $\mathbf{U}$ called *normal modes*, which are determined from the following set of characteristic equations:

$$\sum_{j=1}^{M} \mathbf{C}_{ij} \vec{U}_j - m_i \omega^2 \vec{U}_i = 0 \tag{2.25}$$

Note that the force constants $\mathbf{C}_{ij}$ are 3×3-matrices, but also the elements of a symmetric $M \times M$-matrix, while m_i and ω denote the mass of atom i and

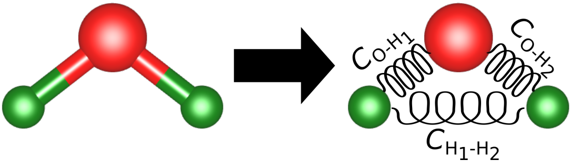

(a) harmonic approximation for water (H_2O)

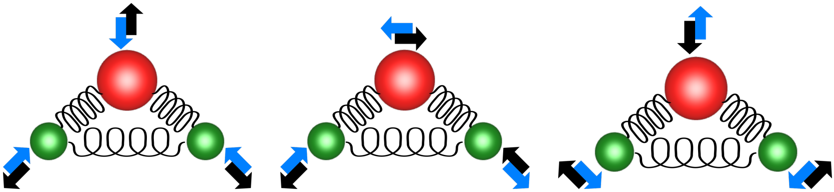

(b) normal modes of water (H_2O)

Figure 2.2: Illustration demonstrating the basics of the vibrational modes calculations for the example of the tri-atomic water molecule (H_2O, hydrohen – green, oxygen – red). **(a)** In the harmonic approximation, interatomic forces are described by harmonic springs with bond specific spring constants C_{ij}, which can be calculated with DFPT. **(b)** Solving the characteristic equations (2.25) for the water molecule yields three different vibrational patterns (illustrated by the black and blue arrows for the first and second half of the vibrational motion, respectively) and their corresponding frequencies ω.

the angular frequency of the vibration, respectively. The interatomic force constant (IFC) matrix is defined by the second derivative of the total energy

$$\mathbf{C}_{ij} = \frac{\partial^2 E}{\partial \vec{R}_i \partial \vec{R}_j} = -\frac{\partial \vec{F}_i}{\partial \vec{R}_j} \tag{2.26}$$

evaluated at $\mathrm{R}^{(0)}$ for the calculation of the normal modes. As an example, the harmonic approximation and normal modes of water (H_2O) are shown in Figure 2.2.

One very efficient method for calculating the IFC matrix without the need to actually change the geometry of the system, is Density Functional Perturbation Theory (DFPT) [40]. As a starting point, the density functional expressions for the forces in equations (2.20) to (2.23) are inserted into the definition of the IFC matrix yielding

$$\mathbf{C}_{ij} = \int \mathrm{d}^3 r \, \frac{\partial \rho(\vec{r})}{\partial \vec{R}_j} \left(\frac{\partial v_c(\vec{r})}{\partial \vec{R}_i} \right)^{\mathsf{T}} + \delta_{ij} \int \mathrm{d}^3 r \, \rho(\vec{r}) \frac{\partial^2 v_c(\vec{r})}{\partial \vec{R}_i \partial \vec{R}_j} + \frac{\partial^2 v_{c-c}(\vec{r})}{\partial \vec{R}_i \partial \vec{R}_j}. \tag{2.27}$$

The only component that is not known from the ground state of the system, is the response of the electron density to a change of the atomic positions $\frac{\partial \rho(\vec{r})}{\partial \vec{R}_j}$. The derivative of the definition of the density

$$\frac{\partial \rho(\vec{r})}{\partial \vec{R}_j} = 2\,\mathrm{Re} \sum_{\substack{n=1 \\ occ}}^{N} \phi_n^*(\vec{r}) \frac{\partial \phi_n(\vec{r})}{\partial \vec{R}_j} \tag{2.28}$$

makes clear that obtaining the density gradient is less trivial and also necessitates the calculation of the single particle wave-function gradients. In order to achieve this, the Kohn-Sham equations (2.10) are differentiated with respect to the atomic positions, which gives

$$\left(\hat{H}_{KS} - E_n\right) \frac{\partial \phi_n(\vec{r})}{\partial \vec{R}_j} = -\left(\frac{\partial v_{eff}(\vec{r})}{\partial \vec{R}_j} - \frac{\partial E_n}{\partial \vec{R}_j}\right) \phi_n(\vec{r}) \tag{2.29}$$

with the Kohn-Sham Hamiltonian $\hat{H}_{KS} = -\frac{\hbar^2}{2m_e}\nabla^2 + v_{eff}(\vec{r})$. Similar to the original Kohn-Sham equations, the gradient of the effective potential

$$\frac{\partial v_{eff}(\vec{r})}{\partial \vec{R}_j} = \frac{\partial v_c(\vec{r})}{\partial \vec{R}_j} + \frac{e^2}{4\pi\varepsilon_0} \int \mathrm{d}^3 r' \, \frac{1}{|\vec{r} - \vec{r}'|} \frac{\partial \rho(\vec{r}')}{\partial \vec{R}_j} + \int \mathrm{d}^3 r' \, \frac{\delta v_{xc}(\vec{r}')}{\delta \rho(\vec{r}')} \frac{\partial \rho(\vec{r}')}{\partial \vec{R}_j} \tag{2.30}$$

depends on the density gradient, which in turn depends on the solution of equation (2.29). Therefore, the presented system of equations is solved iteratively, as described for the Kohn-Sham equations. Note that the gradient of the Kohn-Sham-Eigenvalues

$$\frac{\partial E_n}{\partial \vec{R}_j} = \langle \phi_n | \, \frac{\partial v_{eff}(\vec{r})}{\partial \vec{R}_j} \, | \phi_n \rangle \,, \tag{2.31}$$

follows directly from the effective potential gradient and the ground-state Kohn-Sham orbitals.

In systems with periodic boundary conditions, it is more convenient to describe vibrations in the reciprocal space with a wave vector $\vec{q}$ and the dispersion relation $\omega(\vec{q})$. The aforementioned equations then also have to be transformed to their reciprocal space equivalents, but the underlying principle outlined above remains the same [40]. The reciprocal space equivalent of the IFC matrix is the dynamical matrix $\mathbf{D}_{ij}(\vec{q})$, which is connected to the real-space IFC matrix via a Fourier transformation. The eigenvalues and eigenvectors of the dynamical matrix give the vibrational frequencies $\omega(\vec{q})$ and normal modes $\mathbf{U}(\vec{q})$, respectively. On top of the more convenient description, the reciprocal-space formulation also allows to calculate vibrations with an arbitrary wave-vector $\vec{q}$ via Fourier interpolation, given that the grid for the Fourier transformation is dense enough.

So far, the pure mechanical and quantum-mechanical aspects of a vibration were considered. But for compounds with polar bonds, such as the molecules and metal oxides studied in this work, electric fields arise due to the vibration in the long wavelength limit ($\vec{q} \to 0$). This leads to additional forces, a re-distribution of the electron density, and therefore, to a change in the polarisation. Accordingly, the IFC matrix and the vibrational frequencies change as well. In reciprocal space, the influence on the dynamical matrix for $\vec{q} \to 0$ can be described by the sum

$$\mathbf{D}_{ij} = \mathbf{D}_{ij}(\vec{E} = 0, \vec{q} = 0) + \mathbf{D}_{ij}^{\mathrm{pol}}, \tag{2.32}$$

where the additional term due to the polarisation change in the unit cell with volume Ω

$$\mathbf{D}_{ij}^{\mathrm{pol}} = \frac{4\pi e^2}{\Omega} \frac{(\mathbf{Z}_i^* \vec{q}) \cdot \left(\vec{q}^{\mathsf{T}} \mathbf{Z}_j^*\right)}{\vec{q}^{\mathsf{T}} \boldsymbol{\epsilon}_\infty \vec{q}} \tag{2.33}$$

depends on the electronic dielectric tensor $\boldsymbol{\epsilon}_\infty$ and the Born effective charge (BEC, [41]) tensor $\mathbf{Z}_i^*$ of each atom. As in classical electrodynamics, the dielectric tensor describes the change of polarisation $\vec{P}$ upon a change of the electric field $\vec{E}$. Analogously, the BEC tensor describes the change of polarisation upon displacement of an atom i:

$$\mathbf{Z}_i^* = \frac{\Omega}{e} \left.\frac{\partial \vec{P}}{\partial \vec{u}_i}\right|_{\vec{q}=0, \vec{E}=0} = -\frac{1}{e} \left.\frac{\partial^2 E}{\partial \vec{u}_i \partial \vec{E}}\right|_{\vec{q}=0, \vec{E}=0} \tag{2.34}$$

Just as the dynamical and IFC matrices, both tensors are second derivatives of the total energy. Therefore, they can be calculated from DFPT in a similar manner [42].

The $\vec{q} = 0$ case is particularly important for calculating the IR spectra of adsorbate molecules on surfaces, because the incoming light only couples to changes of the polarisation due to the vibration, which is called the dynamical dipole moment. The intensity of light absorption is proportional to the square of the dynamical dipole moment. Therefore, the intensity I of each normal mode $\mathbf{U}$ follows directly from the BEC tensor via

$$I = \left| \sum_{i=1}^{M} \mathbf{Z}_i^* \vec{U}_i \right|^2 . \tag{2.35}$$

Since only relative intensities can be measured experimentally, I can be normed with an arbitrary factor I_0, for example given by the intensity of the normal mode with the highest intensity. Furthermore, contributions of the dynamical dipole parallel or perpendicular to a surface, can be separated in a straightforward manner by projecting the vectors $\mathbf{Z}_i^* \vec{U}_i$ onto the corresponding directions.

Finally, it should be noted that vibrational frequencies obtained with the method presented here, are usually shifted with respect to the experimental results, due to the harmonic and density-functional approximations [43, 44]. Even though there are recent developments towards an efficient approximate calculation of anharmonic contributions [45], and towards including quantum effects for atomic cores with low mass [46], these still come with a substantial increase in computational costs. In this work, the accuracy of the harmonic approximation and neglecting nuclear quantum effects is considered to be sufficient.

2.4 Computational surface science

In modern surface science, most research questions cannot be answered by experiments alone, but need to be guided by computational methods. As described before, calculations based on DFT are able to find the most stable atomic structure of a surface or interface. Additionally, the calculated electronic structure shows whether a molecule binds to a surface through a chemical bond (chemisorption) or simply through van-der-Waals interactions (physisorption). This section will further explain how binding energies and the stability of surfaces in different experimental conditions can be predicted from electronic and atomic structure calculations. Before these properties can be tackled, however, one has to understand how surfaces and molecules are modelled in the first place.

Periodic surface slabs

Since solid state problems usually have translational symmetry, i.e. a periodic structure, many codes for electronic structure calculations use periodic boundary conditions. However, there is no periodicity perpendicular to a surface. In other words, translational symmetry is broken in one dimension if a surface is present. To account for this breaking of symmetry without changing the basis set, and hence, the periodic boundary conditions, periodic surface slab models are built. Similar to how a surface can be cleaved from a bulk crystal in reality, surface slab models for calculations are created by cleaving the bulk structure and inserting a vacuum region (see Figure 2.3). Additionally, only one k-point is used for integration in the direction perpendicular to the surface to account for the symmetry breaking.

The size of the inserted vacuum region has to be big enough to ensure that the interaction of the surface slab with its own periodic image, due to the boundary conditions, is negligible. Since larger vacuum regions also increase the computational costs, a convergence test with respect to the vacuum size is usually performed. In most cases, a distance of 15 Å to 25 Å between periodic images is enough to obtain a reasonable accuracy.

The same applies for calculating the electronic structure and energy of an isolated molecule. In this case, translational symmetry is broken in all three dimensions. Therefore, the isolated molecule must be separated from its periodic images by a vacuum region in all three directions (see Figure 2.4). In order to avoid imposing other symmetry constraints on the electronic structure, the separation length is chosen to be different for all directions. Furthermore, integration is only performed using one k-point to account for the symmetry breaking.

But not only the size of the vacuum affects the accuracy of surface slab calculations. Another important parameter is the size of the slab itself. If the slab is too thin, the top and the bottom of the slab interact, which will result in a change of the properties. This can be desirable for the simulation of 2D-materials or thin films, but for the calculation of nanoparticle surface properties in this thesis it has to be avoided.

The size of the slab is usually measured in layers, where atoms with similar coordinates in the direction of the surface normal are considered to belong to the same layer (see Figure 2.3). Since adding more layers can increase the computational costs significantly, convergence tests are performed with respect to the number of layers. The amount of layers needed to converge a property to the desired accuracy depends a lot on the calculated property, and on the system studied. For surface relaxations and energies, for example, usually 10 to 25 layers can suffice, whereas for some electronic properties, such as the work function of a metallic surface, more than 60 layers may be needed [47].

A method to reduce the required amount of layers, is to use asymmetric surface slabs, where a number of layers at the bottom of the slab are fixed in their bulk positions. In theory, this imposes a bulk boundary condition on the atoms next to the fixed layers and makes them relax as if they were connected to bulk material. In practice, the presence of a surface at the bottom of the slab alters the electronic structure of the fixed layers compared to the bulk electronic structure. Therefore, careful testing has to be performed to check if an asymmetric surface slab really produces accurate results. On the other hand, well tested asymmetric slab models can reduce the computational costs of the following adsorption calculations significantly, because usually less layers are needed.

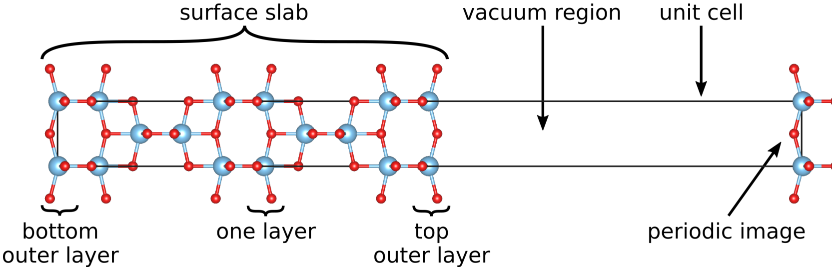

Figure 2.3: Illustration of a surface slab model of the (001) surface of anatase TiO_2 (colour code: Ti – blue, O – red). A vacuum region separates the slab from its periodic image, producing two surfaces in the unit cell on the top and bottom of the slab.

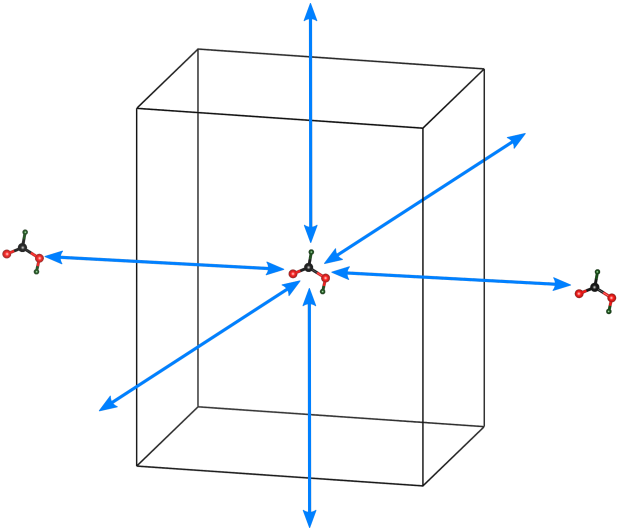

Figure 2.4: Illustration of an isolated molecule model of formic acid (HCOOH, colour code: H – green, C – black, O – red). The molecule is separated from its periodic images by vacuum space in all three directions.

The periodicity along the surface also plays an important role in surface science, because it determines which structures can be studied computationally. Many real surfaces have a structure similar to the surface created from cleaving the bulk, as described before. These bulk truncated surfaces only change their structure slightly by *relaxations* that can be calculated with DFT. Relaxations appear on all surfaces due to the missing chemical bonds compared to the bulk, which is why the outermost layer usually relaxes inwards. Apart from simple relaxations, it is also possible that the surface structure deviates significantly from the bulk truncated surface, which often results in a change of the periodicity along the surface. Therefore, modelling these *reconstructed* surfaces necessitates larger surface slab models with the appropriate periodicity. In order to make the size of the surface unit cell more apparent, the notation $(a \times b)$ is used, where a and b denote the relative increase in the size of the unit cell vectors compared to the bulk truncated (1×1) surface. Famous examples include the (7×7) reconstruction of the silicon (111) surface [48] or the $(1{\times}2)$ reconstruction of the rutile TiO_2 (110) surface [49], which sparked a lot of discussions and research in the surface science community. In this regard, diffraction experiments, such as surface X-ray diffraction (SXRD) or low-energy electron diffraction (LEED), provide valuable information for building the surface slab model.

Adsorption energies

The adsorption energy E_{ads} is defined as the energy change when one molecule attaches to (adsorbs on) a surface coming from an infinitely distant starting point. This process can be formally written as the chemical reaction

$$\mathrm{slab} + \mathrm{mol} \longrightarrow \mathrm{slab{-}mol_{ads}}. \tag{2.36}$$

Accordingly, the adsorption energy is the energy change of this reaction and can be calculated from

$$E_{\mathrm{ads}} = E_{\mathrm{slab-mol}} - (E_{\mathrm{slab}} + E_{\mathrm{mol}}), \tag{2.37}$$

where $E_{\mathrm{slab-mol}}$, E_{slab}, and E_{mol} are the energies of the adsorption structure, the surface slab without an adsorbate, and the molecule alone, respectively. As described in the previous section, even with periodic boundary conditions the "infinitely distant starting point" can be approximated by placing the molecule in a sufficiently large cell and creating a sufficiently large vacuum between periodic images of surface slabs. If the molecule is large or a low coverage shall be simulated, more than one unit cell of the surface might be needed for the slab$-$mol$_{\mathrm{ads}}$ structure. On the other hand, at high coverage, more than one molecule may fit in one surface unit cell. Therefore, equation (2.37) has to be generalized to the case of M surface unit cells and N molecules, resulting in

$$E_{\mathrm{ads}} = \frac{1}{N}[E_{\mathrm{slab-mol}} - (M \cdot E_{\mathrm{slab}} + N \cdot E_{\mathrm{mol}})]. \tag{2.38}$$

Note that the adsorption energy is defined per molecule and is usually a function of the surface coverage.

Within this definition, the adsorption energy is negative, if the adsorption is energetically favourable, i.e. if the energy of the adsorption structure is lower than the combined energies of the separated surface and molecule. Therefore, a lower or more negative adsorption energy corresponds to a stronger binding to the surface. Since this sometimes makes the discussion of the binding strength somewhat confusing, the binding energy E_{B} is defined as the negative adsorption energy

$$E_{\mathrm{B}} = -E_{\mathrm{ads}}. \tag{2.39}$$

It describes how much energy is needed to remove the adsorbate from the surface and therefore corresponds to the binding strength. Both quantities, adsorption and binding energy, may be used in the discussion of the results throughout this thesis, depending on which quantity provides more clarity, but only adsorption energies will be shown as results in tables.

Surface free energies

Surface free energies are needed to assess and compare the stability of surface structures in different chemical environments. The surface free energy is defined as the Gibbs free energy ΔG per surface area A for creating that specific surface. Hence, a surface with a lower surface free energy is more likely to form (see Section 2.5). Using the same concept as for the adsorption energies, one can write the surface formation process as a chemical reaction

$$n \cdot \text{bulk} \longrightarrow \text{slab}, \tag{2.40}$$

where n units of a bulk material form the surface slab resulting in a surface free energy of

$$\gamma = \frac{\Delta G}{A} = \frac{1}{A}(G_{\text{slab}} - n \cdot G_{\text{bulk}}). \tag{2.41}$$

Sometimes molecules may be involved in the surface formation process, especially when creating surface structures with different oxidation states or with adsorbate molecules present on the surface. The reaction can then be generalized to

$$n \cdot \text{bulk} + \sum_i n_i \cdot \text{reactant}_i \longrightarrow \text{slab} + \sum_j m_j \cdot \text{product}_j, \tag{2.42}$$

where an arbitrary number n_i of each reactant can take part in the reaction and an arbitrary number m_j of each product different than the created surface slab can be taken into account. Here, the created surface slab, denoted as "slab", can also be the adsorption structure, denoted as "slab$-$mol$_{\text{ads}}$" in the previous section. According to its definition, the surface free energy for this generalized surface creation reaction is

$$\gamma = \frac{1}{A}\left[\left(G_{\text{slab}} + \sum_j m_j G_j\right) - \left(n \cdot G_{\text{bulk}} + \sum_i n_i G_i\right)\right]. \tag{2.43}$$

Since the Gibbs free energies G of the different reactants and products depend on their temperature, pressure, and concentration, different surface structures can be stabilised (i.e. γ can be lowered) by changing the chemical environment of the surface formation reaction. However, a direct prediction of the Gibbs free energies from electronic structure calculations would require a very costly simulation of the molecular dynamics in an (N, p, T) ensemble, where the number of particles N, the pressure p, and the temperature T can be controlled directly. Nevertheless, it is possible to approximate the surface free energy γ from static calculations in a $(N, V, T = 0\,\text{K})$ ensemble, with fixed volume V, and within the limit of a temperature of 0 K.

To go from a $(N, V, T = 0\,\text{K})$ ensemble to a (N, p, T) ensemble, two steps need to be performed. First, the corresponding thermodynamic potentials have to be transformed, according to the $V \leftrightarrow p$ transition. Second, the effect of temperature has to be included.

The transition from a pressure based description to a volume based description, and vice versa, can be expressed by the Legendre transformation

$$F(N, V, T) = G(N, p(N, V, T), T) + p(N, V, T) \cdot V, \tag{2.44}$$

where F is the Helmholtz free energy of the system. However, in the typical pressure/volume ranges of the surface science questions at hand, the product $p \cdot V$ has a very small (less than $0.1\,\mathrm{meV\,\AA^{-2}}$ or $2\,\mathrm{mJ\,m^{-2}}$) contribution to the surface free energy. Therefore, the first approximation is to neglect this term and assume $G \approx F$.

For the inclusion of temperature effects, the Helmholtz free energy is split into a contribution at 0 K and a contribution due to temperature effects. The electronic structure calculations described in Section 2.1 allow to evaluate the inner energy $E(N, V, T = 0\,\mathrm{K})$ of the system in the electronic ground state at 0 K. The difference to the Helmholtz free energy is that zero-point vibrations are not included, since only fixed configurations are considered. Therefore, the total Helmholtz free energy can be expressed as the sum

$$F(N, V, T) = E(N, V, T = 0\,\mathrm{K}) + F_{\mathrm{ZPV}}(N, V, T = 0\,\mathrm{K}) + \Delta F(N, V, \Delta T), \tag{2.45}$$

where F_{ZPV} denotes the contribution of zero-point vibrations, and ΔF accounts for the temperature dependence. Inserting this into equation (2.43) yields

$$\gamma = \gamma_0 + \Delta\gamma_{\mathrm{slab/bulk}} + \Delta\gamma_{\mathrm{mol}} \tag{2.46}$$

with

$$\gamma_0 = \frac{1}{A}\left[\left(E_{\mathrm{slab}} + \sum_j m_j E_j\right) - \left(n \cdot E_{\mathrm{bulk}} + \sum_i n_i E_i\right)\right]$$

$$\Delta\gamma_{\mathrm{slab/bulk}} = \frac{1}{A}\left[\left(F_{\mathrm{slab}}^{\mathrm{ZPV}} + \Delta F_{\mathrm{slab}}\right) - n \cdot \left(F_{\mathrm{bulk}}^{\mathrm{ZPV}} + \Delta F_{\mathrm{bulk}}\right)\right]$$

$$\Delta\gamma_{\mathrm{mol}} = \frac{1}{A}\left[\sum_j m_j \left(F_j^{\mathrm{ZPV}} + \Delta F_j\right) - \sum_i n_i \left(F_i^{\mathrm{ZPV}} + \Delta F_i\right)\right]$$

The first of these contributions, γ_0, follows directly from the electronic structure calculations. The second contribution, $\Delta\gamma_{\mathrm{slab/bulk}}$, describes the difference between surface and bulk regarding vibrational and thermal energies. $\Delta\gamma_{\mathrm{slab/bulk}}$ was shown to be negligible, since it only contributes with less than $10\,\mathrm{meV\,\AA^{-2}}$ (or roughly $0.1\,\mathrm{J\,m^{-2}}$) to the surface free energies in the temperature range until 1000 K [50]. The contribution from molecules reacting with or stemming from reactions with the surface, $\Delta\gamma_{\mathrm{mol}}$, is more significant. Usually, it is expressed in terms of the chemical potential shifts $\Delta\mu$ as

$$\Delta\gamma_{\mathrm{mol}} = \frac{1}{A}\left(\sum_j m_j \Delta\mu_j - \sum_i n_i \Delta\mu_i\right). \tag{2.47}$$

This offers the advantage of including not only the effect of temperature and pressure on the surface free energy, but also the influence of the concentration of the components (i and j) in the surrounding medium. Furthermore, chemical potentials of many simple molecules can be easily accessed through computations or from experimentally obtained thermochemical databases [51]. For an ideal gas, the connection of $\Delta\mu$ to the pressure and temperature of the system is given by

$$\Delta\mu(p,T) = \Delta\mu(p^\circ,T) + k_\mathrm{B}T\ln\left(\frac{p}{p^\circ}\right), \tag{2.48}$$

where p° is the standard pressure of 1 bar. The chemical potential shift at standard conditions $\Delta\mu(p^\circ,T)$ can be obtained from thermochemical tables or calculated with accurate ab-initio methods. Moreover, plotting the surface free energy versus the relevant chemical potential shifts can help to identify stability regions of important surface phases, even when the functional connection between chemical potential and experimental conditions is not known explicitly.

2.5 Prediction of equilibrium particle shapes

During synthesis, particles can grow at different rates in the different crystallographic directions. This is caused by the differences in the stability and reactivity of the particles' surfaces. In many cases, stability and reactivity are connected, meaning that a low stability of a surface leads to a higher reactivity. Therefore, the particle grows faster in the direction normal to a surface with low stability. As a result, the final particle mainly exhibits surfaces with high stability, which also determines the shape of the particle.

For the thermodynamic equilibrium state, the final shape of a single crystal particle can be predicted by minimising the Gibbs free energy ΔG of that particle. It can be split up into a contribution from the volume ΔG_v and a contribution from the surface ΔG_s:

$$\Delta G = \Delta G_v + \Delta G_s \tag{2.49}$$

However, for the prediction of the shape at a fixed volume, the volume free energy ΔG_v is constant and only the Gibbs surface energy

$$\Delta G_s = \sum_j \gamma_j A_j \tag{2.50}$$

needs to be minimised, where the summation runs over all surfaces, and γ_j and A_j are the corresponding surface free energy and surface area, respectively.

In 1901 G. Wulff proposed a geometric solution to this minimisation problem [52]. As illustrated in Figure 2.5 for a 2-dimensional case, in the Wulff construction a polar plot of the surface free energies is drawn, which can be scaled according to the particle size. Next, a line perpendicular to the corresponding surface normal is drawn at each point of the plot. The minimal area enclosed by these lines then gives the equilibrium particle shape. In the 3-dimensional case, the Wulff construction works in an analogous manner,

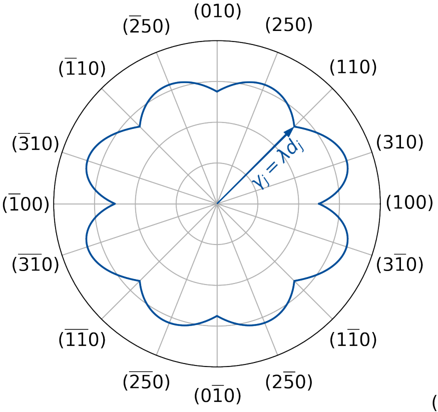

(a) Polar plot of the surface energies γ_j depending on the surface normal (hkl). The radial scale is arbitrary and can be chosen proportional to the particle size.

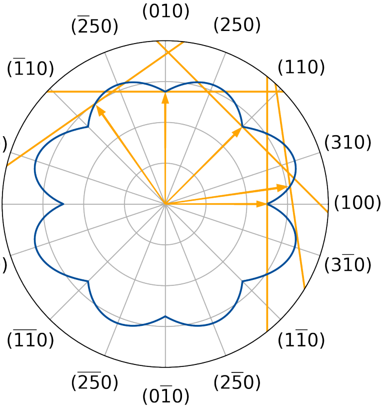

(b) Lines perpendicular to the surface normals are drawn on all points of the polar plot (only some examples are illustrated here for clarity).

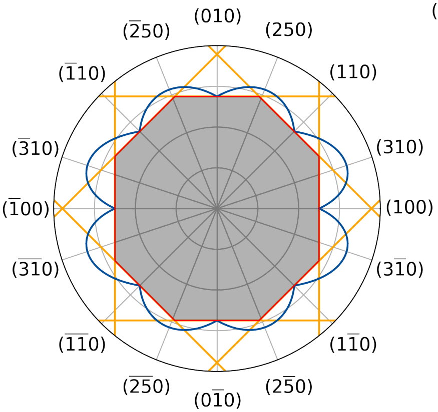

(c) The smallest volume enclosed by the lines gives the particle's shape and stable facets.

Figure 2.5: Illustration of the Wulff construction in two dimensions.

with planes drawn perpendicular to the surface normal in a distance from the centre of the particle proportional to the surface free energy.

The minimisation of ΔG_s by the Wulff construction was later shown analytically by different researchers [53–55]. For example, using the variational principle for a fixed volume of the particle, one obtains the minimisation condition

$$\delta(\Delta G_s) = \delta\left(\sum_j \gamma_j A_j\right) = \sum_j \gamma_j \delta(A_j) = 0, \tag{2.51}$$

because the surface free energy γ_j is a constant. On the other hand, minimising ΔG_s for a fixed volume V also means that $\delta V = 0$. Expressing the volume V in terms of the surface areas A_j and their distances to the centre of the particle d_j, this yields

$$\delta V = \delta\left(\frac{1}{3}\sum_j d_j A_j\right) = \frac{1}{3}\left(\sum_j d_j \delta(A_j) + \sum_j A_j \delta(d_j)\right) = 0. \tag{2.52}$$

However, the latter sum is equal to zero, because increasing one distance d_k would result in a decrease of the other distances for fixed volume and surface areas of the particle. Therefore,

$$\sum_j d_j \delta(A_j) = 0 \tag{2.53}$$

is obtained as the second minimisation condition, which can be combined with Equation (2.51) using an arbitrary factor λ:

$$\sum_j (\gamma_j - \lambda d_j)\delta(A_j) = 0 \tag{2.54}$$

Since in general $\delta(A_j) \neq 0$, the distance to the particle's centre has to be proportional to the corresponding surface free energy ($\gamma_j = \lambda d_j$), which is the basis of the Wulff construction.

It should be stressed again, that the Wulff construction only gives a reasonable approximation of the particle shape in the thermodynamic equilibrium. Furthermore, effects of the increased energy at the edges and corners of the particle are not accounted for. A more accurate prediction of the particle shape and detailed insight into growth mechanisms can be gained by employing nucleation and growth simulations on the basis of molecular dynamics calculations, such as the Kawska-Zahn approach [56]. J. Anwar and D. Zahn published an excellent review on these methods [57]. They are, however, computationally much more demanding than the simple Wulff construction, especially on the DFT level of theory. Therefore, the Wulff construction is employed in this work as a reasonable first approximation of the real particle shape.

3

Adsorption structure search

The energy of an atomic configuration can be optimised with the help of atomic structure calculations, such as the ones described in Chapter 2. In these kind of calculations, the atomic positions are changed along the gradient of the potential energy surface (PES), in order to find a minimum of this complex high-dimensional function. However, the optimisation algorithms do not necessarily yield the atomic structure with the absolute lowest energy, i.e. the global minimum of the PES, but rather the structure of a local minimum close to the starting configuration. Therefore, it is important to perform multiple calculations starting from different configurations or apply other methods that sample the PES more exhaustively than a single structural optimisation. Figure 3.1 exemplifies this fact for a structure of two hydrogen and two fluoride atoms. It follows that even structures consisting of very few atoms can have different stable configurations corresponding to different local minima in the PES. Furthermore, the example shows the importance of knowing more about the different local minima and the global minimum. The comparison of the energies of different local minima allows to calculate reaction enthalpies. In the example of Figure 3.1, one could predict if the reaction $H_2 + F_2 \rightleftharpoons 2\,HF$ is exothermic (HF is energetically favourable) or endothermic ($H_2 + F_2$ is energetically favourable). The global minimum of the PES is the thermodynamically most stable state (at 0 K), since all reactions to this state are exothermic. Therefore, many systems are described well by this ground state configuration of the system. Furthermore, chemical reactions start and end in (meta-)stable configurations, which is why a knowledge of the different local minima of the PES also helps to study reaction rates and barriers.

In this work, a search for the most stable adsorption structures of carboxylic acids on transition metal oxide surfaces is important to identify relevant interface structures, and accurately predict their binding energies and other properties that evolve from these, such as the shape of TiO_2 nanoparticles. This chapter first provides a short introduction to the challenges and current approaches for adsorption structure search, as well as the existing in-house code that was developed for this purpose by the group of Prof. Stefan Müller at TUHH, with the initial idea outlined in the Diploma thesis of B. Elsner [58] and then further developed in the PhD thesis of W. Heckel [59]. In the course of this thesis, the in-house code was completely re-written and improved in several aspects, in order to solve existing issues, make the program more open

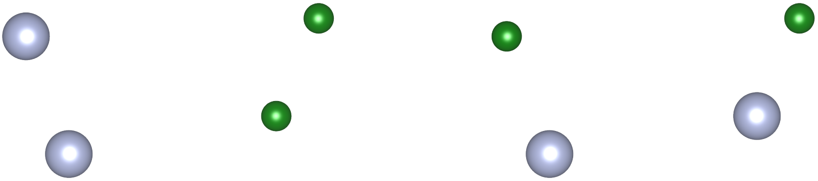

(a) $\mathrm{H + H + F + F \longrightarrow H_2 + F_2}$ **(b)** $\mathrm{H + H + F + F \longrightarrow 2\,HF}$

Figure 3.1: The influence of the starting configuration on the resulting optimised structure illustrated for a structure consisting of two hydrogen atoms (H, green) and two fluorine atoms (F, silver). If atoms of the same species are placed close to each other (a), the closest minimum energy configuration consists of a hydrogen molecule and a fluorine molecule. If the atoms of different species are placed close to each other (b), the closest minimum energy configuration consists of two hydrogen fluoride molecules.

and user-friendly, and to include up-to-date machine learning techniques. The second part of this chapter explains the functionality of the new program, called *Configuration space determination and Reduction* (`CodeRed`), and the paradigms it builds on. Finally, further possible steps for improvement are outlined.

3.1 Introduction to adsorption structure search

The most challenging aspect of finding the energetically most favourable adsorption structure is the "curse of dimensionality". Neglecting symmetry constraints, each additional atom adds three degrees of freedom to the configuration space, and hence, the potential energy surface (PES). This complicates finding the minimum energy by increasing the search space and adding more local minima to the PES. In fact, it can be shown that the number of local minima increases exponentially with the number of atoms in the system [60]. This can be understood from the simple example in Figure 3.1: If the structure would only consist of one hydrogen atom and one fluorine atom, there would be only one degree of freedom, the distance between both atoms, and only one energy minimum corresponding to a HF molecule. Doubling the system to two hydrogen and two fluorine atoms increases the number of degrees of freedom to six, and creates more local minima in the PES – the ones discussed before and further, less intuitive minima, such as configurations with single atoms in vacuum or different trimers and tetramers. The presence of a surface on which the molecule can adsorb, does not improve the situation. Since the surface breaks the translational and rotational invariance of the configuration space, meaning that now it matters how a molecule is oriented and where it is placed with respect to the surface, the number of degrees of freedom increase further.

In the aforementioned example of one hydrogen and one fluorine atom, not only the distance between those atoms determines their energy when they are placed close to a surface, but also their distances to the different surface atoms. Therefore, even studying the adsorption of single atoms and small molecules necessitates a thorough adsorption structure search.

State of the art

Several approaches to lift the curse of dimensionality, while keeping the accuracy of ab-initio electronic structure calculations, have been made in the past years. One prominent example is the Ab-Initio Random Structure Search (AIRSS) method [61, 62]. It creates random structures with a sensible atom density, and then imposes further constraints before performing structural relaxations with ab-initio methods. At first, the approach was mainly applied to find stable structures of solids, such as the high pressure phases of silane [61], alumina [63] , and ammonia [64], but later it was also applied to surface science investigations, such as finding the active sites for hydrogen evolution on pyrites [65] or to identify the adsorption sites of lithium ions on molybdenum disulphide [66]. Searching for stable structures with the AIRSS method is very unbiased and hence, easy to automatise. However, it also requires the generation and evaluation of many structures that might not be of interest for a particular investigation. Furthermore, the preselection of structures only considers their density, symmetry, and connectivity, but not the similarity of the selected structures.

More recently developed approaches, which are more targeted on adsorption structure search, employ mathematical tools, such as graph theory [67] or Bayesian optimisation [68], to preselect interesting structures. The Bayesian Optimisation Structure Search (BOSS) technique [68] aims to accelerate the structure search by using the information from previously evaluated structures to calculate error estimates and propose new structures. So far, BOSS was employed to investigate stable adsorption modes of C_{60} on TiO_2 surfaces [68], as well as camphor [69] and tetracyanoethylene [70] on a copper surface. The strength of the approach lies in the very efficient sampling of the configuration space, with a focus on finding the minimum energy adsorption structure with a minimum amount of iterations. In addition, the method creates a surrogate model of the PES, which can serve as a good first estimate for further calculations. However, the application is limited to molecules with a restricted amount of degrees of freedom, since each degree of freedom has to be specified manually. Furthermore, the iterative nature of the optimisation procedure can slow down the structure search when a larger number of samples is needed. In that case, a more parallelised approach might work faster, even though the overall computational cost can be higher.

Apart from these approaches, which try to find bound states and foremost the global minimum of the PES by sampling the configuration space efficiently, there are also several methods more suited for flat PESs. These are relevant, for example, when modelling transition states in chemical reactions. Notable examples include techniques such as simulated annealing [71], metadynamics [72] or a combination of metadynamics with umbrella sampling [73]. In summary, there are many methods for sampling the PES in general, and depending on the goal of the structure search, different approaches might be preferable. Nevertheless, the availability of methods targeted at adsorption structure search is limited and not satisfactory, which is why another approach is chosen here.

The method that is developed further in this thesis builds on an idea by B. Elsner and W. Heckel [58, 59]. They created a program that assembles adsorption configurations atom by atom, including already existing knowledge about typical bond lengths and angles, in order to create realistic adsorption structures. For each atom, a three-dimensional mesh of possible positions is created with an individual mesh width. Then, the configurations that do not fulfil the boundary conditions for bond lengths and angles specified by the user are excluded. The boundary conditions in this approach should be loose enough to allow exhaustive sampling of the configuration space, but tight enough to limit the amount of configurations, in order to make sure that they still fit into the memory of the machine on which the program is running[1]. A coarse graining approach was introduced, which further reduces the amount of resulting configurations, with the aim of minimising redundant calculations for similar structures. The implemented algorithm divides the unit cell into coarse graining boxes, and assigns each atom in a configuration to the box it is in. Two configurations are then regarded as similar, when they have the same box pattern or the box patterns are symmetrically equivalent, and one of the similar configurations is removed.

Parts of the configuration that are not expected to change their internal structure upon adsorption, such as the methyl ($-CH_3$) end group of a carboxylic acid, can be excluded from the configuration search and inserted back into the different configurations afterwards. The obtained structures can then be relaxed on the ab-initio level (for example using DFT), and their energies are calculated and compared. In principle, this approach is similar to the aforementioned AIRSS method, but the configuration space is sampled more systematically and without randomness here. Furthermore, the inclusion of more boundary conditions and the use of the coarse graining algorithm can lead to a much lower number of structures that have to be evaluated in order to find the most favourable one.

Potential for further development

Even though the method and the corresponding tool by Elsner and Heckel was successfully applied to find new favourable adsorption structures of acetone [43] and benzoic acid [74] on TiO_2 surfaces, there are several aspects that need to be improved. The most important point concerns the coarse graining

---

[1] It is much easier to reach this memory limit than one might think. Without boundary conditions, creating and storing configurations from meshes with 1000 possible positions for four atoms already results in $4 \cdot 10^3 \cdot 10^3 \cdot 10^3 \cdot 10^3 \cdot 4\,\mathrm{Byte} \approx 16\,\mathrm{TB}$ of memory or disk space.

algorithm. There, the representation of atomic structures by boxes makes it possible that very similar structures are not detected to be similar. As an example, look at the two structures of a formic acid molecule in Figure 3.2, that have the same positions of all atoms except for the one hydrogen atom on the top. This one atom is very close to the boundary between two boxes, but for structure (a) it is on one side of the boundary and for structure (b) it is on the other side. Hence, the box representations of both structures will be different and the algorithm is not able to detect their similarity. Therefore, both structures would be passed on to be treated with more expensive methods, even though an experienced computational materials scientist knows that they will most likely relax to the same structure.

The other points for improvement are concerning the implementation of the method in computer code. The software written by Elsner and Heckel is a MATLAB® script that also makes use of the symmetry detection of the universal cluster expansion (UNCLE) [75] in the MedeA® modelling suite. Therefore, it depends heavily on proprietary software, and possible future users would also need to buy licences for these software packages. Another practical issue of the code, is that each atom of the adsorption structure is implemented explicitly in the code with functions dedicated to this atom only. That means, that for each additional atom, new code has to be added, which leads to a limitation of six atoms in the configuration and a lot of redundant programming. Furthermore, the feature that allows to add parts of the adsorbate molecule after the configuration search, is limited to methyl

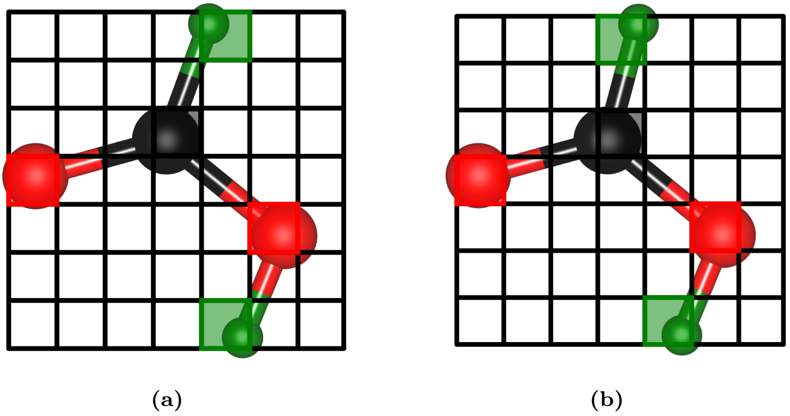
(a)

(b)

Figure 3.2: Box representation for two formic acid molecules, with almost exactly the same structure. The only difference is that the top hydrogen atom in (a) is shifted by 0.1 Å compared to (b), which nevertheless, yields a different box representation. Colour code: O – red, C – black, H – green.

($-CH_3$) and hydrogen ($-H$, $-H_2$, $-H_3$) end groups. Therefore, the possible adsorbates that can be studied, are limited to molecules with up to six atoms, plus some small side groups.

3.2 Configuration space determination and Reduction (`CodeRed`)

In order to resolve the aforementioned issues, the original idea by Elsner and Heckel is developed further into a more generalised tool for configuration space sampling in this thesis. Furthermore, a new implementation of the method is written, in order to make it easily available and to simplify the usage. The new tool is named ***CodeRed***, standing for *Configuration space determination and Reduction*. This section explains the new method and the new features of the software tool.

`CodeRed` was developed and written with the following goals in mind:

- There should be no limitation to the type of structure that can be built.
- State-of-the-art machine-learning tools should be used for the selection of dissimilar structures.
- Only open source software should be required to run `CodeRed`.
- It should be possible to operate `CodeRed` interactively and in scripts.

The first goal, of lifting the limitation to adsorption structures with six adaptable atoms, is clearly related to the drawbacks of the existing code. A program for building and preselecting adsorption structures should be able to be applied to any molecule of interest. Achieving the second goal, of employing machine-learning tools for the preselection of dissimilar structures for further in-depth study, presents a methodological advancement. The advent of machine-learning techniques for computational materials science in the past two decades has provided us with ample tools for representing and comparing atomic structures, while respecting their permutational, translational, and rotational invariants [76]. Furthermore, modern unsupervised machine-learning tools[2], such as dimensionality reduction or clustering algorithms, enable a better understanding and sampling of the configuration space. The last two goals consider the usability of `CodeRed`. Since the program is designed to help with the set-up and configuration space sampling of any adsorption structure calculation, it should be compatible with any atomistic simulation code. Therefore, `CodeRed` should be an open-source software, which allows users to adapt it to their particular simulation environment. Furthermore, a wider portion of the

---

[2] Machine-learning tools are usually categorised into *supervised* and *unsupervised* methods. Supervised tools predict a property y of a new data point $\vec{x}$ from a dataset of points $\vec{x}_i$ with known properties y_i, whereas unsupervised tools try to extract information from a dataset of points $\vec{x}_i$ with unknown properties y_i, which gives insight into the structure of the dataset. For a basic practical introduction to machine learning in general, the interested reader may refer to [77] or [78].

atomistic simulations community can be reached with an open-source software. Finally, the possibility to operate `CodeRed` interactively is important, since exploring the configuration space is an iterative process that often needs adjustment of the input parameters. A complete restart of the program after each adjustment would slow this process down and make it more tedious.

General structure of `CodeRed`

`CodeRed` makes use of object-oriented programming, which means that the input parameters, calculation methods (also called functions), and the resulting structures, are stored in a `CodeRed` object and other related objects[3]. The most important methods of the `CodeRed` object are `code()` and `red()`. In accordance with the name of the program, the method `code()` determines the available configuration space, while the method `red()` is called to reduce the number of configurations to save computational costs in further calculations.

A process flow chart for the `code()` method is shown in Figure 3.3. When the method for configuration space determination is called, it iteratively adds atoms to the adsorption structure until all atoms are added. For each atom, it starts by creating a grid of possible positions. Then, for all the possible structures that arise from the combination of the existing structures with the new positions, `code()` checks the compliance with the boundary conditions for bond lengths and bond angles that were specified by the user. All combinations that do not comply are excluded from further analysis and the program moves on to the next atom. If all combinations are excluded at some point, which can happen, for example, when the user specified too narrow boundary conditions, the method stops the calculation, allowing the user to adjust the input parameters. When all atoms are added, the list of combinations is converted to a list of atomic structures that represents the available configuration space.

The user can then obtain this list of structures and perform further analysis or pass it on to the `red()` method, in order to reduce the amount of structures. Figure 3.4 illustrates how the reduction process is implemented. First, the atomic positions in each structure are transformed into features. For now, the features can be seen as a way to make structures easier to compare, but a more detailed explanation will be given later-on. Based on the features, the similarities for each pair of structures are calculated, and dissimilar structures are selected. The user can then decide whether or not further reduction is necessary to limit the computational costs to a reasonable amount. Finally, parts of the molecule that are not expected to change their geometry significantly upon adsorption can be added to the adsorption structure as side chains.

As an example, the creation of adsorption positions for a single oxygen atom on the (111) surface of magnetite (Fe_3O_4) is shown in Figure 3.5. All the small circles represent the grid of possible positions that is created in the

---

[3] An in-depth knowledge of programming techniques is not required in order to understand this section. The interested reader may refer to source [79] for an introduction to programming in Python, including object-oriented programming.

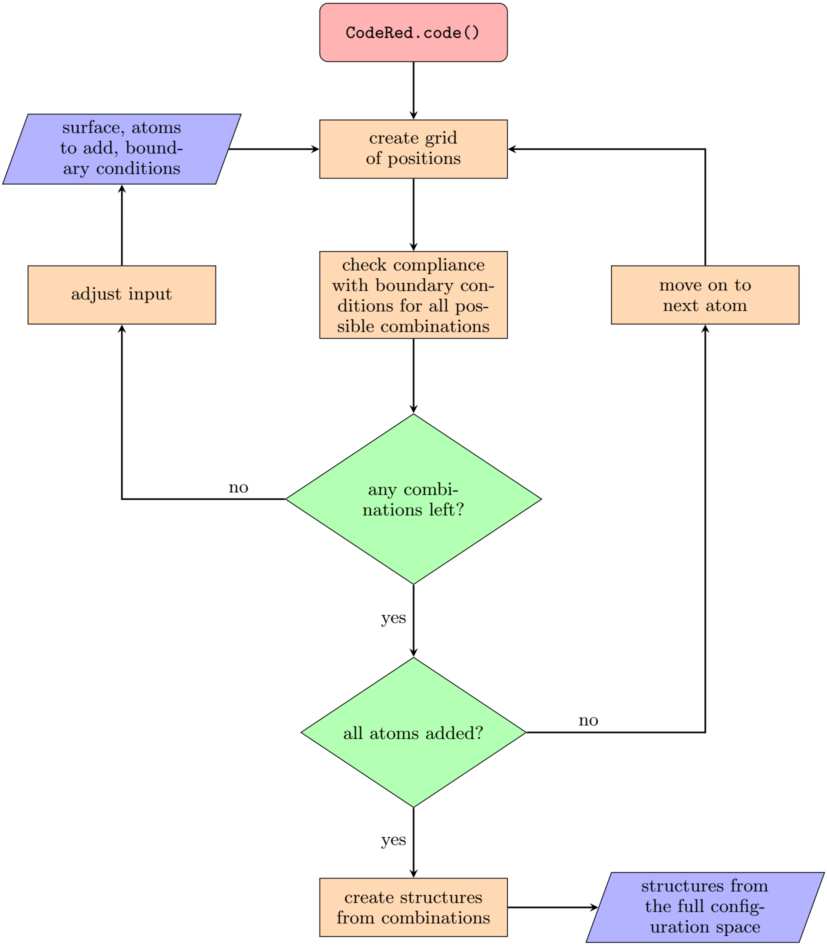

Figure 3.3: Process graph of the `code()` method implemented in `CodeRed` (easiest to read along the centre column). Processes are depicted as orange rectangles, while data used as input or output are shown as purple parallelograms, and decisions are represented by green diamonds. The user provides all necessary input parameters and adjusts the input, if `CodeRed` fails to find any combinations fulfilling the boundary conditions (left column). Otherwise, `CodeRed` automatically creates reasonable adsorption structures, sampling the defined configuration space.

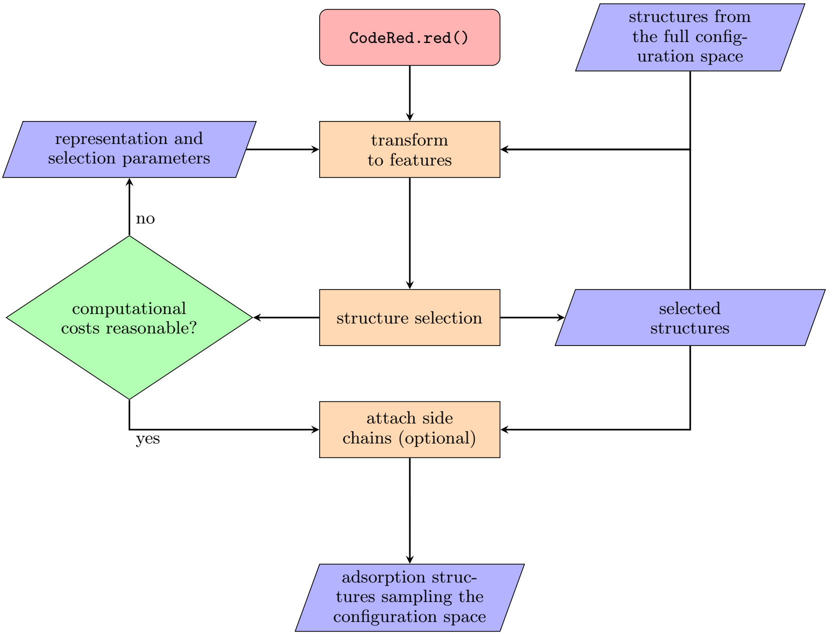

Figure 3.4: Process graph of the `red()` method implemented in `CodeRed` (easiest to read along the centre column). Processes are depicted as orange rectangles, while data used as input or output are shown as purple parallelograms, and decisions are represented by green diamonds. The user sets the parameters for how the structures are represented and selected, and decides how many structures can be treated with computationally more expensive tools (left column). `CodeRed` reduces the number of structures for sampling the configuration space accordingly and produces adsorption structures ready for usage in electronic structure calculations.

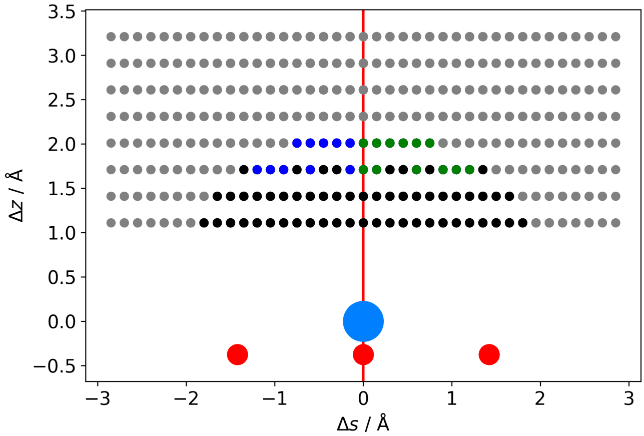

(a) side view

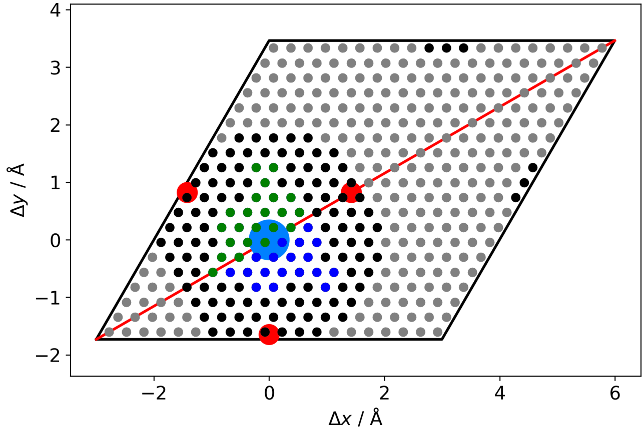

(b) top view

Figure 3.5: Example of the `CodeRed` approach for the adsorption of one oxygen atom on the magnetite (111) surface. The surface unit cell is shown with a black line in the top view, with a red line marking a mirror symmetry plane. The topmost iron and oxygen atoms of the surface are visualised as big circles in light blue and red, respectively. Possible adsorption positions are depicted as small circles whose colours indicate which condition leads to their exclusion from further analysis: grey – distance to Fe atom, black – distance to O atoms, blue – symmetrically equivalent, green – not excluded.

first step of the `code()` method. The grid usually spans the whole unit cell, but can be limited through position boundary conditions, as can be seen here for the extension of the grid in z-direction. From other studies on transition metal oxide surfaces, it is known that an oxygen atom will bind to a metal atom on the surface. Therefore, a distance boundary condition is applied that forces the Fe−O bond length to be in the range of 1.8 Å to 2.2 Å, and thereby excludes the positions marked in grey. Furthermore, due to the repulsive Coulomb forces between Oxygen atoms, their distances to each other are usually larger than 2.5 Å. Applying this boundary condition excludes the black circles, leaving only the positions marked in blue and green. However, many of these remaining adsorption positions are symmetrically equivalent, because of the mirror symmetry of the unit cell, indicated as a red line in Figure 3.5. Therefore, the `red()` method is invoked with parameters to perform a symmetry reduction, which almost halves the number of positions to study (blue marked positions are excluded). A closer look reveals that the threefold rotation symmetry of the surface did not lead to a reduction of the possible positions, because the grid is not centred around the threefold symmetry axis on the iron atom. This already indicates that a similarity metric, which allows small deviations from exact symmetrical equivalence, would be more suited to compare and select structures.

Arbitrary adsorption structures

In theory, an arbitrary number of atoms can be added to the adsorption configuration with the described program structure. Each atom from the adsorption structure added to `CodeRed` is an `AdAtom` object that stores all boundary conditions associated with this atom, as well as its grid of possible adsorption positions and other basic properties. Therefore, the single atoms can be added consecutively until the whole structure is included, and the order of atoms can be changed easily. Furthermore, the properties and boundary conditions of each `AdAtom` can be accessed and modified for successive runs. If desired, the creation of the `AdAtom` objects from a molecule that shall be adsorbed on a surface can also be scripted by the user. However, this possibility should be utilized with care, since the inclusion of existing knowledge about the adsorption structure and chemical intuition through the boundary conditions is an integral part of the tool.

`CodeRed` stores the positions of all atoms in the remaining combinations as a $N \times M \times 3$ matrix, where N is the number of combinations and M is the number of atoms in each combination. Therefore, a practical limitation to the number of `AdAtoms` that can be added arises from the memory of the machine on which `CodeRed` is executed. Without boundary conditions, the number of possible combinations scales exponentially with the number of atoms in the structure, leading to a matrix with $3M \cdot \prod_{i=1}^{M} n_{\mathrm{grid},i}$ entries that have to be kept in the memory, where $n_{\mathrm{grid},i}$ is the number of grid points for atom i. Therefore, creating configurations with many atoms can easily exceed the available memory. Possible solutions are to reduce the number of grid points by employing a coarser grid, and to tighten or add boundary conditions, both of which lead to a less exhaustive sampling of the configuration space. In general, it is preferable to include as much of the existing knowledge about the adsorption configuration as possible through boundary conditions, and only then increase the mesh width of the positions grid. The flexibility of `CodeRed` also allows to invoke reduction algorithms implemented in the `red()` method on intermediate steps, in order to reduce the amount of combinations with further atoms. It is up to the user to decide which route or combination of routes to follow in order to include more and more atoms. It should be noted, though, that for very large structures it may be more efficient to employ random sampling of the configuration space, as implemented in AIRSS [62] or make use of the side chain feature of `CodeRed` to add parts of the molecule after the configuration search.

The side chain feature makes `CodeRed` a very powerful tool for the creation of adsorption structures of molecules with a mixture of rigid and flexible parts. The configuration space of the flexible parts is fully sampled with the aforementioned methods, while the rigid parts are only added after the reduction process is finished. `CodeRed` allows to add an arbitrary number of side chains, and automatically calculates their positions and orientations for each configuration, based on only a few input parameters provided by the user.

Representations and selection algorithms

The reduction of the number of configurations to sample the configuration space is a core element of `CodeRed`. The aim of the reduction process is to create a subset of structures, which are as dissimilar as possible, while still maintaining a good representation of the space of potential adsorption configurations. Ideally, each starting configuration relaxes to a different local minimum, which would mean that each calculation gathers additional information about the configuration space. In general, the dissimilarity between two structures can be expressed as a distance

$$D_{ij} = \|\vec{q}_i - \vec{q}_j\| \tag{3.1}$$

in the configuration space, where $\vec{q}_i$ and $\vec{q}_j$ are feature vectors describing the structural properties of structures i and j, respectively. Following this definition, two structures with a low distance are very similar and only one of them should be selected for the following electronic structure calculation. Choosing appropriate structural features $\vec{q}$ in order to obtain reliable similarity values, however, is not straightforward. Furthermore, it should be noted that the norm in equation (3.1) is not necessarily the Euclidean distance, but can be any norm in the mathematical meaning[4]. The choice of the norm depends

---

[4] A norm $\|\cdot\|$ projects any feature vector $\vec{q}$ from the configuration space $\mathcal{C}$ on the set of non-negative real numbers $\mathbb{R}_0^+$, while fulfilling three conditions:

1. Triangle inequality: $\forall \vec{p}, \vec{q} \in \mathcal{C}$: $\|\vec{p} + \vec{q}\| \leq \|\vec{p}\| + \|\vec{q}\|$
2. Absolute homogeneity: $\forall \alpha \in \mathbb{R}$: $\|\alpha\vec{q}\| = |\alpha| \cdot \|\vec{q}\|$

on the selected features representing the structure and can influence how well structures can be distinguished.

In computational materials science, atomic structures are usually described by a list of atomic positions and their corresponding elements. This makes it easy to visualise the atomic structure and set up the potential energy of an electronic structure or classical molecular dynamics calculation. For the purpose of comparing two structures, however, the list of positions is not a very convenient representation, since it does not include the knowledge about basic invariants of atomic structures. Most evidently, the list of positions is not permutation invariant, because swapping two entries yields a different representation, even though nothing in the structure changes when both entries have the same chemical species. Furthermore, the list of positions is not invariant to translations and rotations, which means that moving the whole structure without changing the relative positions of the atoms yields a different representation, even though the properties of the displaced or rotated structure will remain the same. It is possible to overcome these drawbacks of the atomic positions representation by defining an appropriate norm to calculate the distances between two structures [80]. However, the adapted norm needs significantly more time to be computed, which is why for large sets of structures changing to a different representation is more efficient.

In the past two decades, the field of machine learning for atomic structure calculations and materials science has advanced significantly [81], resulting in several new ways of representing atomic structures. Supervised machine learning applications predict atomic or molecular properties of new compounds from big datasets of known compounds. In order to achieve high predictive accuracy, they depend on having a reliable and efficient measure for the similarity of two atomic structures. Therefore, the representations and features employed in machine learning are also perfectly suited for calculating similarity measures in `CodeRed`.

One very successful representation for machine learning is called smooth overlap of atomic positions (SOAP). Originally, it was designed to compare the chemical environments of atoms [82], but it can also be easily extended to compare whole atomic structures [83]. For the calculation of the SOAP features of one atom in the structure, the environment of the atom is represented as a distribution $\rho(\vec{r})$, which is a sum of Gaussian distributions centred at the positions of each atom in the environment. The similarity of two environments follows from the overlap integral of the two distributions. In order to obtain rotational invariance, however, the overlap integral has to be integrated over all possible relative rotations between the two environments. Translational invariance is already ensured, since all positions are expressed with respect to the atom of interest. Furthermore, permutational invariance can be achieved easily by creating separated distributions for each species in the structure. The overlap integral and the integral over all rotations are simplified significantly by expanding the distribution of environmental atoms in terms of spherical

---

3. Positive definite: $\|\vec{q}\| = 0 \implies \vec{q} = \vec{0}$

harmonics $Y_{lm}(\vec{r})$ and an orthogonal set of radial basis functions $g_n(\vec{r})$:

$$\rho(\vec{r}) = \sum_{nlm} c_{nlm} g_n(\vec{r}) Y_{lm}(\vec{r}) \quad \text{with} \quad c_{nlm} \in \mathbb{C} \tag{3.2}$$

The elegance of SOAP – and probably also one of the reasons for its good performance – lies in this natural choice of a basis set that is known from the atomic orbitals of the hydrogen atom. The final SOAP features are coefficients derived from the expansion coefficients c_{nlm} and known as the power spectrum $p_{nn'l}$:

$$p_{nn'l} = \sum_{m=-l}^{m=l} c_{nlm} (c_{n'lm})^* \tag{3.3}$$

Using this representation, the overlap and rotation integral for calculating the similarity of two environments is simply the dot product of the two SOAP vectors. The transformation from the single atomic environments of each atom in the structure to an overall structural descriptor and an accompanying norm, is achieved by appropriate averaging [83].

The number of SOAP features depends on how many terms are used in the expansion (3.2). Usually, a SOAP vector contains a few thousand entries, but dimensionality reduction algorithms, such as Principal Component Analysis (PCA) or Principal Covariates Regression (PCovR) can give valuable insight into the structure of the dataset and structure-property relationships [84]. Even though there is still room for further theoretical development of the SOAP representation [85], it has been applied very successfully for the creation of machine learned interatomic potentials that can predict the stable structures of molecular crystals [86], as well as the formation enthalpies and elastic constants of several metals [87].

A subroutine for the calculation of SOAP features is included in `CodeRed`. However, by allowing the user to define any function that converts atomic positions to a desired feature vector and use any function to calculate the distances between those feature vectors, `CodeRed` is not limited to the SOAP representation. Therefore, the extension to other representations and similarity metrics, including SPRINTs [88], Coulomb Matrices [89], and Atom-Centred Symmetry Functions (ACSFs) [90] is straightforward.

Finally, an algorithm needs to decide which structures should be selected to sample the configuration space based on the similarity metric. Again, tools from machine learning are perfectly suited for this task. Since there is no further information on whether a selection is good or not, it is necessary to employ unsupervised machine learning algorithms. For example, a clustering algorithm can bundle similar structures in clusters, and then only select one structure from each cluster that represents the whole cluster. Several well-known clustering algorithms are available for this task, such as k-means clustering, agglomerative clustering or DBSCAN. An example of k-means clustering is shown in Figure 3.6a. At first, it randomly creates a fixed number of cluster centres, and then assigns each point to the closest centre. Then, the new cluster centres are calculated from the means of all points in each cluster.

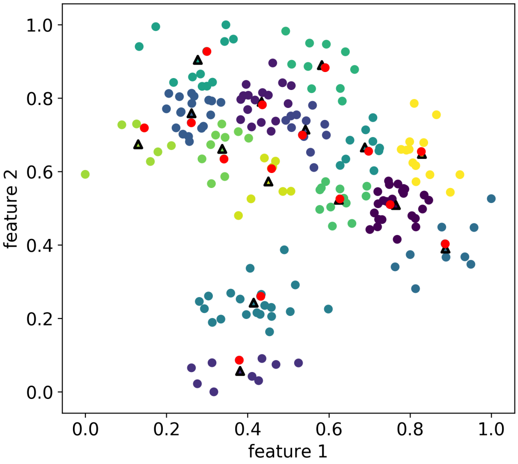

(a) selection by k-means-clustering

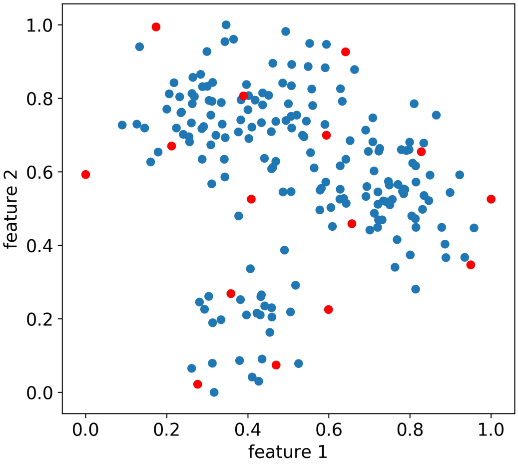

(b) selection by furthest point sampling

Figure 3.6: Illustration of the k-means-clustering (a) and furthest-point-sampling (b) selection algorithms applied to a randomly created configuration space of 200 configurations described by two features. Each configuration is represented by a circle marker, and the 15 selected configurations are marked in red. For the k-means-clustering, the colour indicates the corresponding cluster, and black triangles mark the cluster centres.

The process of assigning the points and re-calculating the cluster centres is repeated until the clusters stop changing.

An alternative to clustering algorithms is the selection by Furthest Point Sampling (FPS). The idea behind FPS is to select a set of structures with the highest possible distance to each other, meaning that the similarity of the two most similar structures in the selection is minimised (see Figure 3.6b). Even though there is an exact solution to the FPS problem, the number of possible selections usually requires an approximative solution. Comparing the resulting selections in Figure 3.6 shows the different characteristics of both algorithms. While the clustering algorithm can sample dense areas with more points, the FPS algorithm yields a more uniform sampling. Therefore, the structures selected by the clustering algorithm are better suited for representing their area of the configuration space, while the FPS algorithm performs better at including outliers (compare, for example, the sampling of points with feature 2 smaller than 0.4 at the bottom centre of Figures 3.6a and 3.6b). Both the clustering and the FPS algorithms have the advantage, that the number of selected structures can be selected by the user, which allows to limit the computational costs of further analysis. However, this advantage also bears the risk of missing important structures, if the number of selected structures is too low. Therefore, different selection sizes and their influence on the resulting structures should be carefully analysed.

Openness, dependences and usability

One of the aforementioned goals is to make `CodeRed` an open source software that only depends on other open source packages. This goal is achieved by using *python* as a programming language and including other existing, and openly available python packages for certain tasks in `CodeRed`. Furthermore, python is a common scripting language in the scientific community, which makes `CodeRed` easier to learn for many potential users. The source code of `CodeRed` is published on the GitLab repository hosted by TUHH under the GNU Lesser General Public License[5]. Therefore, it can be easily implemented in other software, further developed by the community, and distributed by companies with their own add-ons.

Like many other scientific codes, the core elements of `CodeRed` depend on the `numpy` package [91] for the handling of data arrays[6]. Furthermore, atomic structures are implemented through `Atoms` objects from the atomic simulation environment (`ase`) package [92], which also provides methods to write these structures to input files for electronic structure codes[7]. The implemented conversion of structures to SOAP descriptors uses the python implementation

---

[5] Visit `https://collaborating.tuhh.de/m-9/commod/codered` for obtaining the code and `http://www.gnu.org/licenses/` for detailed information about the license.

[6] Visit `https://numpy.org/` for further information.

[7] Visit `https://wiki.fysik.dtu.dk/ase/` for further information on `ase`.

of the `librascal` [93] library[8], developed by the COSMO and LAMMM labs at the École polytechnique fédérale de Lausanne (EPFL). Machine learning tools are implemented through the `scikit-learn` package[9], which has become a standard software for machine learning applications in the last decade [94].

Regarding the usability, `CodeRed` is much more interactive than its predecessors. As a python package, it can be loaded into Jupyter[10] notebooks, where it is easy to go back to intermediate steps and change input parameters without the need to re-run the whole script. This also simplifies learning `CodeRed` through existing working examples. Furthermore, the object oriented structure of `CodeRed` makes it possible to operate `CodeRed` interactively in a python shell. For example, after an unsatisfactory call of `code()`, the user can change the properties of one of the included `AdAtom` objects and then call `code()` again to see how the changes affect the resulting structures. Moreover, the separation of the configuration space determination (`code()` method) and the configuration space reduction (`red()` method) makes it easy to compare and study the influence of different selection criteria on the resulting configuration space sampling.

Concluding remarks

In this chapter, a new tool for Configuration space determination and Reduction (`CodeRed`) was introduced. The aim of the new tool is to aid the thorough search for the most stable adsorption structures, which is particularly difficult due to the high dimensional space to search. Reviewing the most important existing solutions, it became clear that for flexible small and medium sized adsorbates, a new solution might be more efficient. In order to close this gap, `CodeRed` was created.

With the new software, arbitrary adsorption structures can be built, only limited by the hardware of the machine it is running on. Based on very basic chemical intuition and prior knowledge about the system, a large number of sensible adsorption configurations is created representing the full configuration space. Rigid parts of the molecule that are expected to not change their configuration upon adsorption, can be excluded from the configuration space sampling and be re-added later in the process. Since similar structures usually relax to the same local minimum, a further reduction of the number of structures based on their similarity can save a considerable amount of computational resources. `CodeRed` employs modern machine-learning tools to calculate the similarities between the structures created, and select the

---

[8] Visit `https://cosmo-epfl.github.io/librascal/` for guidance on installation and usage of `librascal` for the creation of SOAP vectors and other descriptors.

[9] Visit `https://scikit-learn.org/stable/` for the `scikit-learn` documentation.

[10] Visit `https://jupyter.org/` for more information on the Jupyter project.

most dissimilar ones for further analysis. Moreover, it allows to include user-defined functions for this task, which makes it open to future developments in this emerging field. In summary, `CodeRed` combines chemical intuition with unbiased structure search and machine learning techniques, for an efficient and thorough sampling of the configuration space.

As an open-source python package, `CodeRed` uses a widely-known software framework, which makes it easy for other people to integrate the tool in their workflows, combine it with other software, and contribute to its improvement. For example, a user-defined function for representation and selection of structures could be included permanently in `CodeRed`, so that it can be invoked by simple keywords. Furthermore, it might be possible to speed-up parts of the software through parallelisation, i.e. the distribution of independent tasks on different computing units. In the future, one may also reconsider the storage of all possible configurations in the memory of the machine, which limits the number of configurations to analyse. Storing the configurations on the hard drive or in a more memory efficient way can extend the applicability of `CodeRed`, but will also most likely slow down the software. Finally, `CodeRed` has only been applied to a few example systems so far. Applying it in more and more adsorption structure searches will not only reveal further points for improvement, but also show the true power of the tool, by finding adsorption structures that pure chemical intuition would have missed.

4

Restructuring of magnetite/carboxylic-acid interfaces

The hybrid interface between carboxylic acids (R−COOH) as an organic component and magnetite (Fe_3O_4) nanoparticles, plays an important role in many applications. In drug delivery applications, the chemicals to deliver are bound to the magnetite particle through carboxylic acids [2]. If the interface fails, the drug could be released earlier or in a different part of the body than intended. The same applies to the application of magnetite for the cleaning of waste water from pollutants, such as heavy metal ions, which are captured by molecules that bind to magnetite through a carboxylic acid anchoring group [1, 95]. Investigating the adsorption of smaller carboxylic acids on magnetite surfaces can also help to understand how magnetite works as a catalyst in important industrial processes, such as the water-gas shift reaction [3, 4] or Fischer-Tropsch synthesis [4, 96]. Last but not least, the extremely high interface to volume ratio in hybrid materials based on a combination of magnetite nanoparticles and carboxylic acids, makes the binding strength of the interface a crucial property for the overall mechanical strength of the material.

In this chapter, the basic properties and common approaches for the modelling of magnetite are introduced first. Then, the atomic structures of the most important facets of magnetite nanoparticles are presented. They form the basis of the following theoretical adsorption studies for formic acid on magnetite surfaces. As the smallest representative of the carboxylic acid family, formic acid is used to study how the structures of the relevant interfaces are affected by the adsorption process, and to determine the binding energies of different interfaces. The results presented in this chapter are published in [97] and [98].

4.1 Properties of bulk magnetite

Magnetite (Fe_3O_4) takes a special place among the different possible oxidation products of iron, since the iron atoms in magnetite come in two different oxidation states, Fe^{2+} and Fe^{3+}. The less oxidised wüstite (FeO) has exclusively Fe^{2+} ions, and the more oxidised maghemite (γ-Fe_2O_3) and hematite (α-Fe_2O_3) phases are composed of Fe^{3+} and O^{2-}. The mix of oxidation states in magnetite gives rise to interesting properties, such as its name-giving magnetism, and a drastic change of its electrical conductivity at the Verwey temperature around 120 K [99]. Most metal oxides are ceramics, but the electrical conductivity of magnetite at room temperature forbids the classification of magnetite as a ceramic material following most definitions. However, it is not a classic metal either. According to band structure calculations [100], bulk magnetite is metallic only in the minority spin component, while the majority spin orientation is semiconducting with a band gap of approximately 1.5 eV. This combination makes magnetite a half-metal and sparked the idea of using it in spintronic applications. However, the half-metallicity of magnetite above the Verwey temperature is still under debate, since the expected spin-selectivity of $-100\,\%$ at the Fermi edge (with the minus sign as a reference to the minority spin component) is not observed experimentally [101]. More recent computational studies also suggest that magnetite is a semiconductor at room temperature with a small band-gap induced by symmetry breaking [102].

Around 120 K magnetite passes through the Verwey transition [99]. Below this temperature, the conductivity and magnetisation of magnetite drop significantly, and the structure is distorted slightly, resulting in a low symmetry monoclinic crystal structure [103]. Verwey connected both to a change in the charge ordering, but the origin and mechanism of the Verwey transition are far more complex [103] and still a matter of research [104]. However, since the motivation of this work stems from applications at temperatures much larger than 120 K, the Verwey transition is not studied or discussed in greater detail here, and only the room temperature structure of magnetite is considered in the following.

Above the Verwey temperature, magnetite crystallises in a cubic inverse spinel structure (see Figure 4.1). In this structure, the oxygen ions form a face-centred cubic lattice, while the iron ions occupy one eighth of the tetrahedral and half of the octahedral gaps in the lattice [105]. The tetrahedral gaps are filled with Fe^{3+} exclusively, while there is a mix of Fe^{2+} and Fe^{3+} on the octahedral sites, resulting in the sum formula $Fe^{2+}Fe_2^{3+}O_4^{2-}$. Therefore, electrons can move from one octahedral iron to the next, causing the observed electrical conductivity at room temperature [100]. In fact, due to the electron mobility and the resulting charge fluctuation, an effective oxidation state of $Fe^{2.5+}$ is commonly assumed for the octahedral iron sites. It has to be noted, that the formal integer charges used for explaining the chemistry of magnetite, are not observed in electronic structure calculations. The difference between calculated local charges on the octahedral (formally 2.5+) and tetrahedral (formally 3+) iron atoms is only around $0.1\,e$ for most exchange-correlation functionals. The charge distribution between iron and oxygen atoms also

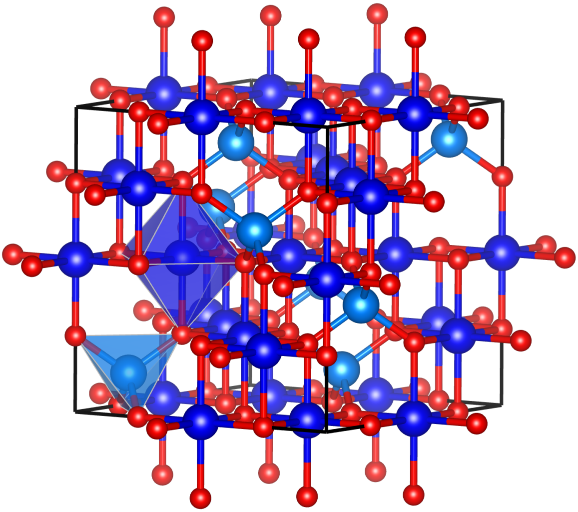

Figure 4.1: Bulk structure of magnetite (Fe_3O_4) optimised with DFT. The inverse spinel cubic structure is made up of a face-centered cubic lattice of oxygen atoms (red) and iron atoms occupying the octahedral (dark blue) and tetrahedral (light blue) gaps in that lattice.

appears to be more spread out, leading to charges around $-1.2\,e$, $1.5\,e$, and $1.6\,e$ on oxygen atoms, octahedral iron atoms, and tetrahedral iron atoms, respectively (see Table C.3 in Appendix C). Even though these charges are far away from the formal charges, the description with formal charges is often used, because it is more convenient and the qualitative trends are the same.

The magnetic moments of tetrahedral and octahedral sites are coupled anti-ferromagnetically. Therefore, the magnetic moments of the Fe^{3+} ions on both sites cancel each other out, resulting in a magnetic moment of $4\,\mu_B$ per formula unit stemming mostly from Fe^{2+} [106]. It follows that magnetite is ferrimagnetic. A more detailed comparison of the magnetic moments of bulk magnetite calculated with different exchange-correlation functionals is shown in Appendix C, Table C.2. On a larger scale, the ferrimagnetism of the magnetite crystals results in a super-paramagnetism of magnetite nanoparticle assemblies [20], which can be used to steer them in drug delivery applications or to assist a self-assembly process.

Accurate modelling of Fe_3O_4 with density-functional theory (DFT) is challenging, due to the localisation of the d-band electrons at the iron atoms. One way to circumvent this problem is to add additional constraints to DFT calculations [100]. A very common constraint for transition metals is the use of a Hubbard model [35], where an additional parameter U scales how much the d-electrons are localised. For magnetite, U-values between 3 eV and 4 eV reproduce the structure, energetics, band gap, and magnetic moments with sufficient accuracy [107]. It has to be noted, though, that the quality of predictions for different properties are not the same for different values of U, and sometimes more advanced methods are needed to obtain very accurate results [102, 108], especially when it comes to calculating the electronic band structure. In this work, $U = 4.0\,\text{eV}$ is used in combination with the GGA exchange-correlation functional by Perdew, Burke, and Ernzerhof (PBE) [30], if not otherwise stated. This results in a lattice constant of 8.480 Å, which is slightly larger than the experimentally measured lattice constant of 8.396 Å [109]. Other quantities, such as the band gap, magnetic moments, and the formation enthalpy also agree well with experimental results [110]. The computational settings for the results obtained in this chapter are listed in detail in Appendix A, followed by the necessary convergence tests in Appendix B, and comparison between results obtained with different exchange correlation functionals in Appendix C.

4.2 The major facets of magnetite nanoparticles

Magnetite nanoparticles can be synthesised in various shapes ranging from cubes to octahedrons, spheres, and even star-like spiky shapes [111]. While the latter are clearly non-equilibrium structures, cubes and octahedrons can be formed in thermodynamic equilibrium capped with {001} and {111} facets, respectively, which are known to have the lowest surface energies [112]. Almost spherical particles are created when {001} and {111} facets are very close in energy. Therefore, these two facets are the most important when it comes to understanding magnetite nanoparticles and their interaction with carboxylic acids.

The magnetite (001) surface

Along the [001] direction, magnetite is made up of alternating layers of tetrahedrally coordinated iron (Fe_{tet}, A-layer), and octahedrally coordinated iron (Fe_{oct}) and oxygen (B-layer). Therefore, in principle two different terminations are possible for a bulk truncated (BT) surface. However, theoretical and experimental studies found that only the B-layer $Fe_{oct}-O$ termination is stable in typical conditions [113, 114]. The resulting surface structure is shown in Figure 4.2a. Apart from the termination, experiments observe an undulation of the Fe_{oct} rows on the surface, leading to a larger $(\sqrt{2}\times\sqrt{2})R45^\circ$ unit cell [115, 116]. At first, these were explained by small relaxations of the iron atoms in a model called distorted bulk truncation (DBT) [117]. Later, a subsurface cation vacancy (SCV) reconstruction model was found, which explains the experimental data much better than the DBT model, and is also calculated to be more stable in typical conditions [118]. In the SCV model, two Fe_{oct} vacancies are created in the subsurface layer and one tetrahedrally coordinated interstitial iron (Fe_{int}) is created in the layer above (see Figure 4.2b).

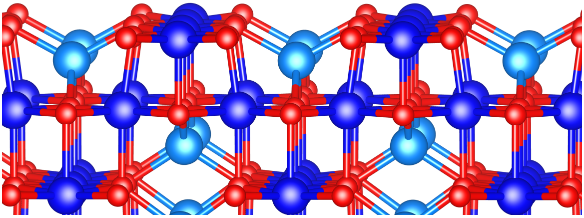

(a) BT structure

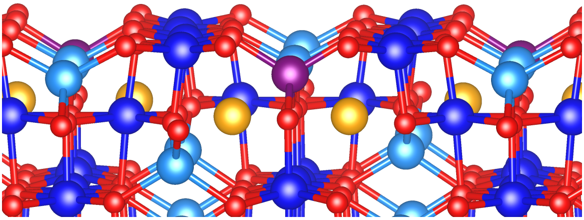

(b) SCV structure

Figure 4.2: Atomic structure of the clean (001) surface of Fe_3O_4 after structural optimisation with DFT. The bulk truncated (BT) model (a) is found to be less stable than the subsurface cation vacancy (SCV) model (b). Colour code: Fe_{oct} – dark blue, Fe_{tet} – light blue, Fe_{int} – violet, Fe vacancy – orange, O – red.

Therefore, the SCV model is iron deficient compared to the bulk truncation, which means that it is stabilised by oxidising conditions.

The calculated structure of the SCV reconstruction is shown in Figure 4.2b and exhibits the same pronounced undulation of the octahedral iron rows on the surface. Furthermore, the calculation unveils that this undulation continues in the underlying oxygen rows, because of the missing Fe – O bonds caused by the iron vacancies. The next Fe_{oct} – O-layer still shows some significant relaxation of the oxygen atoms for the same reason, before the structure becomes bulk-like in the deeper layers with relaxations smaller than 0.1 Å. The bulk truncated structure (Figure 4.2a) reaches this threshold much closer to the surface, as only the first three layers relax significantly. On both surfaces, the charges of the octahedrally coordinated iron atoms close to the surface increase. This can be interpreted as Fe^{2+} oxidising to Fe^{3+}, which increases the magnetic moments of these atoms on the surface. The total magnetic moment of the SCV structure, however, is much lower, since two octahedral irons are replaced with an anti-ferromagnetically coupling interstitial tetrahedral iron [118].

Adsorption sites on the magnetite (001) surface are the under-coordinated

Fe_{oct} and oxygen atoms in the outermost layer. One major influence factor is the Coulomb interaction with the positively charged Fe_{oct} and negatively charged O sites, which can lower the barrier for the splitting of molecules on the surface and lead to selective adsorption at distinctive sites. Combined with the presence of electrical conductivity, it makes magnetite an interesting catalyst in, for example, the water-gas shift reaction or Fischer-Tropsch syntheses. In this regard, the adsorption and splitting of water [119] and methanol [120] were already investigated before, as was the interaction with other molecules, such as benzene (C_6H_6) [121], carbon dioxide (CO_2) [122], carbon monoxide (CO) [123] or nitric oxide (NO) [124].

The magnetite (111) surface

The question of the termination of the magnetite (111) surface is less easy to answer than for the (001) surface. Cutting the crystal perpendicular to the [111] direction gives six different possible terminations: tet1, O1, oct1, O2, tet2, and oct2 (see Figure 4.3). All of these terminations only have one species (Fe_{tet}, Fe_{oct}, or O) on the surface and are named accordingly, but usually the loose packing of the iron terminations makes the oxygen layer below also accessible for adsorbates. Electronic structure calculations predicted that only the three terminations shown in Figure 4.3 (oct2, tet1, and O1) can be stable in a reasonable range of oxygen pressures and temperatures [125, 126]. The latest experiments support this view, finding a tet1 terminated Fe_3O_4 (111) surface in ultra-high vacuum [98, 127]. Therefore, only the oct2, tet1, and O1 terminations are studied further in this work.

The oct2 termination is characterised by two iron atoms per unit cell on the surface. One of them is placed in an Fe_{oct} position, but is only threefold coordinated by oxygen. The other one sits on an Fe_{tet} position and also has only three neighbouring oxygen atoms. On top of this under-coordination

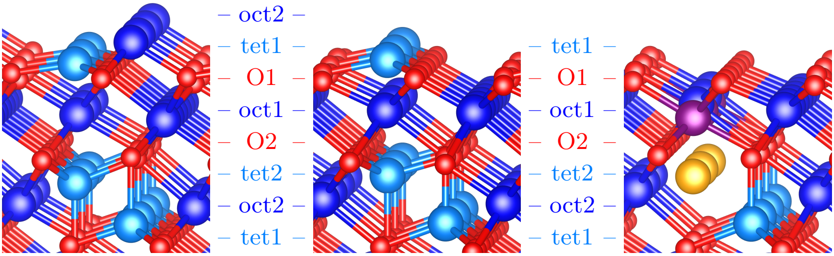

Figure 4.3: Atomic structures of the different terminations of Fe_3O_4 (111) after structural optimisation with DFT: (from left to right) oct2, tet1, and O1. The labelling of the different layers in [111] direction is also indicated. Colour code: Fe_{oct} – dark blue, Fe_{tet} – light blue, Fe_{int} – violet, Fe vacancy – orange, O – red.

of iron atoms, the underlying oxygen layer also has one under-coordinated oxygen atom per unit cell, which binds to the next tet2-layer in the bulk, and therefore, relaxes inward for this termination. The oct2 termination of the magnetite (111) surface is only stable at very reducing conditions, since it is oxygen deficient compared to bulk magnetite. Just taking away the oct2 layer, and thereby creating the tet1 termination, already changes the stoichiometry to an iron deficient surface. Therefore, the tet1 termination is also stable in more oxidising environments. Its one $\mathrm{Fe_{tet}}$ atom on the surface is one-fold under-coordinated, as for the oct2 termination, and the now missing $\mathrm{Fe_{oct}}$ also makes the three underlying oxygen atoms one-fold under-coordinated. Since now all the oxygen atoms in the O1-layer are one-fold under-coordinated, there is a more uniform inward relaxation of the oxygen atoms, as can be seen in Figure 4.3. The tet1 terminated surface is considered to be the most stable surface termination of magnetite (111), because usual surface science experiments operate in ultra-high or high vacuum, where the tet1 termination is most stable [126, 127]. However, in oxidising conditions relevant for real world applications, the O1 termination may become more stable, as will be shown in Section 4.4.

The O1 termination has a dense layer of oxygen atoms on the surface. There are no iron atoms in the surface layer and all iron atoms in the subsurface layers are fully coordinated by oxygen octahedra or tetrahedra. In the calculations performed in this work, one tetrahedrally coordinated iron atom moved from the tet2-layer to the oct1-layer during the structural optimisation, leaving behind an iron vacancy in the tet2-layer (see Figure 4.3). Even though the interstitial iron atom is now octahedrally coordinated by oxygen, it still couples anti-ferromagnetically with the other regular $\mathrm{Fe_{oct}}$ atoms. This reconstruction of the O1 termination seems to be more stable than the simple bulk truncated surface. However, this may be an artefact from the overestimation of the lattice constant by the PBE+U exchange correlation functional. Calculating the surface energies with the slightly smaller experimental lattice constant instead, yields the regular bulk truncated structure and higher surface energies for the reconstruction. Other calculations with a smaller U-value also do not seem to observe the reconstruction [125]. Since the O1 termination only forms at very oxidising conditions, it is harder to analyse experimentally with atomic resolution, and so far there is no experimental data on its structure to validate the results from theory. Thus, the question of the exact structure of the O1 termination remains open for now. Even though the movement of iron to the surface may be an artefact from the calculation, it already indicates a high mobility of iron in magnetite surfaces. This allows magnetite to restructure its surfaces upon adsorption, which is the topic of the next sections and this chapter in general.

4.3 Formic acid on magnetite (001)

Formic acid (HCOOH) is the shortest possible carboxylic acid, and an intermediate in the catalytic processes mentioned in the introduction to this chapter. Furthermore, it can be seen as a representative of the whole group of carboxylic acids, with respect to adsorption configurations and binding strength. The adsorption of formic acid on magnetite (001) was studied experimentally by Gamba et al.[128], showing that formic acid dissociates into formate ($HCOO^-$) and a proton (H^+) on the surface. The adsorption also changes the diffraction pattern in low-energy electron diffraction (LEED), indicating a surface transformation. However, the preferred adsorption site could not be determined and the diffraction pattern did not allow for a unique identification of the underlying surface structure. Hence, these factors are studied computationally here, in order to gain more insight into the processes on the surface upon carboxylic acid adsorption.

Adsorption sites and energies

The possible adsorption sites of formate on the bulk truncated (BT) and reconstructed (SCV) structures of the magnetite (001) surface are shown in Figure 4.4. Two sites can be distinguished independent of the underlying surface structure: The *int*-site, where formate adsorbs on the two octahedrally coordinated iron atoms next to an interstitial unoccupied $\mathrm{Fe_{tet}}$ site (see Figure 4.4a,b); and the *tet*-site, where formate adsorbs on the two octahedrally coordinated iron atoms next to a regular occupied $\mathrm{Fe_{tet}}$ site (see Figure 4.4c,d). Apart from the underlying surface, there are no major differences in the calculated adsorption structures visible when comparing the BT and SCV surfaces, but the adsorption energies differ significantly. On the bulk truncated surface, formic acid adsorbs with an energy gain of approximately 2.1 eV, while on the reconstructed surface the energy gain is almost 1 eV lower (see Table 4.1). The influence of the adsorption site of the formate on the adsorption energy is relatively low. At full coverage, the tet-site is preferred on both the BT and the SCV surfaces by 40 meV. At the half-covered surface, however, the int-site is slightly more favourable on the SCV surface ($\Delta E_{\mathrm{ad}} \approx 40\,\mathrm{meV}$), while the BT surface favours adsorption on the tet-site even more ($\Delta E_{\mathrm{ad}} \approx 170\,\mathrm{meV}$).

A more pronounced influence on the adsorption energies is observed for the positioning of the dissociated hydrogen atom. On oxides, hydrogen usually binds to the oxygen atoms on the surface. Therefore, there are two different sites present on the (001) surface: oxygen that is bound to a near-by tetrahedral iron (regular $\mathrm{Fe_{tet}}$ or interstitial $\mathrm{Fe_{int}}$), and oxygen that is not. This results in several different possible distributions of the two dissociated hydrogen atoms per unit cell at full coverage formic acid adsorption, as illustrated in Figure 4.5. However, from the adsorption energies presented in Table 4.1, it becomes obvious that hydrogen atoms preferably adsorb at oxygen atoms next to a gap, i.e. without a near-by tetrahedrally coordinated iron. The same site-preference was found before for the adsorption of pure hydrogen [129–132], hydrogen from dissociated water [119, 133], and single metal atoms [108, 118].

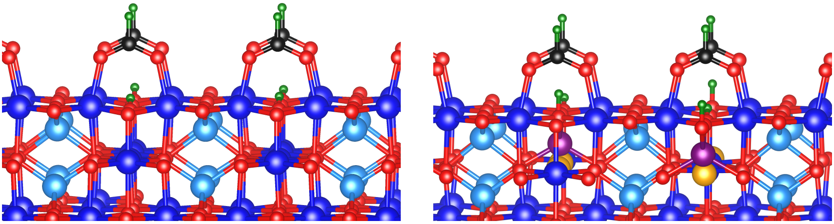

(a) formate at BT-int **(b)** formate at SCV-int

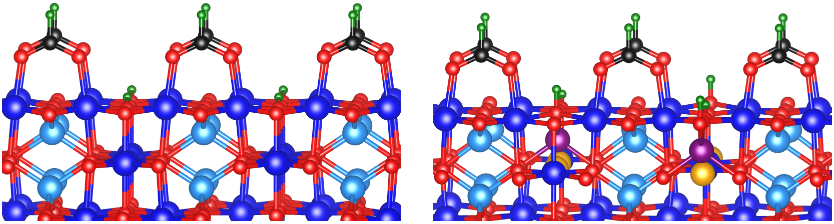

(c) formate at BT-tet **(d)** formate at SCV-tet

Figure 4.4: Adsorption structures of formic acid on Fe_3O_4 (001) with different adsorption sites for the formate ($HCOO^-$), and bulk truncated (BT) or reconstructed (SCV) surface structures after structural optimisation with DFT. Colour code: Fe_{oct} – dark blue, Fe_{tet} – light blue, Fe_{int} – violet, Fe vacancy – orange, O – red, C – black, H – green.

Table 4.1: Calculated adsorption energies E_{ad} of formic acid on Fe_3O_4 (001) depending on the adsorption site (tet-site or int-site, see Figure 4.4), the bulk truncated (BT) or reconstructed (SCV) surface structure, and the positioning of the dissociated hydrogen (H_{diss}, see Figure 4.5).

Structure	E_{ad}(BT) / eV		E_{ad}(SCV) / eV	
	int-site	tet-site	int-site	tet-site
half-covered, H_{diss} at O_{int}	−2.22	−2.39	−1.31	−1.27
fully covered, H_{diss} at O_{int}	−2.08	−2.12	−1.15	−1.19
fully covered, H_{diss} at O_{tet}	−1.61	–	–	−0.96
fully covered, 2 H_{diss} at O_{int}	−1.96	–	–	−1.21

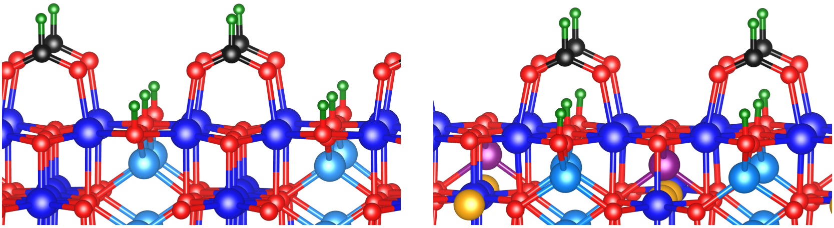

(a) H_{diss} at O_{tet} (BT surface) **(b)** H_{diss} at O_{tet} (SCV surface)

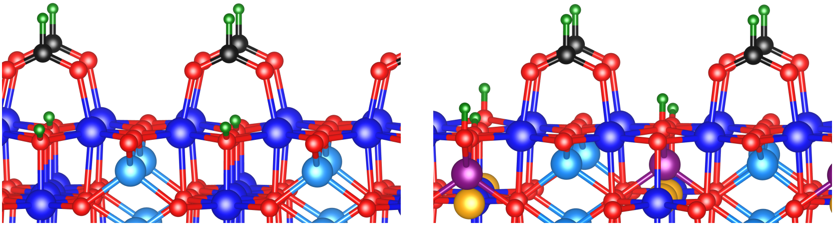

(c) H_{diss} at O_{int} (BT surface) **(d)** H_{diss} at O_{int} (SCV surface)

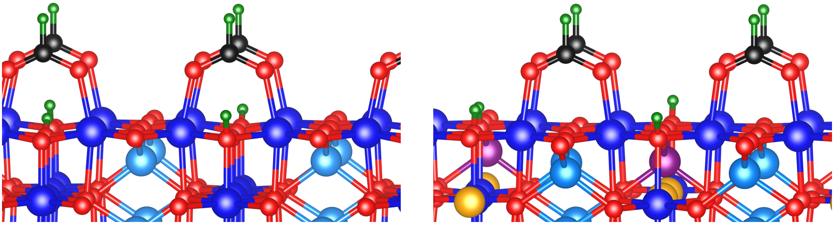

(e) $2\,H_{diss}$ at O_{int} (BT surface) **(f)** $2\,H_{diss}$ at O_{int} (SCV surface)

Figure 4.5: Adsorption structures of formic acid on Fe_3O_4 (001) with different adsorption sites (O_{tet} and O_{int}) for the dissociated hydrogen (H_{diss}) at the bulk truncated (BT) and reconstructed (SCV) surfaces after structural optimisation with DFT. Colour code: Fe_{oct} – dark blue, Fe_{tet} – light blue, Fe_{int} – violet, Fe vacancy – orange, O – red, C – black, H – green.

The effect is indeed so strong, that in spite of the repulsive Coulomb interactions between two adsorbed hydrogen atoms, it is more favourable to adsorb both dissociated hydrogen atoms at the same gap on the magnetite (001) SCV surface, than placing one of them next to the interstitial tetrahedral iron atom.

Lifting of the reconstruction

As previously mentioned, the diffraction pattern of the magnetite (001) surface changes from a $(\sqrt{2}\times\sqrt{2})$R45° pattern to a 1×1 pattern upon adsorption of formic acid [128], indicating a transition from the SCV to the BT structure. Only later on, this lifting of the reconstruction was unambiguously proven by a combination of surface x-ray diffraction (SXRD) and the work presented in this thesis [97]. To enhance the understanding of the reconstruction lifting process, two transition structures are studied here. Starting from the SCV surface covered with formic acid, one of the octahedral iron vacancies is filled by the interstitial tetrahedral iron in the first transition structure (see Figure 4.6b). Then, the other octahedral iron vacancy is filled by an octahedral

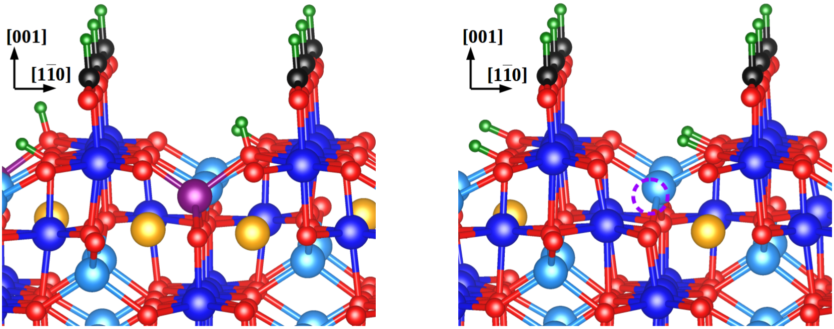

(a) reconstructed surface **(b)** first transition step

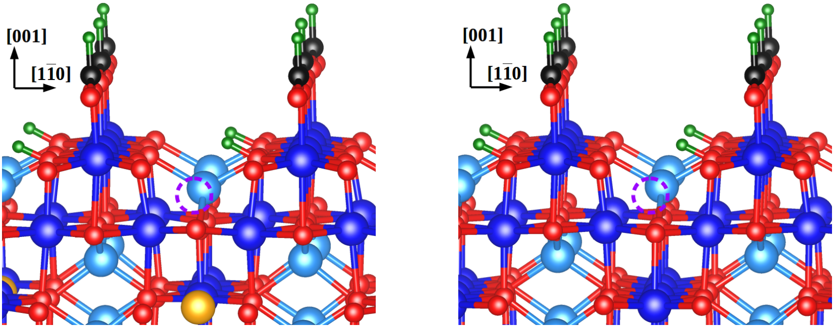

(c) second transition step **(d)** bulk truncated surface

Figure 4.6: Atomic structures during the reconstruction lifting process after structural optimisation with DFT. Colour code: $\mathrm{Fe_{oct}}$ – dark blue, $\mathrm{Fe_{tet}}$ – light blue, $\mathrm{Fe_{int}}$ – violet, Fe vacancy – orange, O – red, C – black, H – green.

iron from the more bulk-like layer below in the second transition structure (see Figure 4.6c). Finally, the BT adsorption structure can be formed by filling the remaining vacancy with an octahedrally coordinated iron atom. Interestingly, there is an energy gain of 47 meV per unit cell for going from SCV to the first transition structure and 83 meV per unit cell for the second transition step. It follows, that the basically unreconstructed (001) surface with an octahedral iron vacancy in the bulk-layer shown in Figure 4.6c is more favourable than the reconstructed SCV surface. However, it should be mentioned, that the energy barriers associated with the restructuring of the surface were not studied here. In bulk magnetite, calculations suggest barriers of 50 meV and 700 meV for the first and second transition steps, respectively [134]. But, diffusion barriers can differ in the surface layers due to surface stresses and the presence of additional structural degrees of freedom. Still, it can be assumed that the first step happens almost instantaneously, while the second step is associated with a higher barrier that slows down the process.

More insight into the stability of different surface structures in various conditions can be gained from surface phase diagrams (more information on the calculation of these diagrams can be found in Chapter 2). The diagram pre-

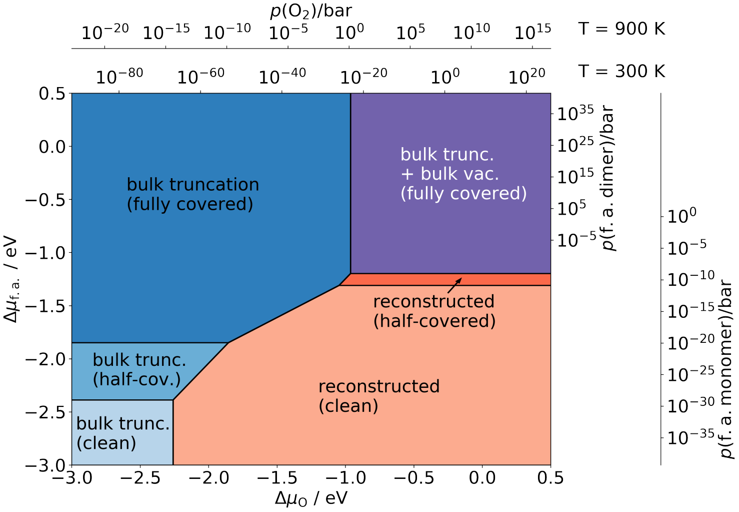

Figure 4.7: Calculated surface phase diagram of the magnetite (001) surface in contact with gaseous formic acid (f.a.) and oxygen (O_2). The structures with the lowest surface free energies are shown depending on the chemical potential shifts $\Delta\mu$, which are converted to pressure scales on the top and right. Formic acid gas undergoes a monomer-to-dimer transformation in the range of 10^{-3} bar to 10^{-2} bar [135] (see Appendix D for more information).

sented in Figure 4.7 shows the structures with the lowest surface free energy depending on the partial pressures of the surrounding oxygen and formic acid gases. The bulk truncated surface structure – represented by the blue region on the left – is clearly stabilised by formic acid adsorption, as the stability range with respect to the oxygen pressure increases when formic acid adsorbs on the surface. However, this is not enough to stabilise the pure bulk truncated surface at room temperature in ultra-high vacuum or at higher oxygen pressures. In more relevant conditions, the structure of the second transition step – represented by the violet region on the top right – is most stable. Therefore, the experimentally observed bulk truncation is stabilised by a combination of formic acid adsorption and the presence of bulk vacancies, which leads to the lifting of the SCV reconstruction, as discussed before.

These results can also be interpreted as a trend in which the magnetite surface is preferably in a more reduced state than the underlying layers. This is true locally for the SCV reconstruction of the clean surface and even more so for the described reconstruction lifting upon adsorption of formic acid. It is also observed in first computational studies on the surface structures of the closely related, more oxidised, maghemite (γ-Fe_2O_3) [136]. This may aid the understanding of oxidisation and catalytic processes on iron oxide surfaces in general, and be a driving force for iron diffusion in these materials, which is even observed at room temperature [137].

Insights from vibrational spectroscopy

In experiments, adsorption configurations of organic molecules are typically studied with Fourier-transformed infrared (FTIR) spectroscopy, where the unique vibrational frequencies of the molecule are recorded. However, the interpretation of FTIR spectra is not always straight forward, since the vibrational frequencies change depending on the underlying surface, and different configurations can have similar or overlapping peaks. Therefore, calculations based on density-functional perturbation theory (DFPT, see Chapter 2, Section 2.3) that compute the vibrational frequencies and intensities of each configuration can help to understand the experimental results and distinguish different structures.

The calculated vibrational spectra for different adsorption configurations are shown in Figure 4.8a. As can be seen at first glance, the spectrum of formic acid in the gas phase differs significantly from formic acid bound to the magnetite surface for wave numbers between $2000\,\mathrm{cm}^{-1}$ and $1000\,\mathrm{cm}^{-1}$. The stretching vibrations of the C=O double bond (σ(C=O) at $1760\,\mathrm{cm}^{-1}$) and the C−OH single bond ($1070\,\mathrm{cm}^{-1}$) disappear upon dissociation of the molecule. They are replaced by the asymmetric (σ_{as}) and symmetric (σ_s) stretching vibrations of the adsorbed O−C−O group around $1530\,\mathrm{cm}^{-1}$ and $1330\,\mathrm{cm}^{-1}$, respectively. The two modes differ mainly in the movement of the central carbon atom and the direction of the resulting dynamic dipole moment. In the asymmetric mode, one of the C−O bonds stretches while the other one contracts. Therefore, the positively charged carbon atom moves parallel to the surface in between the negatively charged oxygen atoms, leading to a dynamic

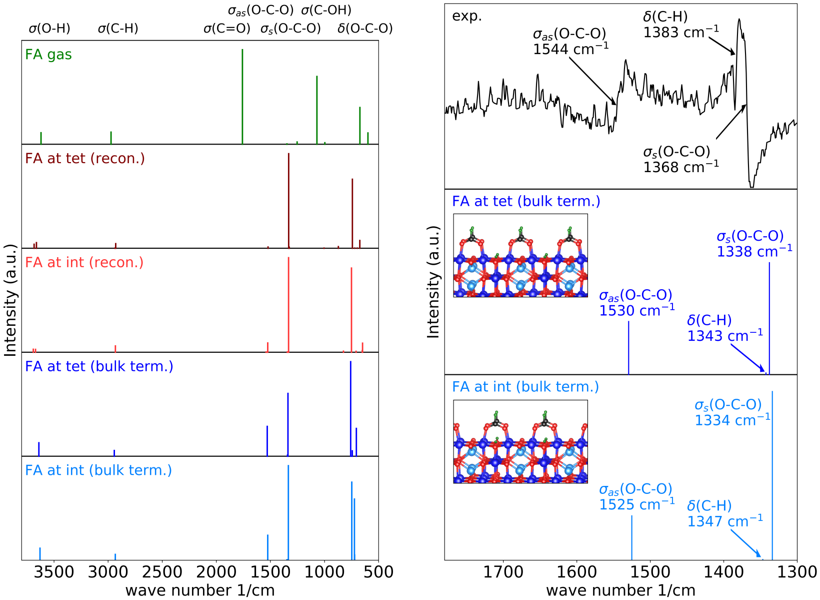

(a) (b)

Figure 4.8: Calculated vibrational spectra of formic acid in the gas phase and adsorbed on Fe_3O_4 (001): (a) comparison of the whole spectrum for different adsorption sites on the reconstructed and bulk truncated surface; (b) comparison of parts of the spectra for different adsorption sites on the bulk truncated surface with the experimental FTIR spectrum recorded by colleagues from DESY Nanolab (published in [97]).

dipole mainly oriented parallel to the surface. In the symmetric mode, both C−O bonds stretch and contract at the same time. Accordingly, the carbon atom moves perpendicular to the surface, creating a dynamic dipole moment in that direction. The characteristic frequencies of both vibrational modes do not change much depending on the underlying structure of the magnetite surface or the adsorption position, as can be seen in Figure 4.8. Nevertheless, the relative peak intensities show a noticeable dependence. The complete list of relevant calculated vibrational modes and intensities can be found in Appendix D, and animations of the vibrational patterns of some important modes can be viewed in the online supporting material[1].

---

[1] Visit `https://doi.org/10.15480/336.3408` for obtaining the online supporting material. The link can also be accessed by scanning the QR code at the beginning of Appendix D.

In materials with high electrical conductivity, like metals, a dipole moment parallel to the surface would create a mirroring dipole moment in the surface, thereby annihilating the overall dipole moment. This leads to selection rules, where only vibrational modes with a significant dipole moment perpendicular to the surface are visible in FTIR spectra, since the peak intensity is proportional to the square of the dynamical dipole moment. These rules can help to determine the orientation of molecules on the surface. However, since magnetite is neither a metal nor an insulator, the intensity of the asymmetric stretching vibration σ_{as} peak does not vanish, but is still significantly smaller than the intensity of the symmetric stretching vibration σ_s peak. Interestingly, the σ_{as} peak is much smaller on the reconstructed surface than on the bulk truncated surface, which could be used to track the reconstruction lifting process with FTIR spectroscopy. Examining the results for the different adsorption sites, *tet* and *int*, there is also a small difference in the peak intensity ratio between the asymmetric and the symmetric O–C–O stretching vibration. However, the comparison with experimental data presented in Figure 4.8b shows that these small differences may be harder to detect in practice.

Combining the presented results of different computational and experimental techniques, the complete story of the adsorption process of formic acid on magnetite (001) can be summarised as follows: As confirmed by FTIR spectroscopy, formic acid dissociates upon adsorption and forms a bi-dentate adsorption geometry. At first, formic acid adsorbs at the reconstructed surface with a lower binding energy and preferably at the *int*-site. But dosing more and more formic acid leads to a lifting of the reconstruction and preferred adsorption at the tet-site. This is confirmed by the ratio of the peak intensities in the FTIR spectrum, and more importantly, by surface x-ray diffraction (SXRD) measurements [97]. The latter also detects a 0.10/0.75 ratio for the occupancy of the *int*- and *tet*-sites, which can be explained by the change of the preferred adsorption site during the process and the low energy difference between both configurations. The dissociated hydrogen, which is close to impossible to detect by SXRD and FTIR spectroscopy, can be located at an under-coordinated oxygen atom with the help of the DFT calculations presented here.

4.4 Formic acid on magnetite (111)

In contrast to the (001) surface of magnetite, the adsorption mode of formic acid on magnetite (111) was not understood experimentally before. The only available study so far concluded a chelating adsorption of formate, based on scanning tunnelling microscopy (STM) images [138]. However, deducing an adsorption mode exclusively from STM images is not straightforward and unambiguous, especially when atomic resolution is not achieved, as was the case in the cited study. Therefore, a more thorough computational study is needed to uncover the most stable configurations and how they affect the stability of the different surface structures. The focus of this study lies on the tet1 termination, since it is the most stable termination in a wide range of oxygen chemical potentials. However, depending on the surface termination, different binding geometries with different adsorption energies are possible, which may lead to a stabilisation of other terminations, as observed for the (001) surface. Therefore, formic acid adsorption on the oct2 and O1 terminations of magnetite (111) is also discussed here, after presenting the thorough adsorption study for the tet1 termination.

Low coverage adsorption on the tet1 termination

The tet1 terminated Fe_3O_4 (111) surface has one under-coordinated iron atom per surface unit cell. Since the iron atoms are 6 Å apart, the very stable bi-dentate binding mode cannot be formed on this surface. The structure search algorithm described in Chapter 3 was used to generate 59 different adsorption geometries in order to sample possible configurations. However, during the structural optimisation, all of these geometries relaxed to structures with a quasi-bi-dentate (qbd) binding to the surface. Quasi-bi-dentate means that the hydrogen of the acid dissociates and binds to a surface oxygen, and the remaining formate binds to an iron atom and the newly created hydroxyl group (see Figure 4.9). While the Fe−O bond is a strong mixed covalent and ionic bond, the binding to the hydroxyl group happens through a weaker hydrogen bond. Similar binding geometries have also been observed on zinc oxide and titania surfaces before [139, 140]. Theoretical calculations predict that in quasi-bi-dentate binding geometries, the dissociated hydrogen may tunnel between or be shared by the two oxygen atoms involved [140].

The studies on formic acid adsorption at the magnetite (001) surface already showed a significant influence of the dissociated hydrogen atom (H_{diss}) on the adsorption energies (see Section 4.3). Therefore, the positioning of the hydrogen atom is studied in more detail here as well. In order to reduce the interaction with periodic images of the adsorbate, a larger surface cell with a lower coverage of one molecule per three iron atoms (1/3 monolayer) is used. Starting from a configuration where the hydrogen is placed at a nearest neighbouring (NN) oxygen atom, the quasi-bi-dentate binding distance is systematically increased by placing the hydrogen at the second (2NN), third (3NN), and fourth (4NN) nearest neighbouring oxygen atoms (see Figure 4.9 and Table 4.2). This significantly influences the adsorption energy, as well as the orientation of the remaining formate ($HCOO^-$) with respect to the Fe−O bonds at the surface. With hydrogen at the NN position, the formate orients parallel to the Fe−O bond, forming the qbd-$\upharpoonleft\upharpoonright$ adsorption mode. Placing the hydrogen further away at the 2NN position leads to a rotation of the formate by 60°, which equals an anti-parallel orientation with respect to one of the Fe−O bonds (qbd-$\upharpoonleft\downharpoonright$ mode). Because of the size and symmetry of the surface cell, the 3NN and 4NN positions are technically the same. However, due to the differences in the initial orientation of the formate, the adsorbate relaxes to distinct configurations with different $Fe_{tet}-H_{diss}$ distances. One of these configurations is quasi-bi-dentate (qbd-3NN), but the formate is not

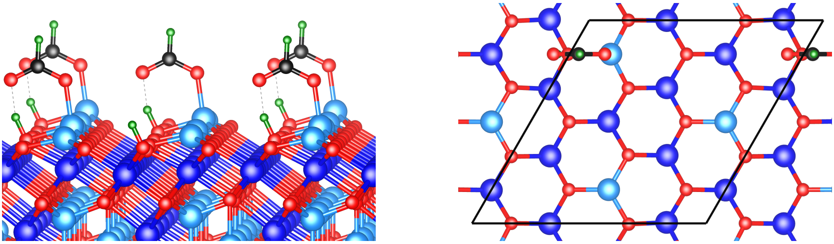

(a) qbd-↿↾ adsorption mode

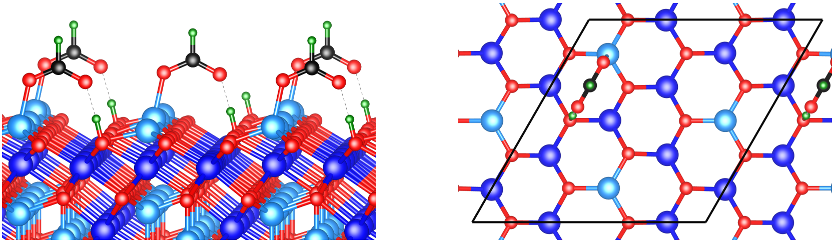

(b) qbd-↿⇂ adsorption mode

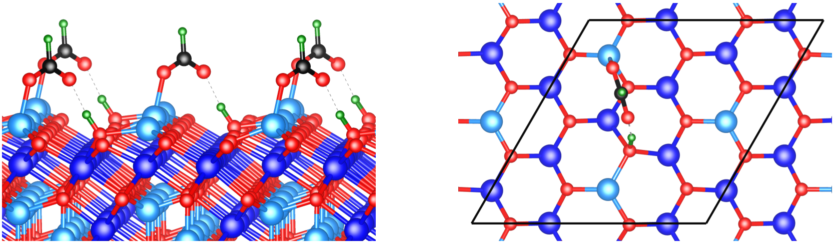

(c) qbd-3NN adsorption mode

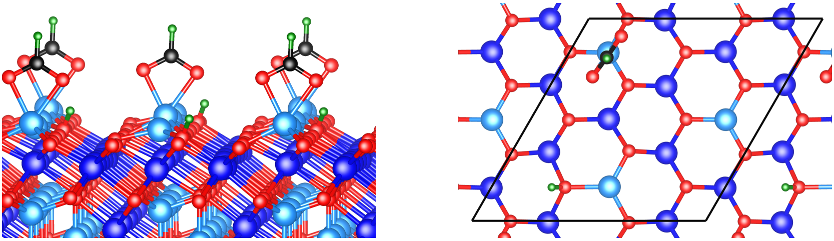

(d) chel adsorption mode

Figure 4.9: Adsorption geometries of formic acid on the tet1-termination of magnetite (111) at 1/3 monolayer coverage after structural optimisation with DFT. Different quasi-bi-dentate (qbd) and chelating (chel) adsorption modes are shown in a side view (left) and a top view (right). Colour code: $\mathrm{Fe_{oct}}$ – dark blue, $\mathrm{Fe_{tet}}$ – light blue, O – red, C – black, H – green.

Table 4.2: Adsorption properties of formic acid on magnetite (111) at low coverage (one molecule per $(\sqrt{3} \times \sqrt{3})\mathrm{R}30^\circ$ supercell) forming different configurations (qbd $\hat{=}$ quasi-bidentate, chel $\hat{=}$ chelating) with the dissociated hydrogen ($\mathrm{H_{diss}}$) bound to different surface oxygen atoms as shown in Figure 4.9.

	$\mathrm{H_{diss}}$ bound to			
	NN	2NN	3NN	4NN
binding mode	qbd-$\upharpoonleft\upharpoonright$	qbd-$\upharpoonleft\downharpoonright$	qbd-3NN	chel
$\mathrm{Fe_{tet}}-\mathrm{H_{diss}}$ distance / Å	2.38	3.16	3.78	4.03
adsorption energy / eV	−1.58	−1.82	−2.01	−1.83

oriented along one of the symmetry planes. The other is a bidentate-chelating (chel) adsorption mode, where both oxygen atoms of the formate bind to the same tetrahedral iron atom, while the hydrogen is bound to an oxygen atom further away from this adsorption site. The adsorption energies of all four different adsorption configurations are listed in Table 4.2. They show a clear preference for the quasi-bi-dentate qbd-3NN mode, with the chelating (chel) and quasi-bi-dentate qbd-$\upharpoonleft\downharpoonright$ adsorption configurations in second place having almost identical adsorption energies.

Stability at full coverage

At full coverage, the hydrogen on the third nearest neighbouring oxygen is closer to the next adsorption site than to the original one. Therefore, the formate on the next adsorption site is attracted to this hydrogen and a full-coverage chelating or qbd-3NN adsorption mode cannot be observed. Removing the dissociated hydrogen from the surface in the calculation results in a chelating binding to the surface (see Figure 4.10), but opens up the question of where the hydrogen might go to. Experimental analysis of scanning tunneling microscopy (STM) images and surface x-ray diffractometry (SXRD) results provide a possible answer to this question. They find that tetrahedral iron vacancies are present on real magnetite (111) surfaces with a concentration of roughly 20 % [98]. It follows, that the surface is actually partly O1-terminated. As will be shown later, hydrogen binds very strongly to this termination. Furthermore, experiments observed a high mobility of hydrogen on magnetite (001) at room temperature [130]. Therefore, it may be possible that hydrogen not only dissociates from formic acid upon adsorption, but also migrates to the O1-terminated regions. Another observation in the STM images and additional low-energy electron diffraction (LEED) analysis, is the formation of a triangular $(\sqrt{3} \times \sqrt{3})\mathrm{R}30^\circ$ superstructure on magnetite (111) upon adsorption of formic acid [98]. Calculating the energies of triangular adsorption structures indeed leads to a decrease in energy. However, the difference compared to the simple 1×1 structures is quite low with only 10 meV and 40 meV

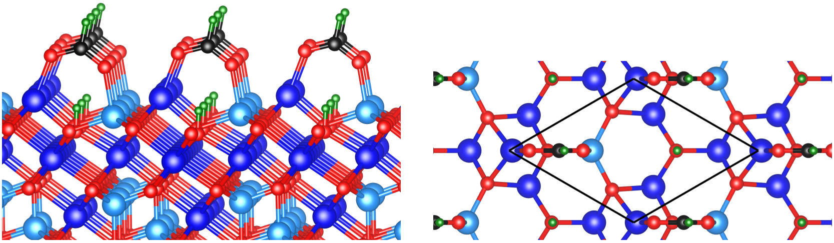

(a) bi-dentate adsorption on the oct2-termination

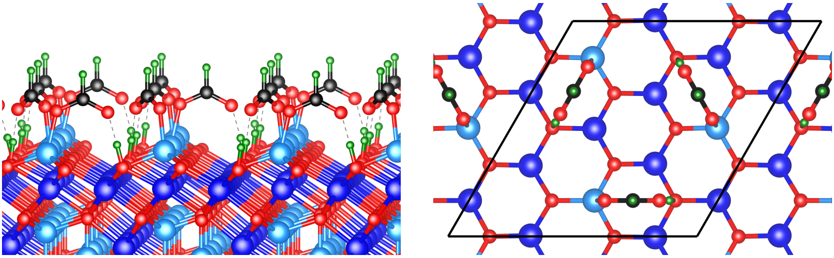

(b) qbd-$\upharpoonleft\downharpoonright$ triangular adsorption on the tet1-termination

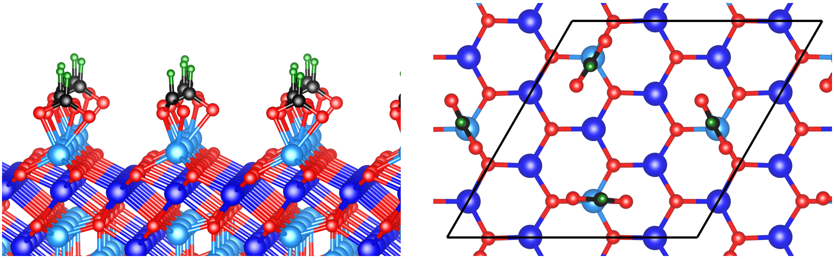

(c) chelating triangular adsorption on the tet1-termination

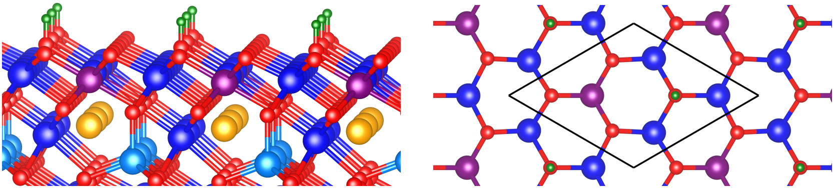

(d) hydrogen adsorption on the O1-termination

Figure 4.10: Adsorption geometries of formic acid on the different terminations of magnetite (111) at full monolayer coverage after structural optimisation with DFT. The different adsorption modes are shown in a side view (left) and a top view (right). Colour code: Fe_{oct} – dark blue, Fe_{tet} – light blue, Fe_{int} – violet, Fe vacancy – orange, O – red, C – black, H – green.

per molecule for the quasi-bi-dentate and chelating adsorption modes, respectively. Therefore, only the chelating configuration can form a stable triangular superstructure at room temperature (approximately 25 meV).

Full coverage formic acid adsorption is also studied on the oct2 termination of the Fe_3O_4 (111) surface. The oct2 termination has two iron atoms on the surface with a distance similar to the distance of the Fe_{oct} atoms on the (001) surface. Therefore, formate probably binds to this termination in a bidentate geometry with the dissociated hydrogen binding to a surface oxygen (see Figure 4.10). This hypothesis is confirmed by the calculated adsorption energy for this binding mode, which is -2.52 eV per molecule. Hence, it shows a much stronger binding than for many other surfaces [97, 139, 141, 142], including the bulk truncated magnetite (001) surface. As for the (001) surface, the dissociated hydrogen preferably adsorbs at the under-coordinated oxygen on the surface. Placing the hydrogen at another oxygen atom is much less favourable with an energy difference of 0.32 eV.

In contrast to the oct2 termination, formic acid adsorption is not favoured at all on the O1 terminated magnetite (111) surface. There are simply no adsorption sites for the oxygen atoms in the molecule, which usually contributes most to the surface binding. Nevertheless, due to the fact that the dissociated hydrogen may bind to O1 terminated patches on the surface, hydrogen adsorption on the O1 termination is discussed in more detail here. In principle, there are four oxygen atoms on the surface that the hydrogen can bind to (see Figure 4.10). However, three of these are equivalent adsorption sites due to the threefold rotational symmetry of the surface. Adsorbing hydrogen at one of the three symmetrical equivalent sites yields an adsorption energy of -2.04 eV, which is a bit less negative than for the adsorption at the remaining site, which yields -2.13 eV. In general, hydrogen adsorption on the O1 terminated surface is much more favourable than on the tet1 and oct2 terminated surfaces, where the adsorption energies are only -0.87 eV and -1.03 eV, respectively. Therefore, hydrogen may contribute to the stabilisation of O1 terminated patches on the magnetite (111) surface.

To assess the stability of all these different possible adsorption modes on the different terminations or even a mix of terminations, a surface phase diagram is calculated. The diagram displayed in Figure 4.11 shows the structures with the lowest surface free energies depending on the chemical potential of formic acid and oxygen in the surrounding gas phase. Each chemical potential value corresponds to a certain partial pressure (for more information see Chapter 2). The range of conditions where the oct2 termination is stable (green area) increases with increasing formic acid potential, but still does not enter the range of practically relevant pressures of 10^{-13} bar to 10^{4} bar. The tet1 termination (blue area), on the other hand, is most stable in vacuum and also at higher gas phase pressures with formic acid bound to it in the quasi-bi-dentate configuration as described above. Interestingly, there is a large range of conditions where both the tet1 and the O1 termination can coexist in the thermodynamic equilibrium (violet area). In this mixed termination structure, formate binds to the tet1 terminated patches in a chelating configuration, while the dissociated hydrogen binds to the O1 terminated patches.

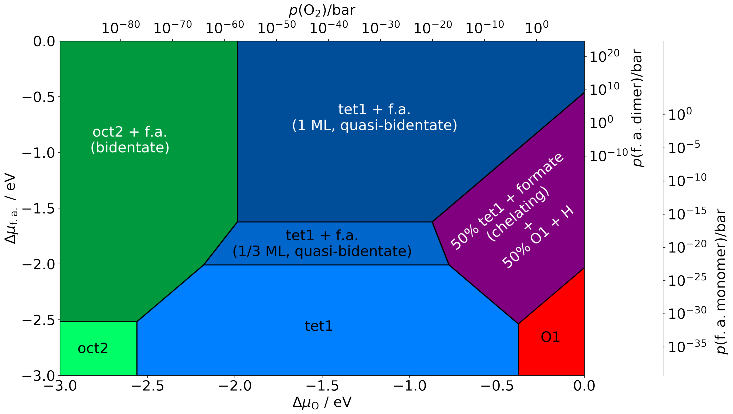

Figure 4.11: Calculated surface phase diagram of the Fe_3O_4 (111) surface in contact with gaseous formic acid (f.a.) and oxygen (O_2). The structures with the lowest surface free energies are shown depending on the chemical potential shifts $\Delta\mu$, which are converted to pressure scales on the top and right. Formic acid gas undergoes a monomer-to-dimer transformation in the range of 10^{-3} bar to 10^{-2} bar [135] (see Appendix D for more information).

These findings agree well with the aforementioned experimental results from STM images, as well as LEED and SXRD measurements that were published along with the computational results from this section in reference [98]. The oxygen and formic acid pressures chosen for the experiments at room temperature, were close to the calculated phase boundary between a pure tet1 termination with formic acid in the quasi-bi-dentate configuration (dark blue area in Figure 4.11), and the mixed tet1/O1 termination with formate in the chelating configuration and the dissociated hydrogen at the O1 terminated patches (violet area in Figure 4.11). In agreement with this prediction, the STM images show regions with triangular structures – an indication for the chelating formate configuration, and less structured regions indicating a quasi-bi-dentate binding. The LEED pattern confirms that there is a superstructure with $(\sqrt{3} \times \sqrt{3})\mathrm{R}30°$ periodicity, but the original 1×1 pattern is also still visible. The mixture of terminations appears in the SXRD measurement, where a tet1-layer occupation of only 80 % obtains the best fit with the diffraction data.

Insights from vibrational spectroscopy

Comparing vibrational spectra calculated using DFPT with FTIR spectra recorded in the same experimental conditions as before, provides clear evidence for a mixed adsorption mode. As for the (001) surface, the peaks for the stretching vibrations of the C=O double bond and the C–OH single bond of formic acid in the gas phase convert into an asymmetric σ_{as} and a symmetric σ_s O–C–O stretching peak with lower frequency splitting upon adsorption (see Figure 4.12a). However, the distance between those peaks is much larger for the different quasi-bi-dentate configurations than it is for the chelating configuration, which makes it possible to identify the binding mode from the vibrational spectrum. Another interesting result from the calculated spectra at low coverage is the shift of the O–H stretching peak $\sigma(O{-}H)$. The vibrational frequency of the O–H stretching vibration changes drastically depending on the adsorption mode, which is consistent with the fact that the binding of the hydrogen also changes significantly. Unfortunately, measuring the O–H stretching vibration is difficult because of the small size of the peak, and residual gas molecules that are often present in the chamber and on the surface. Otherwise, the position of this peak could also be used to identify the binding mode. The complete list of calculated vibrational modes and intensities can be found in Appendix D, and animations of the vibrational patterns of some important modes can be viewed in the online supporting material[2].

The spectra for a full coverage adsorption in Figure 4.12b show that the frequencies of the asymmetric (σ_{as}) and the symmetric (σ_s) O–C–O stretching vibrations are similar to the ones on the magnetite (001) surface for the chelating configuration, but shifted to a lower frequency for σ_s of the quasi-bi-dentate configuration. The shift can be attributed to the weaker binding in the hydrogen bond of the quasi-bi-dentate structure compared to the two strong Fe–O bonds in the chelating or bi-dentate bridging structures. The experimental FTIR spectrum has four peaks in the range where the O–C–O stretching vibrations occur. Even though the measured absolute vibrational frequencies are higher than the calculated ones due to the approximations in the calculation, the two pairs of peaks can clearly be attributed to the two binding modes, since their distances almost exactly match the computational result. This proves that both configurations are present in the experiment, which is in agreement with the results discussed above.

Combining the results from the different computational and experimental methods, the adsorption of formic acid on the (111) surface of magnetite can be summarised as follows: First, formic acid dissociates into formate and a proton that binds to an oxygen from the surface. The formate binds to one tetrahedral iron of the tet1 terminated surface and the newly formed hydroxyl group in a quasi-bi-dentate configuration. However, the hydrogen is most likely able to jump from one surface oxygen to another with the help of thermal activation, which also changes the binding mode of the formate. If the hydrogen is too far away, the quasi-bi-dentate configuration is not possible and changes to a chelating configuration, where both oxygen atoms of the formate bind to the tetrahedral iron. As the coverage increases, more and more hydrogen atoms move around on the surface until some of them get

---

[2] Visit `https://doi.org/10.15480/336.3408` for obtaining the online supporting material. The link can also be accessed by scanning the QR code at the beginning of Appendix D.

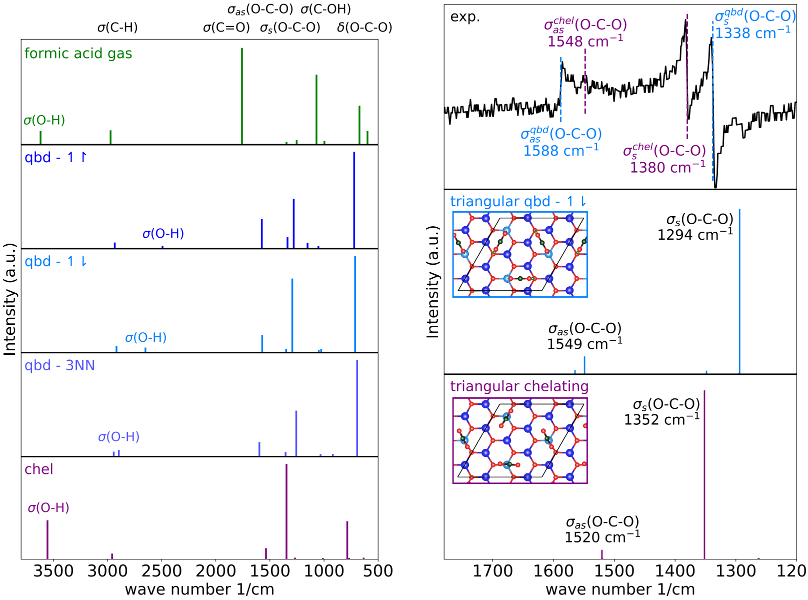

(a) (b)

Figure 4.12: Calculated vibrational spectra of formic acid in the gas phase and adsorbed on the tet1-termination of $\mathrm{Fe_3O_4}$ (111): (a) comparison of the whole spectrum for different adsorption configurations at low coverage (see Figure 4.9); (b) comparison of parts of the spectra for different configurations at full coverage (see Figure 4.10) with the experimental FTIR spectrum recorded by colleagues from DESY Nanolab (published in [98]).

trapped at O1 terminated patches that are caused by $\mathrm{Fe_{tet}}$ vacancies on the surface and offer a much stronger binding. This stabilises the defects and the chelating binding of the remaining formate. The chelating binding mode is further stabilised by a triangular superstructure, which can also be observed in diffraction experiments. Since some of the hydrogen still remains on the tet1 terminated part of the surface, some formate molecules remain in the quasi-bi-dentate configuration, in agreement with the mix of different adsorption structures observed by FTIR spectroscopy.

Concluding remarks

In this chapter, the interaction of magnetite (Fe_3O_4) surfaces with carboxylic acids, exemplified by formic acid (HCOOH), was studied in detail with computational ab-initio methods. Thereby, and through comparison with experimental results from collaborators at the DESY Nanolab, the mechanisms for the restructuring of these interfaces were revealed. On the magnetite (001) surface, which is most prominent in cubic nanoparticles, the adsorption of formic acid causes a change in the structure of the underlying surface. This increases the binding strength of the interface, which is expected to be beneficial in hybrid materials, and also for other applications. On the (111) surface, which is the dominant facet of octahedron shaped nanoparticles, the dissociative formic acid adsorption leads to a stabilisation of Fe vacancies on the surface. The separation of formate and dissociated hydrogen, which is linked to the stabilisation mechanism, may also be interesting for studies of the catalytic activity of this surface. Furthermore, the stabilisation of defective areas can be detrimental for the mechanical properties of hybrid materials, since defects are a source of mechanical failure.

Comparing the binding strength of the interfaces on $\{001\}$ and $\{111\}$ facets, yields surprisingly similar results. Even though the binding modes and coverages differ, the binding energies normalised by surface area are both in the range of $0.85\,\mathrm{J\,m^{-2}}$ to $0.95\,\mathrm{J\,m^{-2}}$. When nanoparticles are formed close to the thermodynamical equilibrium, the facet with the lowest surface free energy determines the particle shape. Since the two facets studied here are very close in their surface free energies, magnetite covered with carboxylic acids is predicted to form more or less spherical particles. In practice, different particle shapes can occur due to kinetic effects and additional molecules in the synthesis. Studying the kinetics of processes on the surface will also provide more insight into the chemical reactions during the growth process and the catalytic activity of magnetite surfaces. Furthermore, it is not clear yet, whether or not the reconstruction of the (001) surface is also lifted upon adsorption of other organic linkers, such as molecules with phosphorous acid or catechol anchoring groups, and how the binding energies translate to mechanical properties of a hybrid material.

The results presented here form an excellent starting point for these further studies. As a first step, a classical force field for molecular dynamics simulations of magnetite surfaces and interfaces, has been parametrised by colleagues from the molecular modelling group at the TUHH based on the energies, forces, and local charges calculated in this thesis [143]. The new force field allows to model much larger systems, such as interfaces linked by longer carboxylic acids or even small nanoparticle assemblies. The binding energies calculated in this thesis can also be employed in continuum mechanics models, in order to obtain more accurate failure simulations of hybrid materials. Finally, knowing the most stable adsorption configurations of formic acid on the magnetite surfaces is a prerequisite for studying reaction barriers of several catalytic processes.

5

Shape-control of titania nanoparticles

The shape of nanoparticles influences their properties. The reactivity in catalytic applications, for example, depends on how active different facets are, and on how much surface area is actually formed by the more active facets [144, 145]. In composite materials, the electrical and thermal conductivity, the magnetism, and the mechanical strength of the final material can be tuned by changing the shape of the particles [20, 146]. As such, controlling the shape during synthesis is desirable for these applications. However, testing the influence of different agents and reaction conditions on the shape of nanoparticles experimentally can be quite cumbersome or even dangerous, depending on the chemicals used. Understanding the shape-controlling effects beforehand, with the help of computational studies, can aid the development of new synthesis routes, which may result in new particle shapes or may improve the safety for the workers and the environment.

In this chapter, first the properties of titania (TiO_2) nanoparticles and their major facets are summarised. Then, the influence of different adsorbents and reaction conditions on the shape of the synthesised particles is studied and discussed. In current synthesis routes, hydrohalic and carboxylic acids are used, which is why the focus lies on understanding their influences and interactions here, so that future studies can go beyond these agents and study new molecules. A recent study proved that van-der-Waals interactions cannot be neglected for larger carboxylic acids adsorbed on TiO_2 surfaces [74]. Moreover, a comparison of results obtained with the PBE [30] and optB88-vdW [33, 34] functionals indicates that van-der-Waals interactions also play an important role in the binding of larger halides on TiO_2 surfaces. Therefore, all computational results presented in this chapter use the optB88-vdW functional. A detailed list of all computational settings can be found in Appendix A, while the comparison between functionals is presented in Appendix C. The main findings of this part of the thesis have been published in [147].

5.1 Titania nanoparticles and their major facets

Titania (titanium dioxide, TiO_2) has different polymorphs. While minerals mostly contain the tetragonal rutile and anatase phases, nanoparticles can also be synthesised in the orthorhombic brookite structure [148, 149]. In all of these three polymorphs the titanium atom is coordinated by an octahedron of six oxygen atoms as shown in Figure 5.1, but the connection of the coordination octahedra and their distortions differ depending on the polymorph. Rutile is the most stable polymorph of TiO_2 with the lowest formation enthalpy of the bulk structure, whereas anatase and brookite are metastable and convert to rutile when heated [150]. Nevertheless, the effect of lower surface energies and the influence of reaction kinetics make it possible to synthesise pure rutile, anatase, and brookite nanoparticles [148]. The shape control of anatase nanoparticles is particularly interesting, because of their good performance in photocatalytic applications and their facet-dependant catalytic activity, which is connected to facet-dependant adsorption energies [144]. Therefore, the shape-control study will be limited to anatase here.

There are numerous synthesis routes for creating anatase TiO_2 nanoparticles with different shapes and surfactants [149, 151, 152]. In general, aqueous and non-aqueous routes are distinguished depending on whether water is used as a solvent or not. Typical precursors for the synthesis are titanium-halide complexes (TiX_4, where $X = F, Cl, Br, I$), and reactions are performed at elevated temperatures of around 600 K. More details about a typical non-aqueous synthesis route can be found in [147, 149].

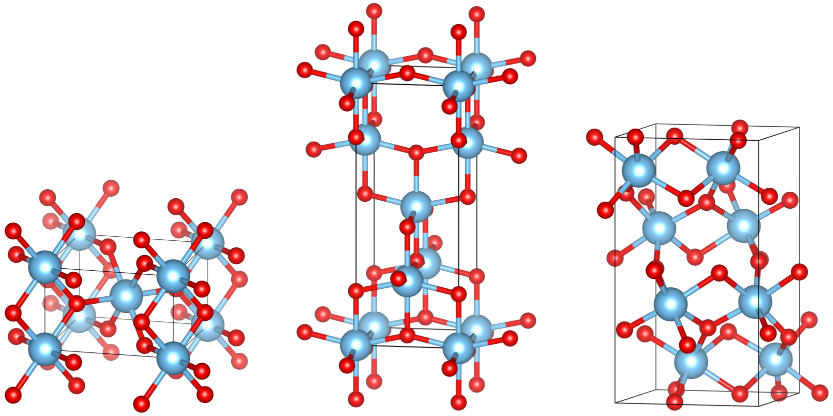

(a) Rutile **(b)** Anatase **(c)** Brookite

Figure 5.1: Atomic bulk structures of the three most prevalent polymorphs of titanium dioxide (TiO_2). Colour code: Ti – light blue, O – red.

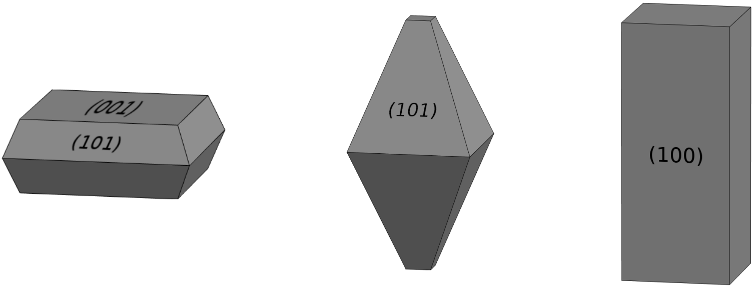

Figure 5.2: Common shapes of anatase TiO_2 nanoparticles. *Left*: Platelet shaped particle dominated by {001} facets. *Center*: Bi-pyramidal particle dominated by {101} facets. *Right*: Rod shaped particle dominated by {100} facets.

Depending on the precursor and surfactants used, anatase TiO_2 nanoparticles are synthesised in platelet, bi-pyramidal or rod shapes. Correspondingly, the major facets of interest are the {001}, {101}, and {100} facets, which dominate the different shapes (see Figure 5.2). Naturally occurring anatase crystals have a bi-pyramidal shape dominated by {101} facets, which were also shown to have the lowest surface free energy in calculations based on DFT [153]. Bi-pyramidal anatase nanoparticles usually also show a small percentage of the more reactive {001} facets on the top and bottom of the particle. Stabilising these facets increases the amount of {001} facets, while reducing the area of the {101} facets, which then leads to platelet shaped particles. Rod-shaped nanoparticles, on the other hand, can be synthesised by lowering the surface free energy of the {100} facets below the surface free energy of the {101} facets with the help of surfactants.

Structurally, there are major differences between the three facets of interest. The (101) surface is characterised by a sawtooth structure with exposed twofold coordinated oxygen atoms that connect the five- and sixfold coordinated titanium atoms in the surface layer (see Figure 5.3a). The resulting low density of under-coordinated titanium atoms is one of the reasons for the low reactivity of this surface in many catalytic processes. The more reactive (001) surface, on the other hand, is almost atomically flat and exposes only fivefold coordinated titanium atoms (see Figure 5.3c). However, due to the high tensile stresses present on this surface, a 1×4 reconstruction forms in ultra-high vacuum [154]. The additional ridge of TiO_2 with fourfold coordinated titanium atoms (see Figure 5.3d) shows strong binding to adsorbates and high reactivity. At the same time, it also blocks adsorption sites on the plateau below and reduces surface stresses. Therefore, the overall reactivity of the reconstructed (001)–1×4 surface is lower than on the unreconstructed (001)–1×1 surface [155]. The (100) surface structure combines elements of

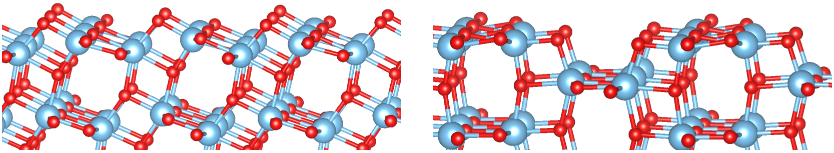

(a) (101) surface **(b)** (100) surface

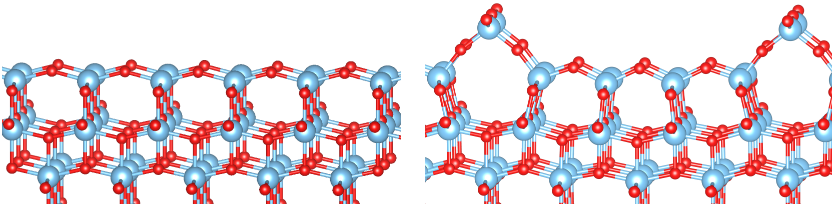

(c) (001) surface **(d)** (001) surface – (1×4) reconstruction

Figure 5.3: Atomic structures of the major facets of anatase TiO_2 nanoparticles. Color code: Ti – blue, O – red.

both the (101) and (001) surfaces. Densely arranged fivefold coordinated titanium atoms form plateaus capped by twofold coordinated oxygen atoms (see Figure 5.3b).

5.2 Interaction with hydrohalic acids

Because of their relevance for the synthesis of TiO_2 nanoparticles, the interaction of hydrohalic acids (HX, where $X=F, Cl, Br, I$) with titania surfaces has been partly studied theoretically before. Fluoride is known to stabilise the {001} facet of anatase nanoparticles, making them more platelet shaped. At first, the pure adsorption of fluoride was thought to be the cause of this stabilisation [145], but later studies found that a substitution of surface hydroxyl groups by fluoride stabilises the {001} facet even more [156, 157]. Taking the substitution concept further, an etching and dissolution of these surfaces takes place at higher HF concentrations, which can be used to form nano-ring structures [158]. Chloride adsorption stabilises the {101} facet, leading to bi-pyramidal particles [145]. Adding a combination of HF and HCl produces cuboid or rod-shaped particles [159], but the reason for this effect is not yet well understood. Shape-controlling effects or theoretical studies of the other halides (bromide and iodide) have not been reported so far. Also, even though the substitution of surface hydroxyl groups by fluoride ions is understood very well, a study of the same substitution process for the other halides was lacking in the literature. Therefore, the adsorption of all four different halides and the substitution of surface hydroxyl groups by them was studied comprehensively in this work.

Adsorption structures and energies

Hydrofluoric acid is known to adsorb dissociatively on anatase TiO_2 surfaces [156, 160]. Therefore, it is assumed that all the hydrohalic acids dissociate upon adsorption with the hydrogen binding to an oxygen, forming a surface hydroxyl group, and the halide binding to a titanium atom from the surface. As can be seen in Figures 5.4 and 5.5, the adsorption structures look similar for all hydrohalic acids. The only notable difference lies in the halide–titanium bond length, that increases with increasing atomic number. However, this increase is to be expected since the atomic radii also increase.

The calculated adsorption energies of all hydrohalic acids on the different anatase TiO_2 facets are listed in Table 5.1. All adsorption energies are negative, indicating that adsorption of all hydrohalic acids is energetically favourable on all three facets of anatase nanoparticles. Comparing the different halides, one can observe that the order of adsorption energies on all surfaces is $E_{\mathrm{ad}}(\mathrm{HF}) < E_{\mathrm{ad}}(\mathrm{HBr}) < E_{\mathrm{ad}}(\mathrm{HI}) < E_{\mathrm{ad}}(\mathrm{HCl})$. Interestingly, HCl breaks the ordering by atomic numbers, which is valid for the halide–titanium bond lengths, and adsorbs even weaker than HI. Another difference appears for the order of the adsorption energies comparing different facets. Hydrofluoric acid adsorbs most strongly on the (001) surface, while the other hydrohalic acids preferably adsorb on the (101) surface. A comparison with the existing literature on HF and HCl adsorption [156, 159, 160] yields a qualitative agreement. Quantitative agreement cannot be reached though, because the adsorption energies are more negative here due to the van-der-Waals interactions, which were not included in the cited studies.

Table 5.1: Calculated adsorption energies per molecule (E_{ad} in eV) of the hydrohalic acids on different anatase TiO_2 surfaces. Adsorption energies of the reconstructed (001)–1×4 surface are given for one molecule per unit cell (ridge, plateau) and three molecules per unit cell (high cov.).

Species	$E_{\mathrm{ad}}(101)$	$E_{\mathrm{ad}}(100)$	$E_{\mathrm{ad}}(001)$ 1×1	$E_{\mathrm{ad}}(001)$–1×4 ridge	plateau	high cov.
HF	−1.41	−1.33	−1.43	−1.59	−0.76	−0.99
HCl	−1.25	−1.11	−1.12	−1.26	−0.53	−0.74
HBr	−1.36	−1.21	−1.19	−1.31	−0.62	−0.82
HI	−1.34	−1.17	−1.12	−1.19	−0.58	−0.74

Lifting of the (001) 1×4 reconstruction

So far, only the adsorption structures and energies for the unreconstructed 1×1 anatase TiO_2 (001) surface were shown in Figure 5.5. However, as mentioned before, the (001) surface can also form a 1×4 reconstruction. In hydrofluoric and carboxylic acid solutions this reconstruction can be lifted [155], meaning that the surface structure reverts back to the 1×1 unit cell. The effect has

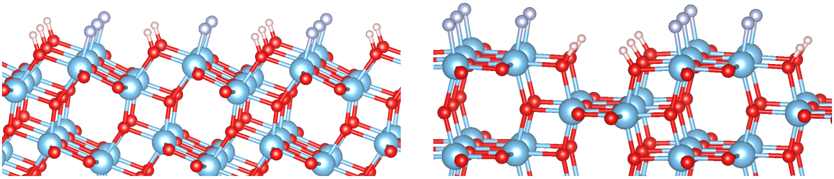

(a) HF adsorption on (101) **(b)** HF adsorption on (100)

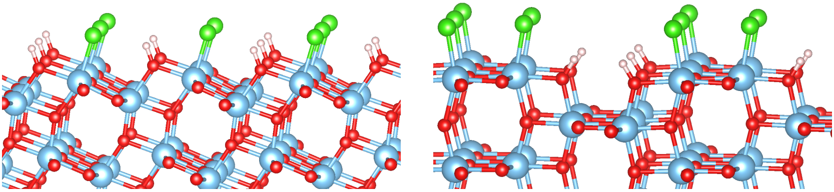

(c) HCl adsorption on (101) **(d)** HCl adsorption on (100)

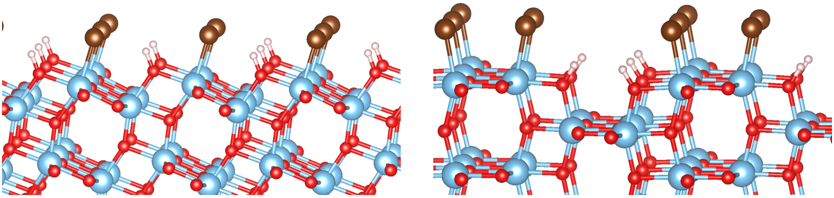

(e) HBr adsorption on (101) **(f)** HBr adsorption on (100)

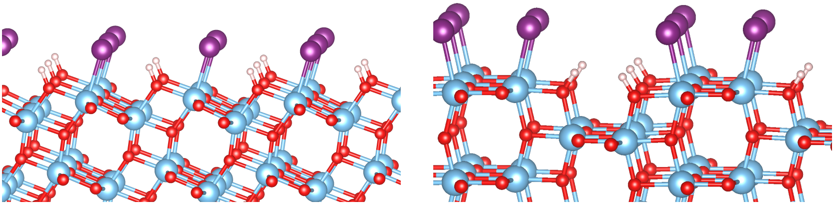

(g) HI adsorption on (101) **(h)** HI adsorption on (100)

Figure 5.4: Adsorption structures of different hydrohalic acids on the anatase TiO_2 (101) and (100) surfaces. Colour code: Ti – blue, O – red, H – white, F – silver, Cl – green, Br – brown, I – violet.

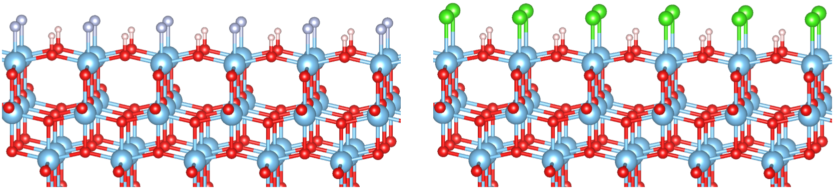

(a) HF adsorption

(b) HCl adsorption

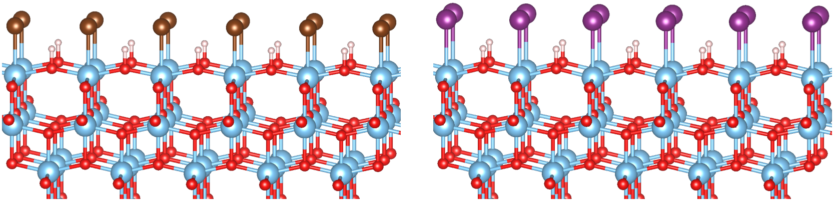

(c) HBr adsorption

(d) HI adsorption

Figure 5.5: Adsorption structures of different hydrohalic acids on the anatase TiO_2 (001) surface. Colour code: Ti – blue, O – red, H – white, F – silver, Cl – green, Br – brown, I – violet.

not been studied yet for the other hydrohalic acids though. Considering the difference in the adsorption energies on the unreconstructed surface, there might also be a difference in the lifting of the reconstruction for different halides.

Here, the adsorption on the reconstructed (001)–1×4 surface was studied for all hydrohalic acids at two different coverages: a low coverage of only one molecule per surface unit cell and a higher coverage of three adsorbed molecules per surface unit cell. The calculated adsorption structures are shown in Figure 5.6. As observed for the other surface structures, there is no apparent difference in the adsorption structures of different halides apart from the increasing halide–titanium bond length with increasing atomic number. At low coverage, the adsorption at the highly reactive additional ridge site is more favourable than on the unreconstructed (001)–1×1 surface, whereas the adsorption energies on one of the plateau sites are less favourable (see Table 5.1). At high coverage, this results on average in a less negative adsorption energy per molecule compared to the unreconstructed (001)–1×1 surface.

The adsorption energies already indicate that a lifting of the reconstruction is favoured in hydrohalic acid environments. Another indication comes from

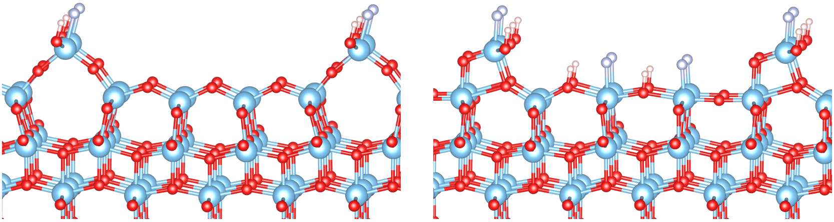

(a) Low coverage HF on (001) – 1×4 **(b)** High coverage HF on (001) – 1×4

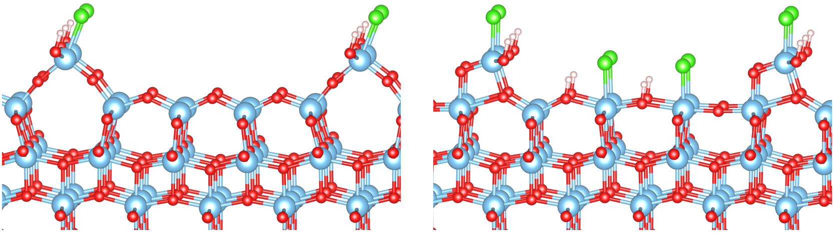

(c) Low coverage HCl on (001) – 1×4 **(d)** High coverage HCl on (001) – 1×4

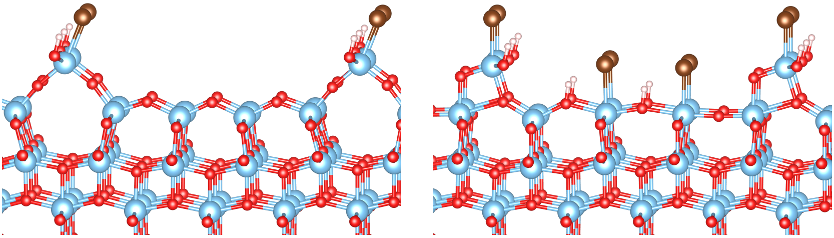

(e) Low coverage HBr on (001) – 1×4 **(f)** High coverage HBr on (001) – 1×4

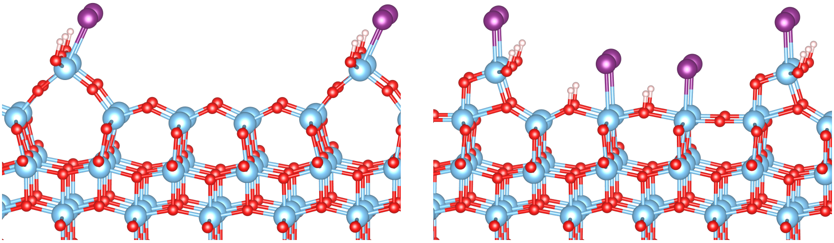

(g) Low coverage HI on (001) – 1×4 **(h)** High coverage HI on (001) – 1×4

Figure 5.6: Adsorption structures of the hydrohalic acids on the 1×4 reconstruction of the anatase TiO_2 (001) surface at different coverages. Colour code: Ti – blue, O – red, H – white, F – silver, Cl – green, Br – brown, I – violet.

the adsorption structures at higher coverage (cf. Figures 5.6b,d,f,h), where the surface structure basically reverts back to the unreconstructed state. The additional row of TiO_2HX does not change the underlying surface structure after adsorption of hydrohalic acids, but just adsorbs on the surface. It can be concluded, that the tensile stresses causing the reconstruction [154] are released by the adsorption of hydrohalic acids and therefore, the reconstruction is lifted in hydrohalic acid environments. Hence, in the following only the unreconstructed (001)–1×1 surface will be studied and discussed.

Substitution structures and energies

As mentioned before, the hydroxyl (–OH) groups on the anatase TiO_2 surfaces can be substituted by halides. Seeing as the formal charges of the OH^- group and the substituting halide (X^-) are the same, charge neutrality is conserved by the substitution. The hydroxyl then combines with the proton from the hydrohalic acid, so the full chemical reaction can be written as

$$\mathrm{Ti}_n\mathrm{O}_{2n}\mathrm{HX} + \mathrm{HX} \longrightarrow \mathrm{Ti}_n\mathrm{O}_{2n-1}\mathrm{X}_2 + \mathrm{H}_2\mathrm{O}. \tag{5.1}$$

Hence, the substitution energy is the difference between the energies of the products and reactants in this reaction

$$E_{\mathrm{sub}} = \frac{1}{M}[E_{\mathrm{slab,sub}} + M \cdot E_{\mathrm{H_2O}} - (E_{\mathrm{slab,ad}} + M \cdot E_{\mathrm{HX}})], \tag{5.2}$$

where the factor M takes into account that more than one surface hydroxyl group may be substituted by a halide.

The calculated substitution structures and the corresponding substitution energies are displayed in Figures 5.7 and 5.8, and in Table 5.2. The fluoride substitution structures and energies agree with existing results of Wang et al. for the (001) and (101) surfaces, given the differences in the computational settings [156]. On all surfaces, the OH-substituting fluoride relaxes inwards compared to the original position of the surface oxygen, which can be connected to the slightly shorter Ti–F bond length of 1.8 Å to 1.9 Å compared to the Ti–O bond length of 2.0 Å. The other halides have larger Ti–X bond lengths in the range of 2.3 Å to 3.0 Å and relax outwards, which even leads to a breaking of titanium–halide bonds in some cases.

Table 5.2: Calculated substitution energies per substitution (E_{sub} in eV) for the hydrohalic acids on different anatase TiO_2 surfaces.

Species	$E_{\mathrm{sub}}(101)$	$E_{\mathrm{sub}}(100)$	$E_{\mathrm{sub}}(001)$
HF	−0.11	−0.24	−0.40
HCl	0.47	0.30	2.43
HBr	0.77	0.60	1.83
HI	1.19	1.11	1.06

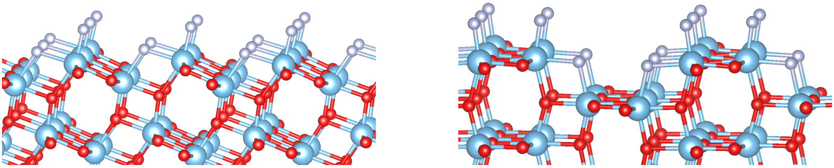

(a) F on (101) **(b)** F on (100)

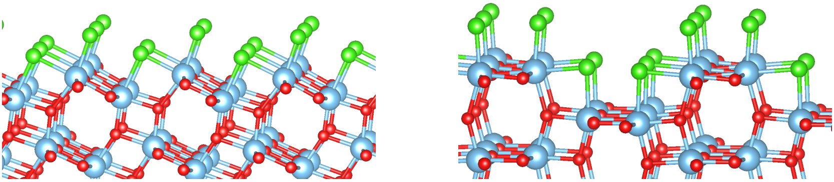

(c) Cl on (101) **(d)** Cl on (100)

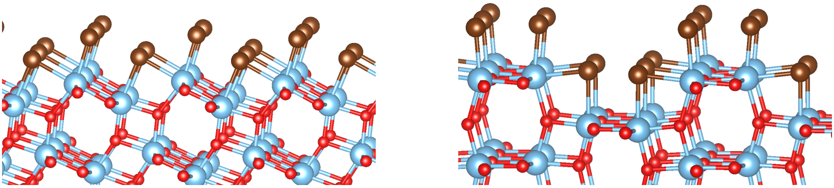

(e) Br on (101) **(f)** Br on (100)

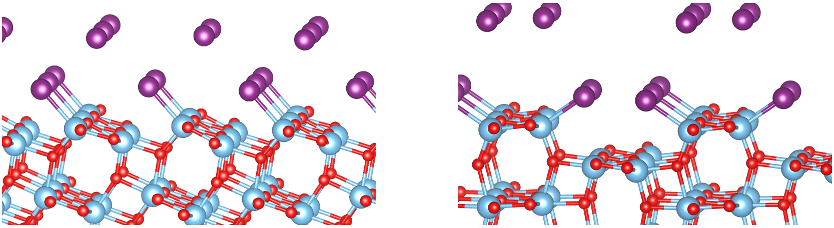

(g) I on (101) **(h)** I on (100)

Figure 5.7: Adsorption structures of different hydrohalic acids on the anatase TiO_2 (101) and (100) surfaces including substitution of the surface hydroxyl groups by halides. Colour code: Ti – blue, O – red, F – silver, Cl – green, Br – brown, I – violet.

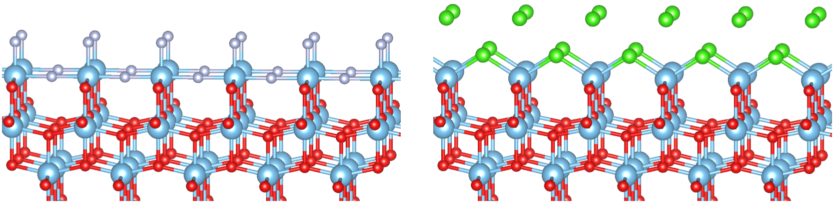

(a) F on (001) **(b)** Cl on (001)

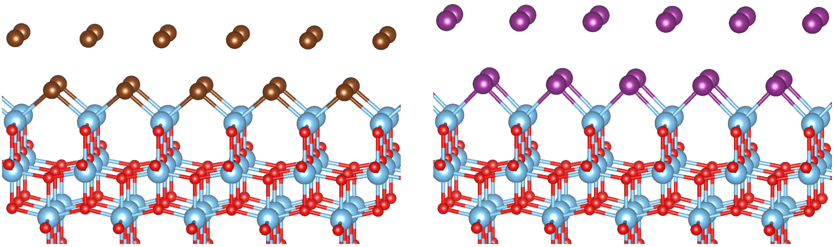

(c) Br on (001) **(d)** I on (001)

Figure 5.8: Adsorption structures of different hydrohalic acids on the anatase TiO_2 (001) surface including substitution of the surface hydroxyl groups by halides. Colour code: Ti – blue, O – red, F – silver, Cl – green, Br – brown, I – violet.

In agreement with the differences in this lattice mismatch, the substitution energies are only negative for a substitution of surface hydroxyl groups by fluoride and are positive for the other halides. At the (101) and (100) surfaces, the substitution energies increase with increasing atomic number, giving further evidence that the lattice mismatch is the most important factor for a possible substitution. However, the calculated substitution energies for the (001) surface show an opposite trend, which can be understood from the stresses present in this surface. On a clean (001) surface, the tensile stress is released through the formation of a 1×4 reconstruction, but as mentioned before, adsorbing hydrohalic acids also releases the tensile stress. When the surface hydroxyl groups are substituted by an outwards relaxing halide, the tensile stress might be reintroduced, because the connected titanium atoms are attracted by the halide and pulled outwards too. Larger halides can counterbalance this effect, since their size gives rise to compressive surface stress caused by the larger titanium–halide distance.

Insights from surface phase diagrams

The prediction of particle shapes is based on the surface free energies of the different facets (see Chapter 2, Section 2.5). In short, the facet with the lowest surface free energy will be the dominant facet of the nanoparticle, and therefore, determine the shape of the particle. The connection between the dominating facet and the particle shape for anatase TiO_2 nanoparticles was already shown in Figure 5.2. At 0 K, the surface free energies follow directly from the total energies calculated with DFT (see Table 5.3). However, since particle synthesis is performed at finite temperatures, an accurate prediction of equilibrium particle shapes necessitates a model that takes into account the reaction conditions. As described in Chapter 2 (Section 2.4), this can be achieved by including temperature and concentration effects through the chemical potential of the adsorbate species. The surface free energies of the different facets then depend linearly on these chemical potential shifts compared to the results obtained with DFT for a temperature of 0 K. Surface phase diagrams plot the surface phases with the lowest surface free energy depending on the chemical potential shifts. This allows to predict the most stable facet for different sets of conditions and makes it easier to understand how a change in conditions will affect the particle shape.

For the influence of hydrohalic acids on the shape of anatase TiO_2 nanoparticles, the chemical potential shifts of the hydrohalic acid $\Delta\mu_{\mathrm{HX}}$ and of water $\Delta\mu_{\mathrm{H_2O}}$ have to be taken into account. Even though adsorption of water on TiO_2 surfaces is not considered here, it plays an important role for the stability of the substitution structures, as demonstrated by Equations (5.1) and (5.2). In general, a high chemical potential corresponds to a high concentration of that component, but the exact conversion is more complex and depends on the temperature. Figure 5.9 shows the most stable facets and surface structures depending on the water and hydrohalic acid chemical potential shifts for the different halides. Noticeably, all halides are able to form substitution structures, even though only HF has negative substitution energies at 0 K. Still, for HF the substitution structures already become favourable at a very low HF chemical potential, while a higher HX chemical potential is required for the other halides to substitute surface hydroxyl groups. Furthermore, these

Table 5.3: Calculated surface free energies in J m^{-2} at 0 K excluding (γ_0) and including ($\tilde{\gamma}_0$) the substitution process for the hydrohalic acids adsorbed on different anatase TiO_2 surfaces.

Species	$\gamma_0(101)$	$\gamma_0(100)$	$\gamma_0(001)$	$\tilde{\gamma}_0(101)$	$\tilde{\gamma}_0(100)$	$\tilde{\gamma}_0(001)$
none	0.77	0.89	0.92	–	–	–
HF	−0.37	−0.26	−0.27	−0.46	−0.47	−0.71
HCl	−0.23	−0.08	0.07	0.14	0.19	2.75
HBr	−0.33	−0.16	0.00	0.29	0.36	2.02
HI	−0.31	−0.12	0.08	0.65	0.84	1.25

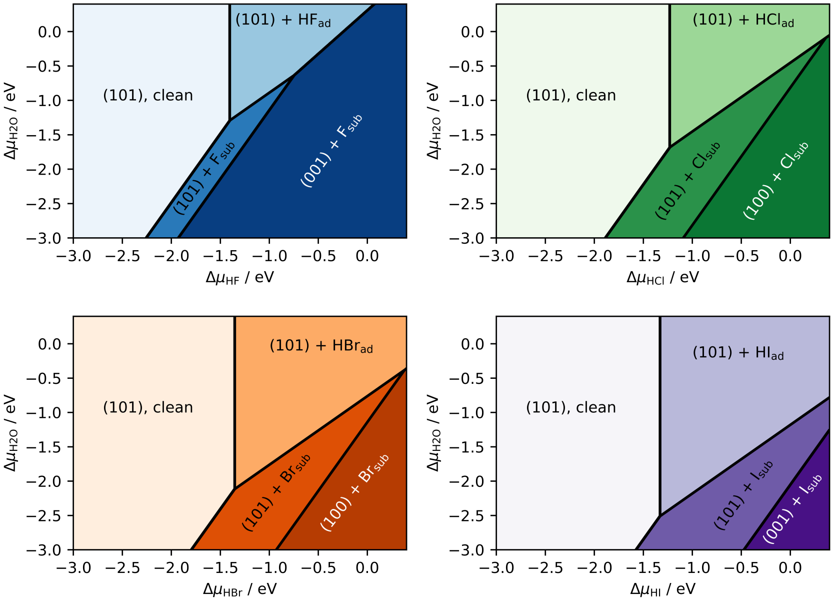

Figure 5.9: Surface phase diagrams showing the most stable surface structures of anatase TiO_2 nanoparticles in hydrohalic acid environments depending on the chemical potential shifts of water ($\Delta\mu_{H_2O}$) and the corresponding acid ($\Delta\mu_{HX}$).

diagrams indicate that due to the difference in the water chemical potential, the substitution process is more stable in non-aqueous synthesis routes than in aqueous synthesis routes. The HF surface phase diagram also illustrates that the substitution process is responsible for the known stabilisation of the {001} facet, which leads to platelet shaped particles.

The experimental observation that a combination of added HF and HCl leads to cuboid shaped particles [157, 159] can now be explained with the help of the surface phase diagrams in Figure 5.9. Higher concentrations of hydrochloric acid stabilise the {100} facets through the substitution of surface hydroxyl groups. Combined with the stabilisation of the {001} facets by fluoride, cuboid shaped particles become the favourable equilibrium particle shape. Similar results can be expected for the addition of HBr, which also stabilises the {100} facets through the substitution process. For HI, on the other hand, the most stable facet only changes in rather extreme conditions, i.e. very high HI chemical potential and very low water chemical potential.

5.3 Competitive adsorption with carboxylic acids

Apart from the hydrohalic acids stemming from the pre-cursor of the TiO_2 nanoparticle synthesis, carboxylic acids also play an important role in the chemical process. In non-aqueous synthesis, carboxylic acids are the source of the oxygen atoms needed to create TiO_2 [149]. As aforementioned, carboxylic acids are also used as capping agents and for the functionalisation of nanoparticles. Therefore, in order to fully comprehend the shape control during TiO_2 nanoparticle synthesis, the influence of carboxylic acids on the particle shape and the competitive adsorption processes between carboxylic and hydrohalic acids have to be understood. Here, two carboxylic acids – acetic acid and benzoic acid – are studied as representatives of the large family of relevant carboxylic acids. Acetic acid is a small molecule that occurs in nature and is usually present when working in ambient conditions [161]. Benzoic acid has a π-bonded system and shows significant van-der-Waals interactions with neighbouring adsorbates [74], which is why it can be considered as a representative for larger carboxylic acids with a significant amount of van-der-Waals bonds in general.

The adsorption energies and structures of acetic and benzoic acid were not calculated in this work, but in the PhD-Thesis of Wolfgang Heckel [59] and also published jointly in [147], where they can be reviewed. The adsorption energies are displayed in Table 5.4 for comparison along with the surface free energies at 0 K. Comparing the adsorption energies with the hydrohalic acid adsorption energies in Table 5.1, clearly shows that the carboxylic acids adsorb more strongly on anatase TiO_2 surfaces. The only exception to this rule is a full coverage adsorption on the (001) surface, where the carboxylic acid adsorption energies are comparable to or even lower than the ones for the hydrohalic acids. Interestingly, there is a strong coverage dependence of the hierarchy of adsorption energies on the different facets. While a stabilisation of the {100} and {001} facets is observed for a half-covered surface, at full coverage the hierarchy is inverted and the adsorption energies are lowest on the (101) surface.

As for the hydrohalic acids, a clear and complete picture can only be gained

Table 5.4: Calculated adsorption energies per molecule (E_{ad} in eV) and surface free energies at 0 K (γ_0 in $\mathrm{J\,m^{-2}}$) for acetic acid (a.a.) and benzoic acid (b.a.) on different anatase TiO_2 surfaces. Adsorption energies are taken from [59] and also published jointly in [147].

Species	θ	$E_{\mathrm{ad}}(101)$	$E_{\mathrm{ad}}(100)$	$E_{\mathrm{ad}}(001)$	$\gamma_0(101)$	$\gamma_0(100)$	$\gamma_0(001)$
a.a.	0.5	−1.61	−1.90	−1.91	0.11	0.06	0.25
	1.0	−1.50	−1.43	−1.43	−0.45	−0.36	−0.28
b.a.	0.5	−1.82	−2.16	−2.22	0.03	−0.06	0.08
	1.0	−1.79	−1.67	−0.48	−0.69	−0.57	0.78

by including the effect of the chemical environment and finite temperature with the help of surface phase diagrams. Especially the stability in a mixed environment of carboxylic and hydrohalic acids is of interest, since it resembles the real conditions as close as possible. The computed surface phase diagrams for these environments are shown in Figure 5.10. To simplify the analysis, the water chemical potential shift is set to $-1.1\,\mathrm{eV}$ for these diagrams, which corresponds to gaseous water at $600\,\mathrm{K}$ [51]. The synthesis of anatase TiO_2 nanoparticles is usually performed at this temperature [149], which is why this setting should allow insights in the shape controlling effects in experimental conditions.

Examining the phase diagrams in Figure 5.10, there is no qualitative difference between acetic acid and benzoic acid, even though both molecules have quite different structures. Therefore, it can be assumed that the results presented here are valid for a wide range of carboxylic acids. At half coverage, carboxylic acids stabilise the $\{100\}$ facets of anatase TiO_2, which would lead to rod-shaped particles. However, the stability range of the half-covered surface is quite narrow, which is why usually bi-pyramidal particles dominated by $\{101\}$ facets are expected to be formed in carboxylic acid environments.

The phase diagrams for competitive adsorption with a fixed water chemical potential uncover a clear trend for the hydrohalic acids. All hydrohalic acids stabilise the $\{101\}$ facets, and hence, bi-pyramidal particle shapes, in their adsorption configurations. However, the stability range of this phase changes with the atomic number. While fluoride shows a very narrow stability range, the stability range increases with atomic number, resulting in a stability of the $\{101\}$ facets over the whole range shown for HI. As aforementioned, substitution structures that stabilise different facets only become energetically favourable at higher concentrations. In conclusion, the shape-controlling effects of HI and HBr upon changing their concentration are expected to be lower than those of HF and HCl.

Finally, when analysing the competitive adsorption of carboxylic versus hydrohalic acids, an increase of the stability range of the carboxylic acids with increasing atomic number of the hydrohalic acids is observed. In combination with the differences in the adsorption energies between carboxylic and hydrohalic acids, this means that HCl, HBr, and HI adsorbed on the surface of anatase TiO_2 nanoparticles are expected to be replaced by carboxylic acids. Hydrofluoric acid, on the other hand, could stay on the surface blocking carboxylic acid adsorption sites. Especially on the $\{001\}$ facets, where HF adsorbs most strongly and also replaces surface hydroxyl groups, HF may be difficult to replace with carboxylic acids for a functionalisation of the nanoparticles.

These theoretical predictions are confirmed by experiments performed by colleagues from the nano-chemistry group (AG Weller) at the University of Hamburg on nanoparticles synthesized with different TiX_4 precursors, where $X = F, Cl, Br, I$, and with oleic acid as oxygen source and capping agent. The particle synthesis and experiments are described in detail in a joint publication [147]. The results show that nanoparticles synthesised starting from TiF_4 have a significant amount of fluoride on their surfaces even after thorough washing procedures. The other halides Cl, Br, and I, though, are proven to be

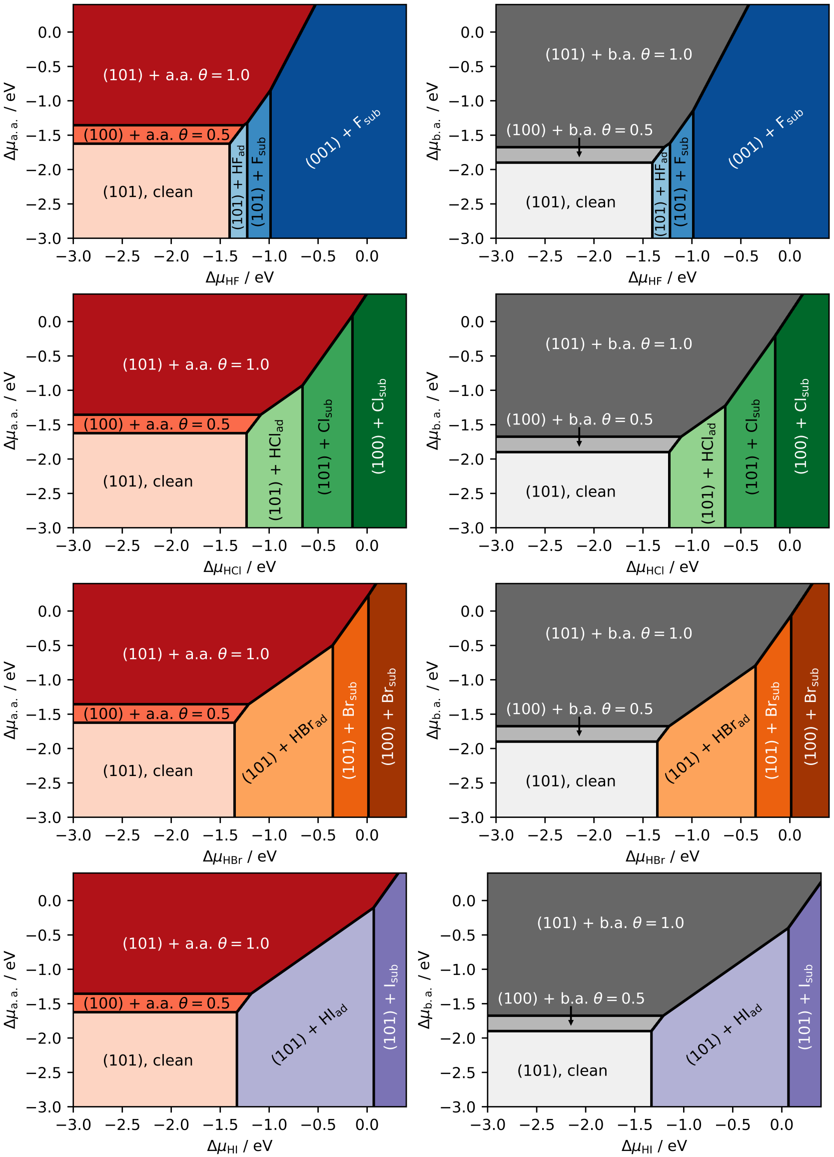

Figure 5.10: Surface phase diagrams showing the most stable surface structures of anatase TiO_2 nanoparticles in environments containing both hydrohalic (HX, X=F, Cl, Br, I) and carboxylic acids (acetic acid – a.a. or benzoic acid b.a.). $\Delta\mu_{H_2O}$ is set to -1.1 eV for the substitution structures, corresponding to gaseous water at the reaction temperature of 600 K.

removed and replaced by oleic acid after a few washing steps. Furthermore, the particle shapes match the theoretical predictions. For TiF_4 precursors, platelets or even thin sheets are observed as products, while bi-pyramidal particles are formed when using other TiX_4 precursors.

Concluding remarks

In this chapter, the shape-controlling effects of hydrohalic and carboxylic acids during anatase TiO_2 nanoparticle synthesis were studied with the help of calculations based on density functional theory. A thorough investigation of the adsorption structures and energies of all the hydrohalic acids on the most important facets of anatase TiO_2 nanoparticles was performed. Similar adsorption structures were observed, and a lifting of the 1×4 reconstruction on the $\{001\}$ facets upon adsorption is predicted. The known substitution of surface hydroxyl groups by fluoride was also studied for the other halides, revealing a new explanation for the stabilisation of cuboid shaped particles through addition of hydrochloric acid (HCl): At high HCl concentrations, the substitution of surface hydroxyl groups by chloride stabilises the $\{100\}$ facets. Surface phase diagrams enable the prediction of shape-controlling effects and provide a detailed view on competitive adsorption processes in mixed hydrohalic and carboxylic acid environments under reaction conditions. Carboxylic acids adsorb more strongly on anatase TiO_2 nanoparticles than most hydrohalic acids, and they stabilise the bi-pyramidal particle shape. Therefore, in agreement with experimental observations, the nanoparticles are usually capped by carboxylic acids. The only exception is HF, which has similar adsorption energies to the carboxylic acids and can be further stabilised through the substitution process.

In conclusion, these results show how electronic structure calculations in combination with thermodynamic models can help to understand and disentangle different influences on the particle shape during synthesis. Future studies may focus on the screening of different candidate molecules that can be added to the synthesis in order to change the resulting shapes. With respect to the application in hybrid materials, it may be interesting to also search for combinations of surfactants that exhibit a facet-selective adsorption, which could enable interlinking of nanoparticles depending on their relative orientation. Another interesting research idea is to take a more detailed look at the density of electronic states of the substitution structures, in order to find out, if there is an influence on the catalytic activity.

6

Mechanical properties of hybrid interfaces

As described in the introduction, improving and understanding the mechanical properties of hybrid materials made from metal oxide nanoparticles and carboxylic acid linkers is one of the main motivations for this work. In the previous chapters, important influencing factors, such as binding energies and geometries, the underlying surface structure, and the shape of nanoparticles were studied in detail. However, it is not yet clear how much those different factors affect the resulting properties. Therefore, the aim of this part of the thesis is to build a virtual mechanical testing device, which allows to simulate the stress-versus-strain curve of hybrid interfaces at the atomic scale. Of course, applying ab-initio methods to study the mechanical properties necessitates approximations and simplifications of the real problem to limit the computational costs. Nevertheless, these calculations help to understand the failure mechanism of the interfaces, and to identify the most important influencing factors. With this information at hand, experimentalists can change the atomic structure of the interfaces to enhance the mechanical properties of the final material. Furthermore, the results of the ab-initio calculations presented in this chapter can also be used for the parametrisation of classical force fields or continuum models. Thereby, a link between the simulation methods on different length and time scales is created, enabling a true multi-scale simulation approach.

6.1 Setting up a virtual mechanical testing device

Modelling interfaces

A first step to build a virtual mechanical testing device, is to create load scenarios that will be modelled. In the hybrid materials relevant to this work, the stress is concentrated in the contact areas between the particles [162]. Therefore, modelling these contacts is of utmost importance for understanding the mechanical properties of hybrid materials and enhancing the accuracy of multi-scale simulations. Figure 6.1 schematically shows possible approximations for the atomic structure of particle surfaces connected by carboxylic acids. Double bonds between carbon atoms in the organic molecule chains are used to ease the cross-linking between the molecules (Figures 6.1a and 6.1b). This increases the strength of the material significantly [17] as the result of the weak van-der-Waals bonding being replaced by stronger covalent bonds. However, a single carboxylic acid linking the two surfaces with two anchoring groups (see Figure 6.1c) can serve as a first approximation for this molecular network. The simplified model further facilitates studying the influence of different binding modes or double bonds that remain after the cross-linking process (Figure 6.1d).

Despite the fact that these initial models are quite general, there are still some approximations that should already be kept in mind. First and fore-

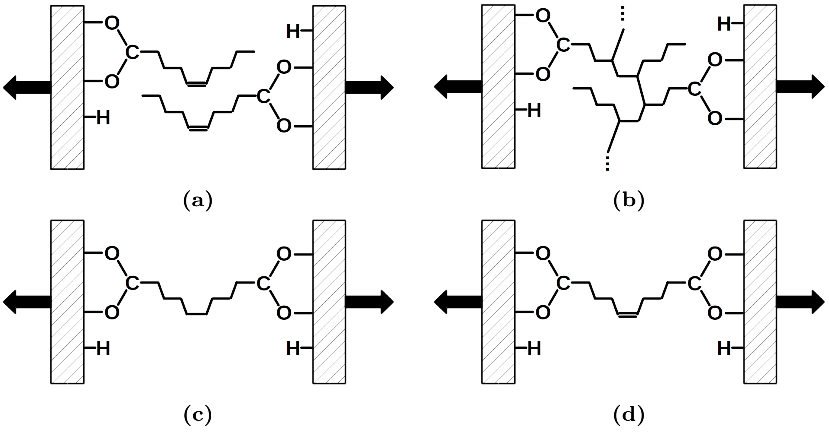

(a) (b) (c) (d)

Figure 6.1: Illustration of possible interface structures for carboxylic acid interfaces. (a) Two carboxylic acids with a double bond, only connected by van-der-Waals interaction. (b) Interlinked carboxylic acids, forming a covalently bonded network in the interface. (c) Molecule with two carboxylic acid end groups interlinks the two surfaces. (d) Molecule with two carboxylic acid end groups and a double bond interlinks the two surfaces.

most, the curved nanoparticle surfaces are approximated by flat and parallel surfaces. This allows for the application of methods with periodic boundary conditions, and reduces the computational costs, due to the fact that less atoms are needed in the simulation cell. On the other hand, changing the geometry of the system means that the mechanical properties of the final material can not be predicted quantitatively. Qualitative predictions, however, may still be valid, and the calculated stress-strain relationship can be included in larger scale continuum models that simulate the real structure of the hybrid material. Another approximation is the limitation to some atomic configurations that are expected to be representative of the real structure. This is necessary to reduce the computational costs to a practicable level, but also opens up the risk of missing important configurations. Methods for a more detailed, and therefore also more expensive, sampling of the configuration space are, for example, the process introduced in Chapter 3 or Molecular Dynamics simulations at finite temperatures.

Applying an external force

The next step is to choose a method of applying a force to the interface. An excellent recent review describes the different approaches currently available for applying and analysing forces in ab-initio calculations of molecules [163]. For this work, the method of constrained geometries simulating an external force (COGEF, [164]) was chosen, since it is easy to implement, especially for larger systems, and it does not diverge when the interface breaks. In the COGEF-method, one or more internal coordinates of the system are fixed, while the other coordinates are allowed to relax for energy minimisation. The fixed coordinate is varied systematically, causing a force on the constrained atoms. The method is very easy to apply, but in many cases there is no clear reasonable choice of internal coordinates to fix. In the case of the interface models relevant for this work (see Figure 6.1), though, the natural choice of constraints is to fix the outer layers of the left and right surface slabs to simulate the bulk structure of the rigid centre of the particles. As illustrated in Figure 6.2, the interface that is allowed to relax then consists of some layers in the surface, and of the molecules connecting the surfaces. The external force on the interface is simulated by displacing the fixed atoms in the right surface slab, and thereby changing the distance between the fixed atoms of the two surface slabs.

The external force appears not only on the displaced atoms, but also on the fixed atoms on the other side of the interface slab model with the opposite sign. Averaging over the (negative) atomic forces in the fixed layers on one side of the slab yields the total (external) force $\vec{F}$ on the interface. The normal stress σ_n on the interface then follows from projecting the total force on the surface normal vector $\vec{n}$ and dividing by the surface area A. The shear stress (τ_i or σ_{ni}) along one of the surface vectors $\vec{a}_i$ is evaluated in the same manner:

$$\sigma_n = \frac{\vec{F} \cdot \vec{n}}{A} \quad \text{and} \quad \tau_i = \frac{\vec{F} \cdot \vec{a}_i}{A} \tag{6.1}$$

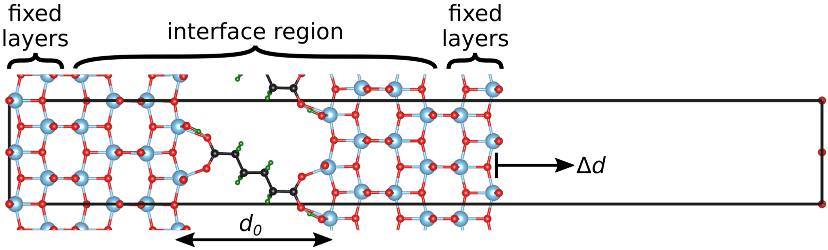

Figure 6.2: Illustration of the interface slab model used in this chapter. The outer layers are fixed to their bulk positions, while the other atoms are allowed to relax. Changing the distance between the fixed layers by Δd simulates the interface under stress (COGEF approach). The strain is calculated with respect to the inner surface distance d_0 in the unstrained state. Colour code: Ti – blue, O – red, C – black, H – green.

Increasing the distance along the direction perpendicular to the surface mainly induces tensile stress, while a change of the distance in a direction parallel to the surface primarily models shear stress.

Changing the distances can either be done in a continuous way, simulating the whole molecular dynamics of the system, or stepwise with intermediate relaxations. The first option offers the inclusion of temperature effects. However, it also requires very fast deformation speeds in the range of at least a few $\mathrm{cm\,s^{-1}}$, since the total simulation time is limited due to the computational costs. The hybrid materials studied in this thesis display a hysteresis in the stress-versus-strain curves in experiments [18], which indicates the presence of viscoelasticity. Accordingly, large deformation speeds would overestimate the Young's modulus[1] of the interface [22]. Therefore, in this work the second option was chosen, where the distances are changed stepwise with intermediate relaxations. If the steps are small enough, this method is equivalent to an infinitely slow deformation speed [163], also called quasi-static approximation, and provides an accurate estimate of the Young's modulus as well as an upper limit for the strength of the interface at 0 K. At higher temperature, the Young's modulus and strength usually decrease, since the average bond lengths increase due to thermal fluctuations, and energy barriers for bond breaking can be overcome by thermal activation.

In order to obtain reliable mechanical properties, it is important to start the mechanical tests from the equilibrium state, i.e. the force-free interface configuration with minimum energy. Therefore, the positions of the fixed layers relative to each other are optimised beforehand with a conjugate gradient algorithm, which was implemented in a python script for this thesis. The opti-

---

[1] The *Young's modulus* or *elastic modulus* describes the geometry independent stiffness of a material under uniaxial strain. It is determined from the slope of the stress-versus-strain curve at low strain.

misation procedure works similar to the already described mechanical testing, but instead of displacing the layers to simulate a force, the displacement is changed to minimise the forces acting on the atoms in the fixed layers. As a first step, the displacement is changed along the direction of the current forces to find the minimum in this direction. Then, the next search direction is calculated from the current forces, the forces of the last step, and the former search direction. Thereby, the conjugate gradient algorithm uses information from former steps, which can speed up convergence significantly.

Checking convergence

Apart from these design-related factors that mostly consider the physical accuracy of the model, the numerical accuracy of the calculated properties should also be evaluated. As previously mentioned, the results can be converged to the infinitely slow deformation limit with respect to the step size. Furthermore, the convergence settings for the calculated forces during the structural relaxation in each deformation step will also affect the accuracy of the resulting mechanical properties. Finally, the number of surface layers that are allowed to relax could affect the results as well. However, testing the convergence with respect to the number of relaxed surface layers is very expensive. As the next section will demonstrate, first mechanical tests on anatase-TiO_2/carboxylic-acid interfaces indicate that the number of layers needed to converge the calculated adsorption and surface energies is also enough to converge the mechanical properties. In both cases, only a few outer layers exhibit significant relaxations away from their bulk positions. Therefore, the convergence with respect to the number of relaxed surface layers is not studied further in this work.

Convergence of the mechanical properties with respect to the step size and the force convergence settings is tested on single molecules in a sufficiently large simulation cell. The detailed outcomes of these tests are presented in Appendix B.2. According to the results, the step size should be 0.1 Å or lower, comparable with other COGEF-studies [164–167]. Otherwise, the strength and maximum strain of the molecule are underestimated in the calculation. The accuracy of the calculated forces is less important for typical convergence settings of DFT calculations (usually $0.01\,\mathrm{eV}\,\text{Å}^{-1}$ or less). However, it should be noted that the force convergence also influences how accurately the equilibrium state to start from can be found, and how accurate derived properties, such as elastic constants, can be calculated. Therefore, it is recommended to obtain forces with an accuracy of $0.005\,\mathrm{eV}\,\text{Å}^{-1}$ or better. The force convergence setting is also used to detect a failure of the interface. A significant drop of the force between two displacement steps indicates that the interface is broken. The drop is only considered to be significant, if it is larger than two times the force convergence setting, because otherwise it might be caused by the lack of convergence.

6.2 Virtual mechanical tests of anatase-TiO_2/carboxylic-acid interfaces

After establishing the modelling parameters, the aforementioned setup can be put into practice to simulate the mechanical properties of hybrid interfaces. As a first example of the many interfaces that are of interest for the hybrid materials that motivated this thesis, the combination of anatase TiO_2 with carboxylic acids is chosen. This combination is particularly interesting in light of the results in Chapter 5: The synthesis of anatase TiO_2 nanoparticles allows to control the shape and hence, the dominating surface structure. Therefore, understanding how the surface structure affects the mechanical properties of the interface can directly be used to improve this class of hybrid materials. As in Chapter 5, the three major facets $\{101\}$, $\{100\}$, and $\{001\}$ are studied here, corresponding to bi-pyramidal, rod-like, and platelet-shaped nanoparticles, respectively.

Apart from the influence of the underlying surface, the binding mode of the carboxylic acid is also studied in this section. On anatase TiO_2, carboxylic acids bind to the surface either through a bi-dentate (bd) bridging configuration or through a quasi-bi-dentate (qbd) configuration, where the hydrogen of the carboxyl group binds to a surface oxygen (see Figure 6.3). While the bi-dentate bridging adsorption mode is usually stronger, the quasi-bi-dentate mode takes up less space on the surface, which allows for a higher coverage. In order to separate coverage effects from the effect of the binding mode itself, however, the same coverage is chosen for both adsorption modes in this study. The third configuration shown in Figure 6.3 also binds to the surface in a quasi-bi-dentate geometry, but two hydrogen atoms in the hydro-carbon chain are removed so that a C=C double bond is formed. This alters the structure and stiffness of the molecule. Hence, comparison of the quasi-bi-dentate structures with and without the C=C double bond allows to evaluate which part of the molecule contributes most to the overall properties of the interface.

All calculations in this section are performed with the exchange-correlation (xc) functional by J. Perdew, K. Burke, and M. Ernzerhof (PBE) [30]. As mentioned in Chapter 2, van-der-Waals interactions are not represented correctly within this xc density functional. Trying to include van-der-Waals interactions with the method employed in Chapter 5, however, resulted in convergence issues in several test calculations. For the systems studied here, the contribution of van-der-Waals interactions is expected to be low, since the distance between the molecules is relatively large. Studying systems with higher coverage or molecules that are not cross-linked, though, would necessitate the use of exchange-correlation functionals, which include van-der-Waals interactions. In those cases, different implementations, such as the method by Langreth and Lundqvist [168], the Tkatchenko-Scheffler method [169] or the Grimme-correction [170, 171], may be employed to circumvent the aforementioned convergence issues. The remaining computational settings are detailed in Appendix A.

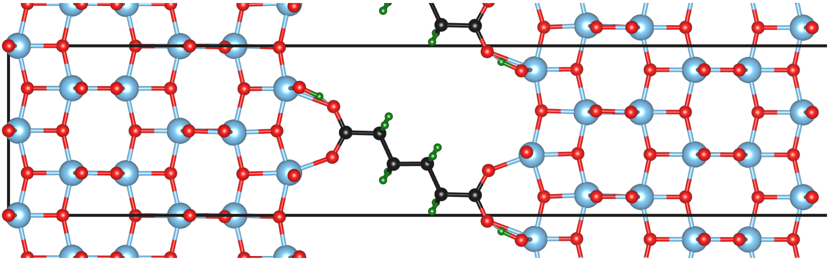

(a) bi-dentate (bd) binding mode

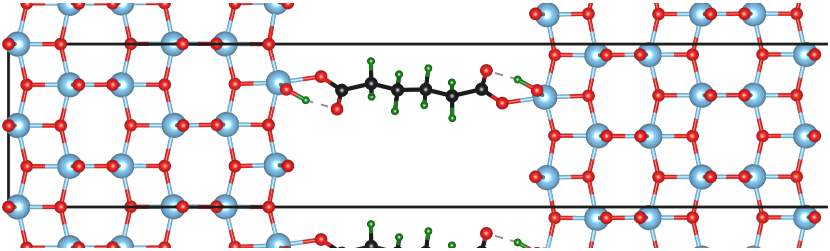

(b) quasi-bi-dentate (qbd) binding mode

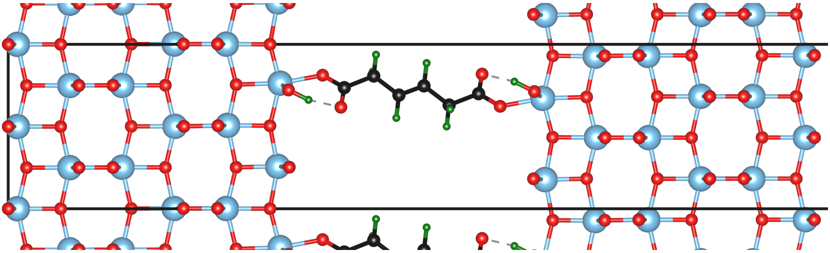

(c) qbd binding mode with a double bond between the third and fourth carbon atom

Figure 6.3: Different binding modes of carboxylic acids on anatase TiO_2 studied in this chapter, illustrated for the {001} facet (see Appendix D for other facets). Colour code: Ti – blue, O – red, C – black, H – green.

Elastic energy and failure mechanisms

The calculated energy-versus-displacement curves for all resulting nine combinations of the three surface structures with the three binding modes are displayed in Figure 6.4. All curves have a parabolic shape indicating a predominantly elastic deformation of the interfaces. Another interesting feature is the maximum energy in the tensile region. A simple but common hypothesis would be to assume that the elastic energy at interface failure corresponds to the binding energy of the molecule on the surface. As was shown in Chapter 5, Table 5.4, the binding energies of carboxylic acids on anatase TiO_2 surfaces are typically in the range of 1.5 eV to 2.3 eV. Apparently, the failure energies observed here are much lower for many interface combinations. To understand the discrepancy, a closer look at the failure mechanisms is needed.

A failure mechanism, which is triggered at an energy that should – in theory – correspond to the binding energy, is the simple detachment of the molecule from the surface. However, a detachment of the molecule is only observed for the interfaces containing the {100} facet (see example in Figure 6.5a and Appendix D). Even there, the failure energy is lower than the binding energy, which might be due to the fact that the surface and the molecules are not separated infinitely, but are still bound weakly by long range interactions. The other interfaces break through a surface failure mechanism, meaning that the titanium atom to which the molecule is bound detaches from the surface (see

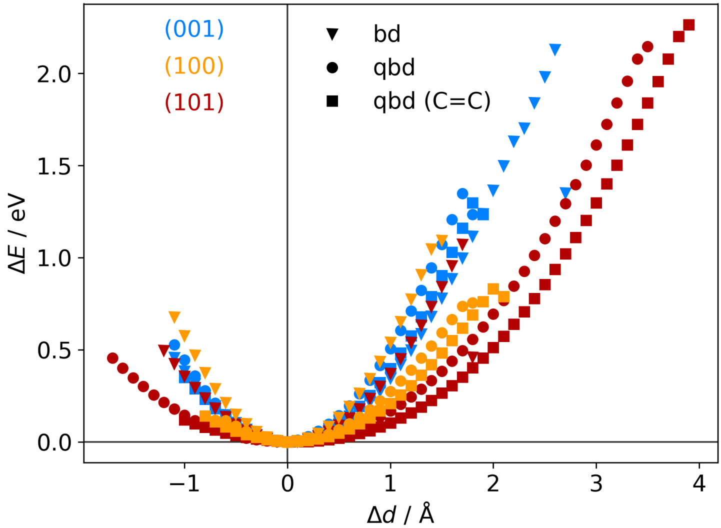

Figure 6.4: Calculated energy change ΔE depending on the displacement of the upper fixed layers Δd for different anatase-TiO_2/carboxylic-acid interfaces. Colours indicate facets: {101} facet – red, {100} facet – orange, {001} facet – blue. Symbols indicate binding modes: bi-dentate bridging mode – triangles, quasi-bi-dentate mode without a C=C double bond – circles, quasi-bi-dentate mode with a C=C double bond – squares.

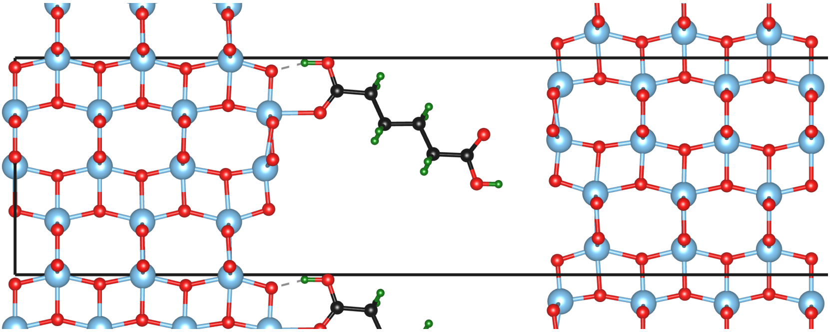

(a) detachment failure mechanism (qbd at {100})

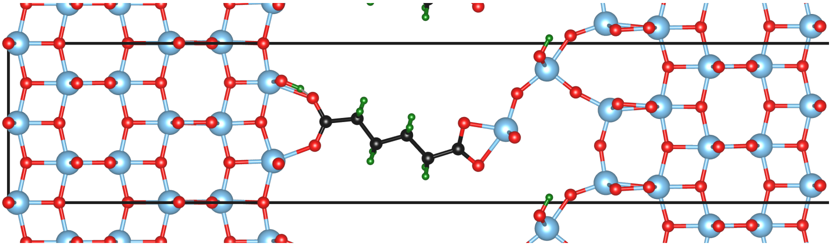

(b) surface failure mechanism (bd at {001})

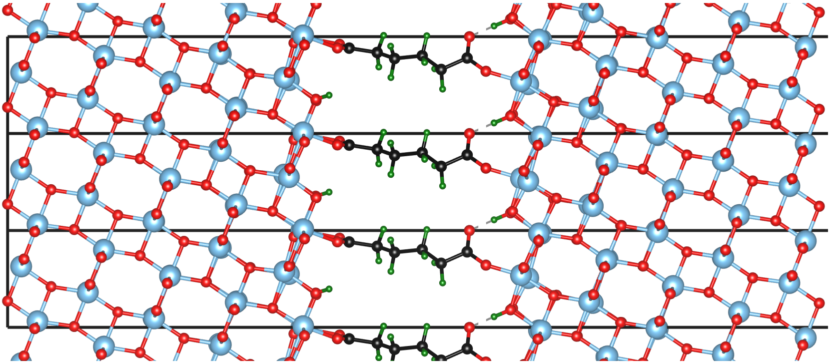

(c) stress release by changing from bi-dentate to quasi-bi-dentate binding (at {101})

Figure 6.5: Final calculated structures of three interface models after failure, exemplifying the different failure mechanisms of anatase-TiO_2/carboxylic-acid interfaces. Note that the unit cell for modelling the bi-dentate adsorption mode on the {101} facet is not orthogonal, which is why more black lines and molecules appear in that image even though the number of molecules per surface area is similar to the other structures. Colour code: Ti – blue, O – red, C – black, H – green.

example in Figure 6.5b and Appendix D). In the process, surrounding oxygen atoms from the surface can also detach. For the most extreme case of this failure mechanism, observed in the interface of the {001} facet with a carboxylic acid bound through a bi-dentate bridging configuration shown in Figure 6.5b, a whole TiO_2-unit detaches from the slab, which then seems to form a reconstruction. A third failure mechanism appears for the interface of the {101} facet with a carboxylic acid bound through a bi-dentate bridging configuration. There, only one of the bonds to the surface breaks and the carboxyl group rearranges to form a quasi-bi-dentate binding (see Figure 6.5c). It can be assumed that the final failure of the interface then follows the mechanism for the quasi-bi-dentate binding mode on this facet. All the final calculated structures after the interfaces failed are depicted in Appendix D for the interested reader, and all virtual tensile tests were animated in short movies, which can be watched in the online supporting material[2].

Calculated mechanical properties

The differences between the interfaces and binding modes with respect to the mechanical properties become much more obvious from analysing the forces displayed in Figure 6.6 than from analysing the energies. The stiffness of the interface is independent of the underlying surface for a bi-dentate bridging binding configuration (triangles in Figure 6.6). Only the breaking force differs for the different facets for this binding mode. Additionally, the molecular structure further away from the surface does not seem to influence the mechanical properties, because the results of the quasi-bi-dentate configurations with a double bond (squares in Figure 6.6) are virtually the same as for the quasi-bi-dentate configurations without a double bond (circles in Figure 6.6). On the {001} facet, the interfaces with a quasi-bi-dentate binding are calculated to be slightly stiffer than the interface with bi-dentate bridging binding, while on the {101} and {100} facets the quasi-bi-dentate structures are significantly less stiff than the bi-dentate bridging structures.

A true comparison of different interfaces, independent of the respective surface areas and initial interface widths, can only be achieved through stress-versus-strain diagrams as shown in Figure 6.7. These diagrams also allow to calculate the elasticity of the interface described by the Young's modulus, as well as the strength and maximum strain of the interface. Here, the Young's modulus is determined from the slope of a linear fit at strains lower than 0.05, and the resulting mechanical properties are listed in Table 6.1. Evidently, the stress-versus-strain diagram looks very similar to the force-versus-displacement diagram, due to the fact that the surface areas and interface widths of different facets are also similar. Therefore, most observations made for the stiffness can directly be transferred to the Young's modulus: Interfaces built with the {001} facet have the highest moduli, and the modulus is independent of whether or not the molecule contains a C=C double bond in

---

[2] Visit `https://doi.org/10.15480/336.3408` for obtaining the online supporting material. The link can also be accessed by scanning the QR code at the beginning of Appendix D.

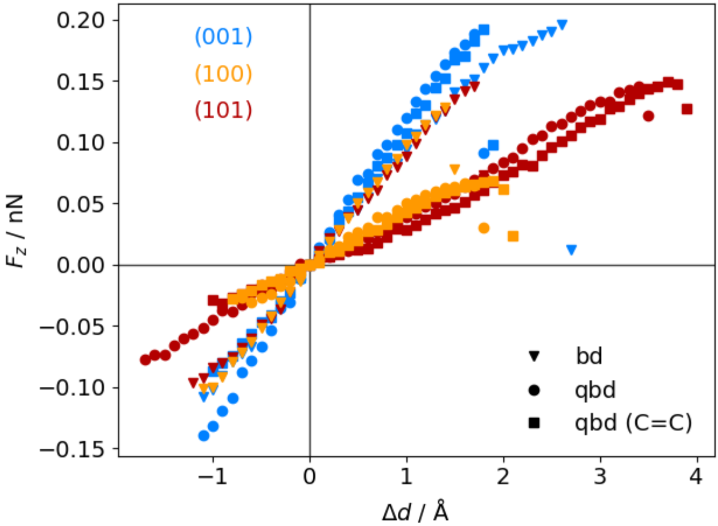

Figure 6.6: Calculated forces F_z on different anatase-TiO$_2$/carboxylic-acid interfaces stretched (+) and compressed (-) perpendicular to the interface by displacing the upper fixed layers by Δd. Colours indicate facets: {101} facet – red, {100} facet – orange, {001} facet – blue. Symbols indicate binding modes: bi-dentate bridging mode – triangles, quasi-bi-dentate mode without a C=C double bond – circles, quasi-bi-dentate mode with a C=C double bond – squares.

the middle. Furthermore, interfaces bound through quasi-bi-dentate configurations have lower Young's moduli than interfaces bound through bi-dentate bridging configurations on {101} and {100} facets, which is in contrast to the result for interfaces with {001} facets. Aside from that, the stress-versus-strain diagram also reveals a clear hierarchy among the different facets with respect to their Young's moduli. Comparing interfaces with the same binding mode, the Young's modulus is always highest for the {001} facet and lowest for the {101} facet.

The tensile strength describes the maximum stress of the interface before it fails. Interfaces built with the {100} facet fail through desorption of the molecule, as can be seen in Figure 6.5. Their tensile strength depends on the binding mode. The quasi-bi-dentate configurations have the lowest tensile strength of the interfaces studied here (around 180 MPa), while the bi-dentate bridging configuration ($\sigma_{max} \approx 350$ MPa) approximately reaches the values obtained for the interfaces built with the {101} facet. As aforementioned,

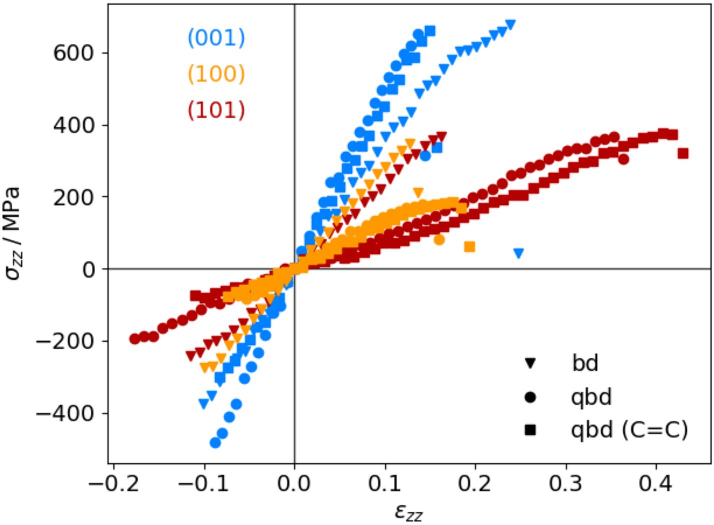

Figure 6.7: Calculated tensile (+) and compressive (-) stress (σ_{zz}) for different anatase-TiO_2/carboxylic-acid interfaces strained perpendicular to the interface (ε_{zz}). Colours indicate facets: {101} facet – red, {100} facet – orange, {001} facet – blue. Symbols indicate binding modes: bi-dentate bridging mode – triangles, quasi-bi-dentate mode without a C=C double bond – circles, quasi-bi-dentate mode with a C=C double bond – squares.

Table 6.1: Calculated tensile strengths (σ_{max} in MPa), maximum tensile strains (ε_{max}), and Young's moduli ($E_{\text{tensile/compressive}}$ in GPa) for interfaces built from different anatase TiO_2 facets connected by a carboxylic acid through different binding modes. A two-sided 95 % confidence interval resulting from the linear fit is given for the Young's moduli.

facet	binding mode	σ_{max}	ε_{max}	E_{tensile}	$E_{\text{compressive}}$
{101}	bi-dentate (bd)	366.6	0.172	2.35 ± 0.29	2.76 ± 0.46
	quasi-bd (qbd)	366.4	0.364	0.78 ± 0.49	1.27 ± 0.73
	qbd - double bond	375.6	0.429	0.72 ± 0.32	1.02 ± 0.14
{100}	bi-dentate (bd)	346.7	0.137	2.92 ± 0.19	3.03 ± 0.22
	quasi-bd (qbd)	179.0	0.160	1.66 ± 0.17	1.68 ± 0.22
	qbd - double bond	185.3	0.193	1.22 ± 0.25	1.03 ± 0.23
{001}	bi-dentate (bd)	676.5	0.247	3.66 ± 0.62	3.78 ± 0.73
	quasi-bd (qbd)	650.6	0.145	5.54 ± 0.46	5.68 ± 0.45
	qbd - double bond	662.3	0.157	4.74 ± 0.31	3.91 ± 0.48

interfaces built with the {101} facet fail through a surface failure mechanism, and the bi-dentate bridging binding mode converts into a quasi-bi-dentate binding mode, when a critical strain is reached. The tensile strength of this facet, however, does not depend on the binding mode (all around 370 MPa), which is particularly interesting for deformation induced stresses. In this case, the conversion of the bi-dentate binding to a quasi-bi-dentate binding can release stress in the material at the critical deformation without inducing terminal failure, and permitting further deformation. Moreover, one can hypothesise, that a heat treatment could release some stress in the material and recover the stronger bi-dentate binding. Interfaces built with the {001} facet do not only have the highest Young's moduli, but also the highest tensile strengths (above 650 MPa). As for the {101} facet, the binding mode on this facet has only a minor influence on the tensile strength.

It has to be noted, though, that the coverage dependence is not studied here. While the bi-dentate bridging geometries already cover all possible adsorption sites, the quasi-bi-dentate configurations only occupy half of the sites. On {001} facets, quasi-bi-dentate binding geometries are usually not stable at higher coverage for larger molecules, while on {101} and {100} facets quasi-bi-dentate structures can be stable at higher coverage, which would strengthen the interface. Nevertheless, a full coverage would increase the Young's modulus at most by a factor of two compared to the half coverage studied here. Therefore, it can be concluded that in general, the {001} facet forms the interfaces with the highest Young's modulus.

Compressive and shear stresses

So far, the discussion focussed on the tensile part in Figure 6.7, but the interfaces were also studied under compression in the elastic regime. As can be seen from Table 6.1, the Young's moduli in the tensile and compressive regime are the same within the uncertainty range of the fits. Therefore, it is possible to model the elastic response of the different interfaces using a harmonic approximation (Hooke's law) in larger scale continuum models. A closer look at the uncertainty of the fit reveals, that the relative uncertainties are quite large due to the low number of points in the linear fit. To increase the accuracy of the fit – and hence, the predicted Young's modulus – a smaller step size could be used in the low strain regime to create more points for the linear approximation. This would, however, also increase the computational costs.

The displacement along the z-axis does not only lead to tensile or compressive stress σ_{zz}, but also to shear stresses perpendicular to that axis (σ_{xz} and σ_{yz}). Figure 6.8 shows the ratio of the tensile or compressive stress to the total stress. A value of one means that there is no shear stress, while a value of zero would indicate pure shear stress. For many interfaces, the ratio is low for small deformations, due to the forces that remain after relaxation, as set by the convergence criteria. At larger deformations, the stress is mainly along the deformation direction as expected. Interfaces with the {001} facet show particularly low shear stress, while interfaces built with the {101} facet and quasi-bi-dentate binding exhibit up to 10 % of shear stress. The difference

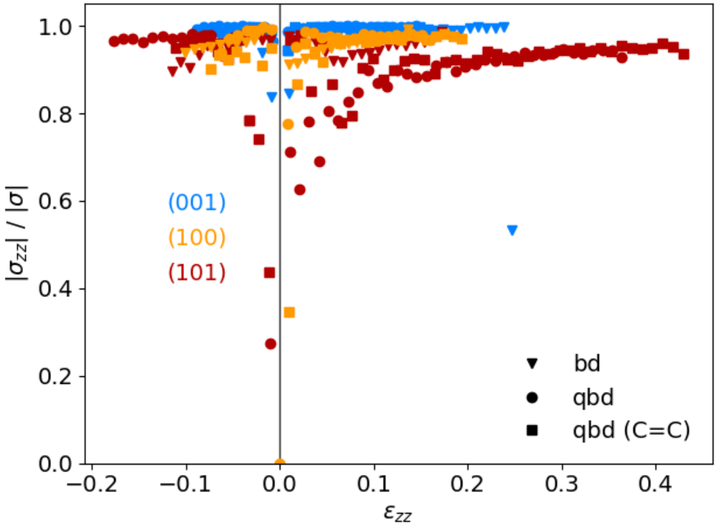

Figure 6.8: Ratio of the calculated stress along the displacement direction σ_{zz} to the total stress $|\sigma| = \sqrt{\sigma_{xz}^2 + \sigma_{yz}^2 + \sigma_{zz}^2}$ depending on the strain ε_{zz}. Values close to one correspond to pure tensile or compressive stress, while values close to zero correspond to pure shear stress. Colours indicate facets: {101} facet – red, {100} facet – orange, {001} facet – blue. Symbols indicate binding modes: bi-dentate bridging mode – triangles, quasi-bi-dentate mode without a C=C double bond – circles, quasi-bi-dentate mode with a C=C double bond – squares.

can be directly attributed to the surface structure. The bond between the carboxylic acid and the surface is approximately oriented along the surface normal on the (001) surface, due to the flat surface structure. The (101) surface, on the other hand, has a sawtooth structure. Therefore, the carboxylic acid binds to the surface on an angle, and shear stress is induced when the molecule is pulled along the surface normal.

Apart from the larger shear stress, the angle between the molecule and the surface normal also causes the molecule to rotate during the deformation. Since the forces to invoke a rotation are lower than for stretching the molecule, this may be the cause for the low elastic modulus of the interfaces based on the {101} facets. Therefore, further cross-linking of molecules or the formation of a covalently bonded network in between the particles, as illustrated in Figure 6.1b, is expected to greatly improve the mechanical properties for these interfaces.

Comparison with experimental data

The elasticity of membranes made from anatase TiO_2 nanoparticles in different shapes linked by carboxylic acids was studied experimentally by colleagues from the Department of Physical Chemistry at the University of Hamburg [18]. As described in Chapter 5, the different shapes are connected to the predominantly exposed facet. Qualitatively, their results agree well with the calculated results presented here. Membranes with platelet shaped nanoparticles dominated by $\{001\}$ facets are found to have the largest Young's modulus of (7.21 ± 1.04) GPa. For membranes with rod-shaped particles exposing mainly $\{100\}$ facets, a Young's modulus of (5.22 ± 0.39) GPa was observed, while for dot-shaped particles, which are expected to show mainly $\{101\}$ facets, the lowest modulus of (2.57 ± 0.18) GPa was reported. Evidently, the calculated trend of $E_{\text{tensile}}(\{101\}) < E_{\text{tensile}}(\{100\}) < E_{\text{tensile}}(\{001\})$ for ideally flat interfaces translates directly into the same trend in hybrid materials that are linked through the corresponding facets. Even though the measured Young's moduli are larger than the computed values presented here, they have the same order of magnitude. As observed in natural hybrid materials, the structure of the hybrid material enhances the mechanical properties to values larger than the ideal flat surface limit.

Concluding remarks

In this chapter, the mechanical properties of hybrid interfaces were simulated on the atomic scale with ab-initio methods. First, the set-up for these virtual mechanical tests was described, and important parameters were discussed. The resulting virtual mechanical testing device uses a sandwich structured slab model (oxide – organic – oxide) for the interface, where the outer layers are fixed in their bulk positions. The force is then applied by displacing the fixed layers in small steps (COGEF approach). A small step size of 0.1 Å was found to yield reliable results within the quasi-static approximation, but even smaller step sizes might be needed in the small deformation region to improve the accuracy of calculated elastic properties. The most important advantages of the set-up are, that implementation and transfer to other systems is very easy, and that the viscoelastic properties of the interface can be neglected. Furthermore, the inclusion of the calculated properties in larger scale continuum mechanics models is straightforward.

In the second part of the chapter, the virtual mechanical testing device was applied to calculate the mechanical properties of hybrid interfaces made from anatase TiO_2 surfaces and carboxylic acids. Interfaces built with the $\{001\}$ facet were found to have the highest Young's modulus, followed by the $\{100\}$ and the $\{101\}$ facets. The computed order of Young's moduli is verified by experimental results for membranes made from TiO_2 nanoparticles with different shapes, linked by carboxylic acids. The $\{001\}$ facets also form the interfaces with the highest tensile strength, with the {101} and {100} facets in second and third place, respectively. Interestingly, the expected failure mechanism through a desorption of the carboxylic acid was only observed for the {100} facets. The other interfaces broke through a titanium atom that was ripped from the surface. On the {101} facet, stress can be released by changing from a bi-dentate bridging binding mode to a quasi-bi-dentate binding mode, which is expected to be a reversible process. In conclusion, the interface failure is not only determined by the binding energy between molecule and surface, but also by the cohesive energy within the surface, as well as by the failure mechanism. This finding underlines the need for quantum mechanical calculations in order to accurately predict these quantities. Furthermore, combining the results summarised above directly yields two optimisation strategies for hybrid materials made from anatase TiO_2 nanoparticles and carboxylic acids: If the Young's modulus and strength of the final material should be as high as possible, platelet-shaped particles with a high amount of {001} facets should be used. If the ability to anneal the material after plastic deformation is desired, bi-pyramidal particles with a high amount of {101} facets are preferable.

As a next step, the calculated properties can be inserted in continuum models to enable a quantitative comparison with experimental results. Working examples of multi-scale simulations that integrate all scales from single atoms to the macroscopic material are scarce as of yet, which makes a study such as this also interesting from a methodological point of view. When quantitative prediction of the mechanical properties is achieved, different material combinations can be screened to improve the properties of the final hybrid material. Furthermore, the results presented here impact the modelling of hybrid interfaces with classical molecular mechanics, which are usually not able to predict the breaking of bonds with sufficient accuracy. Therefore, it is important to know the failure mechanism as well as the rupture energies and forces beforehand, so that they can be included in the model.

7

Conclusion

The aim of this work was to deepen the understanding of hybrid materials made from transition-metal-oxide nanoparticles and organic acid linkers, by studying their interfaces with the help of density-functional theory (DFT) calculations. In particular, interfaces of carboxylic acids with magnetite (Fe_3O_4) and anatase titanium dioxide (TiO_2) were examined, motivated by their diverse fields of application ranging from catalysis and biomedical treatments to cosmetic products and the aforementioned hybrid materials. Due to the huge surface-to-volume ratio of nanoparticles, the hybrid interfaces formed by the nanoparticles with their surroundings become a decisive factor for the performance of catalysts and hybrid materials.

An important step for understanding such hybrid interfaces is to gain insight into how the molecules bind to different surfaces. Configurations with the lowest total energy, i.e. the highest binding energy, are thermodynamically most favourable, and hence, a good first approximation for the real structure of the interface. Simply creating seemingly reasonable structures based off chemical intuition often fails to find these minimum-energy configurations or misses important configurations with similar energy. On the other hand, creating a lot of structures and calculating all of their energies to sample the configuration space exhaustively, is computationally expensive. Therefore, a software for Configuration space determination and Reduction (`CodeRed`) was designed and built in this work. The software creates configurations based on the existing knowledge about the adsorption structure. Then, the amount of structures needed to sample this configuration space is reduced with the help of similarity metrics and unsupervised machine learning (ML) selection methods. The adsorption structures that can be built with `CodeRed` are not limited in any way. An arbitrary number of atoms can be added stepwise to the structure, and parts of the molecule that are not expected to change upon adsorption can be added after the configuration space sampling steps. Furthermore, the users are free to choose their own favoured similarity metric and ML selection algorithm, even though `CodeRed` already offers some preconfigured methods. `CodeRed` is devised as an open-source software written in python. Therefore, it can be easily included in other python packages, and has the potential to evolve further through input from the atomistic simulations community. Since python is a powerful scripting language, the writing of `CodeRed`-scripts is also straightforward for python-users. In summary, `CodeRed` is a user-friendly python package that combines chemical intuition with unbiased state-of-the-art ML techniques to sample the configuration space of arbitrary interfaces exhaustively, but with reduced computational cost compared to pre-existing techniques.

Apart from the methodological development, this thesis also contributed significantly to the understanding of interfaces between magnetite (Fe_3O_4) and formic acid (HCOOH). In the aforementioned applications, mainly the {001} and {111} facets of magnetite nanoparticles determine the overall performance. The structure of the {001} facet is known to convert to a higher symmetry structure upon adsorption of formic acid. By analysing the thermodynamics of different binding configurations and underlying surface structures, and combining the results with experimental data from colleagues at DESY Hamburg, this surface restructuring was explained in this thesis, and published in source [97]. Near surface iron diffusion fills the sub-surface iron vacancies, which results in the aforementioned high symmetry structure. This can also be understood in terms of a preference for bulk iron vacancies over near-surface iron vacancies, due to the acid on the surface. Furthermore, these studies confirmed the dissociation of formic acid on the (001) surface of magnetite, and revealed preferable adsorption sites for the formate and dissociated hydrogen. On the {111} facet, a thorough adsorption structure search provided further insights into the dissociation of formic acid upon adsorption. The dissociated hydrogen atom was found to adsorb favourably on an oxygen terminated surface, leading to a stabilisation of iron vacancies on the surface. Interestingly, two different binding modes – chelating and quasi-bi-dentate – are equally stable on this facet. Comparison of calculated vibrational spectra with measured infra-red absorption spectra, confirmed the observation of both binding modes, under the given experimental conditions. Additionally, the calculated binding configurations on both facets agree with results from surface x-ray diffraction and scanning tunnelling microscopy, which were obtained by collaborators from DESY Hamburg [98].

The knowledge of the most favourable adsorption modes gained in this thesis provides a solid foundation for future studies on the interaction of carboxylic acids with magnetite surfaces. For example, one could study the reaction kinetics in water-gas-shift reactions or Fischer-Tropsch synthesis routes, where formic acid is an important intermediate and magnetite is a successful catalyst, even though the exact catalytic mechanisms are not yet fully understood. Considering formic acid as a representative of the whole carboxylic acid family, the results presented here also contribute to a multi-scale modelling approach for interfaces made from carboxylic acids and magnetite. Classical force-fields for molecular dynamics calculations often fail to accurately predict chemical reactions, such as the dissociation of acids on a surface. Hence, the more precise results on the dissociation of carboxylic acids presented here aid the development of more accurate models. In fact, a new classical force-field based on the adsorption structures and charge distributions calculated in this thesis, has already been developed in a collaboration with the molecular modelling group at TUHH. The new force field was not only able to model the dynamics of formic acid on magnetite, but also predicted the interface structures for water and larger carboxylic acids on magnetite with high accuracy [143]. In this regard, future DFT studies can help to refine the force field, and predict reaction energies of interlinking processes in hybrid materials through a combined quantum-mechanics / molecular-modelling (QM/MM) approach.

The performance of hybrid materials and nano-catalysts is not only influenced by their binding to molecules, but also by the shape of the nanoparticles. Therefore, the shape-controlling effects of hydrohalic (HX, where $X = F, Cl, Br, I$) and carboxylic ($R-COOH$) acids in the synthesis of titania (TiO_2) nanoparticles were investigated in this thesis, and published in source [147]. In the case of the heavier hydrohalic acids, this work was the first to study their adsorption and the substitution of surface hydroxyl groups on titania surfaces. Combined with thermodynamic models, this thorough study was able to find a new explanation for the stabilisation of rod- and cube-shaped particles in solutions containing HCl. At high chloride concentrations, the substitution of surface hydroxyl groups by chloride becomes energetically favourable, which stabilises the $\{100\}$ facet. For a synthesis in hydrofluoric acid containing solutions, the already known preference for platelet-shaped particles was confirmed, while for the heavier halides – bromine and iodine – a preference for bi-pyramidal particles was found. In practice, the adsorption process of hydrohalic and carboxylic acids is competitive, since both acid families bind to the same adsorption sites. The comparison of binding energies and thermodynamic stabilities of different interfaces predicted that the carboxylic acids are able to replace hydrohalic acids on the surface of titania nanoparticles. However, fluoride anions are an exception to this rule, because they are calculated to have a higher tendency to replace an oxygen atom from the titania surface. Thereby, the calculations explain why fluoride is found in the nanoparticle composites experimentally, even after several washing steps. Furthermore, the predicted particle shapes match the ones observed in titania nanoparticle syntheses using different halide precursors, as performed by collaborators from the physical chemistry department at the University of Hamburg. Combining the shape predictions with the half-automated adsorption structure search by `CodeRed` paves the way for a systematic computational search for shape-controlling agents. With reliable shape predictions at hand, experiments on these agents can be limited to a small number of promising candidates. In light of the results presented here, another topic of interest for future studies may be the facet-selectivity of adsorption processes. Finding agents that only adsorb to one of the available facets would allow to link and assemble particles in a preferred orientation, which would increase the design-space for hybrid materials drastically.

Finally, the mechanical properties of hybrid interfaces made from titania and carboxylic acids were investigated with the help of DFT calculations in this thesis. Analysing different facets and binding modes, proved that the contact between molecule and surface determines the overall mechanical properties of the interface. Changes in the molecular structure further away from the surface only have a minor impact on the mechanical properties of the interface. However, the failure of the interface is not always caused by a simple de-bonding of the molecule, but also by atoms that are excavated from the surface. Therefore, the adsorption energies alone cannot be used as an indicator for the mechanical strength, and further quantities, such as the cohesive energy and defect formation energies, have to be taken into account. Interfaces formed with the {001} facet were predicted to have the highest elastic modulus and strength, making hybrid materials with platelet shaped particles the most promising in this regard. Considering the approximations that had to be made in order to be able to perform the calculations, the calculated elastic moduli agree surprisingly well with experimental results for titania nanoparticles with different shapes, as measured by collaborators from the University of Hamburg. Nevertheless, more accurate quantitative predictions can most likely be obtained by employing the results from this thesis in larger scale methods, which model the real microstructure of the hybrid materials. First steps in this direction have already been taken by collaborators from the Helmholtz Centre Geesthacht (HZG), who include the elastic modulus and the interface strength predicted by DFT in their continuum mechanics models. Future studies may also focus on the influences of coverage and the length of the molecules in the interface, as well as their interconnectivity, on the mechanical properties. The computational setup created in this thesis can, in principle, be transferred to any interface of interest.

In summary, this thesis advances the understanding of interfaces between transition metal oxides and carboxylic acids by finding relevant adsorption structures, explaining shape-controlling effects, and simulating the mechanical responses of exemplary systems. Thereby, this work contributes to the development of novel catalysts for a sustainable production of fuels and bio-inspired hybrid materials with exceptional mechanical properties. Collaborations with partners from DESY and the University of Hamburg allowed to validate the computational results experimentally, as well as to include the knowledge from measurements in the interface models. Furthermore, the computational tools developed in this thesis simplify the transition to other systems of interest, which will potentially accelerate the search for improved materials in the future. First steps have already been taken towards resolving the big computational challenge of true multi-scale simulations of hybrid materials. The results presented in this thesis allow comparison with and integration in modelling methods on different length scales, which is an ongoing work in progress in collaboration with groups from the Helmholtz Centre Geesthacht and the Hamburg University of Technology. Interesting research can be expected in the future, when quantum, molecular, and continuum mechanics are interlinked to model and predict the properties of hybrid materials.

Appendices

A Computational details

In this Appendix the detailed computational settings of the different calculations presented in this thesis are documented. Most parameters are provided with the tag that is used in VASP to set this parameter. A short description of the meaning of the different tags is also given, but more detailed information on the settings tags can be found in the VASP manual at `https://www.vasp.at/wiki/index.php/The_VASP_Manual`.

A.1 Settings for magnetite/carboxylic-acid interfaces

The extensive study of interfaces between magnetite nanoparticle surfaces and formic acid presented in Chapter 4 necessitated different computational strategies depending on the system at hand. Nevertheless, all calculations make use of the pseudopotential method, which allows to only treat the outer (valence) electrons explicitly. The outer 8, 6, 4, and 1 electrons of Fe, O, C, and H, respectively, are considered to be valence electrons in this work. Furthermore, all calculations presented in Chapter 4 are performed with the PBE [30] XC-functional. A Hubbard correction [35] in the description of Dudarev *et al.* [172] is applied to the d-orbitals of iron with $U_{\text{eff}} = 4.0\,\text{eV}$. A comparison with other functionals can be found in Appendix C.

For the reference calculations on bulk magnetite a single relaxation run, where all atomic positions are optimised, and a following static calculation were enough to reach the ground state of the system. The two steps, relaxation and static calculation, are performed for several lattice constants, in order to find the equilibrium lattice constant. The k-points for integration in reciprocal space were generated based on a $11 \times 11 \times 11$ grid for the cubic unit cell. The remaining settings of the two computational steps (relax, static) are listed in Table A.1.

Reaching the ground state is more complex for magnetite surfaces due to their non-stoichiometry, the anti-ferromagnetic coupling between tetrahedral and octahedral iron sites, and the charge redistribution close to the surface. Therefore, a four-step process is employed: First, the system is pre-converged in a static calculation to obtain a more reasonable starting electron density for the following run. Second, the atomic positions are optimised in a relaxation run. Third, the atomic positions are refined in another relaxation run with a

Table A.1: Computational settings for the calculation of the properties of bulk magnetite in Chapter 4 with VASP. M_{tet} is the number of iron atoms in tetrahedral sites, M_{oct} is the number of iron atoms in octahedral sites, and M_{rem} is the number of remaining atoms.

Setting	Step	Value	Description
`GGA`	all	PE	select PBE XC-functional
`LDAU`	all	.TRUE.	settings for Hubbard correction
`LDAUTYPE`	all	2	
`LDAUL`	all	2 -1	
`LDAUU`	all	4.0 0.0	
`LDAUJ`	all	0.0 0.0	
`LDAUPRINT`	all	0	
`LASPH`	all	.TRUE.	aspherical contributions
`LMAXMIX`	all	4	include d-orbitals in density mixer
`ISPIN`	all	2	spin polarised calculation
`LORBIT`	all	11	calculate local magnetic moments
`MAGMOM`	all	M_{tet}*-5.0 M_{oct}*5.0 M_{rem}*0.0	initialise magnetic moments for anti-ferromagnetic coupling
`ENCUT`	all	520	cut-off energy (in eV)
`PREC`	all	Accurate	precision setting
`LREAL`	all	Auto	real-space projection
`ISMEAR`	relax	0	gaussian smearing
	static	-5	no smearing (tetrahedron method with Blöchl corrections)
`SIGMA`	relax	0.02	width for gaussian smearing
`IBRION`	relax	2	relax with conjugate gradient algorithm
	static	-1	no relaxation
`ISIF`	all	2	relax atomic positions, but not unit cell
`NSW`	relax	500	maximum number of relaxation steps
	static	0	
`NELMIN`	all	4	minimum number of electronic steps
`NELM`	all	80	maximum number of electronic steps
`EDIFF`	relax	10^{-6}	energy convergence limit (in eV)
	static	10^{-8}	
`EDIFFG`	all	-5×10^{-3}	force convergence limit (in eV Å^{-1})
`LAECHG`	static	.TRUE.	also calculate core charge

Table A.2: Deviations from the computational settings of the bulk reference calculation (Table A.1) for the calculation of the properties magnetite-(001)/formic-acid interfaces in Chapter 4 with VASP.

Setting	Step	Value	Description
`LDAUL`	all	2 -1 -1 -1	adjust for additional species
`LDAUU`	all	4.0 0.0 0.0 0.0	
`LDAUJ`	all	0.0 0.0 0.0 0.0	
`ISMEAR`	pre	0	gaussian smearing
	relax	0	
	refine	0	
	static	-5	no smearing (tetrahedron method with Blöchl corrections)
`SIGMA`	all	0.05	width for gaussian smearing
`IBRION`	pre	-1	no relaxation
	relax	2	conjugate gradient algorithm
	refine	2	conjugate gradient algorithm
	static	-1	no relaxation
`NSW`	pre	0	maximum number of relaxation steps
	relax	200	
	refine	500	
	static	0	
`NELM`	pre	500	maximum number of electronic steps
	relax	300	
	refine	300	
	static	600	
`EDIFF`	pre	2×10^{-4}	energy convergence limit (in eV)
	relax	2×10^{-5}	
	refine	2×10^{-6}	
	static	2×10^{-8}	
`EDIFFG`	relax	-5×10^{-2}	force convergence limit (in $\mathrm{eV\,\AA^{-1}}$)
	refine	-5×10^{-3}	
`LDIPOL`	not pre	.TRUE.	include dipole corrections
`IDIPOL`	not pre	3	correct dipole along surface normal
`DIPOL`	not pre	xx yy zz	coordinates of the centre of mass

Table A.3: Deviations from the computational settings of the bulk reference calculation (Table A.1) for the calculation of the properties magnetite-(111)/formic-acid interfaces in Chapter 4 with VASP.

Setting	Step	Value	Description
`LDAUL`	all	2 -1 -1 -1	adjust for additional species
`LDAUU`	all	4.0 0.0 0.0 0.0	
`LDAUJ`	all	0.0 0.0 0.0 0.0	
`ISPIN`	pre	1	pre-converge without magnetic moments
`ICHARG`	relax	1	start from non-magnetic density
`ISMEAR`	pre	0	gaussian smearing
	relax	0	
	refine	0	
	static	-5	no smearing (tetrahedron method with Blöchl corrections)
`SIGMA`	all	0.05	width for gaussian smearing
`IBRION`	pre	-1	no relaxation
	relax	2	conjugate gradient algorithm
	refine	2	conjugate gradient algorithm
	static	-1	no relaxation
`NSW`	pre	0	max. number of relaxation steps
	relax	200	
	refine	500	
	static	0	
`NELM`	pre	500	max. number of electronic steps
	relax	300	
	refine	300	
	static	600	
`EDIFF`	pre	2×10^{-4}	energy convergence limit (in eV)
	relax	2×10^{-5}	
	refine	2×10^{-6}	
	static	2×10^{-8}	
`EDIFFG`	relax	-1×10^{-2}	force convergence limit (in eV Å^{-1})
	refine	-5×10^{-3}	
`LDIPOL`	not pre	.TRUE.	include dipole corrections
`IDIPOL`	not pre	3	correct dipole along surface normal
`DIPOL`	not pre	xx yy zz	coordinates of the centre of mass

Table A.4: Special settings of the DFPT calculations for the determination of vibrational modes of formic acid on magnetite surfaces.

Setting	Value	Description
`IBRION`	7	DFPT calculation
`LEPSILON`	.TRUE.	calculate BECs
`LREAL`	.FALSE.	more accurate BECs
`ISMEAR`	0	gaussian smearing
`SIGMA`	0.05	width for gaussian smearing
`NSW`	1	technically static calculation
`NELMIN`	10	minimum number of electronic steps
`NELM`	120	maximum number of electronic steps
`EDIFF`	2×10^{-8}	energy convergence limit (in eV)
`NFREE`	2	perturbations with positive and negative sign
`POTIM`	0.02	perturbation scaling parameter
`ISYM`	0	switch off symmetry (recommended)
`NWRITE`	3	output setting for normal modes

stricter convergence criterion. Fourth, a static calculation yields more accurate energies and electronic structure of the final atomic structure. This basic sequence (pre, relax, refine, static) is the same for calculations on interfaces built with the (001) and the (111) surfaces, although the detailed settings within each step differ slightly for the different surfaces. In general, the settings are of course equal to the ones of the reference calculations on bulk magnetite. The deviations from those settings due to the existence of a surface, and the additional pre-convergence and refinement steps in the new sequence are documented in Tables A.2 and A.3.

The k-point grids applied in the calculations follow the inverse size of the corresponding unit cells. For molecular reference calculations only a single k-point is used. For the $(\sqrt{2} \times \sqrt{2})$R45° unit cell of the (001) surface a $5 \times 5 \times 1$ grid is employed, while the smaller non-reconstructed 1×1 unit cell necessitates a finer $7 \times 7 \times 1$ grid. On the (111) surface, the calculations are performed with the same k-point grids of $7 \times 7 \times 1$ and $5 \times 5 \times 1$ for the smaller 1×1 unit cell and the larger $(\sqrt{3} \times \sqrt{3})$R30° superstructure, respectively.

Vibrational modes and their intensities are calculated using Density Functional Perturbation Theory (DFPT) and Born effective charges (BEC) as described in Chapter 2. In order to set up these kind of calculations some input parameters have to be changed and added to the VASP input files. These special settings for DFPT calculations are listed in Table A.4. The k-point grid is not changed, and the refined atomic structure is used as the starting point for applying small perturbations.

A.2 Settings for titania/hydrohalic-acid interfaces

All DFT calculations shown in Chapter 5 are performed with the optB88-vdW [33, 34] XC-functional as already mentioned in the introduction of that chapter. A comparison with results obtained with the PBE [30] XC-functional can be found in Appendix C. All atoms are modelled using the pseudopotential approach, where only the outer (valence) electrons are treated explicitly. For the atomic species relevant in Chapter 5 the following number of outer electrons were considered to be valence electrons: Ti – 10, O – 6, H – 1, X – 7 (where $X = \mathrm{F}, \mathrm{Cl}, \mathrm{Br}, \mathrm{I}$). The interfaces are modelled with symmetric slabs, which allows to neglect dipole corrections. Different sets of k-points are employed depending on the underlying anatase TiO_2 surface. For the (101) and (100) surfaces a grid of $7 \times 3 \times 1$ is created, while for the (001) surface the non-reconstructed structure is simulated based on a $7 \times 7 \times 1$ k-points grid and the reconstructed structure uses a $3 \times 7 \times 1$ k-points grid. Reference calculations for the bulk structure of anatase TiO_2 and the different molecules in vacuum are performed with a k-point grid of $13 \times 13 \times 5$ and a single k-point, respectively. All structures are relaxed in two steps, an initial relaxation using the conjugate gradient algorithm and a refined relaxation using a quasi-Newton algorithm. During both relaxations all atomic positions are optimised with respect to the total energy. After the relaxation converges to a minimum energy state, a static calculation is performed in order to get a more accurate total energy as recommended in the VASP manual. All input parameters of the three calculation steps (initial, refined, static) as provided in the INCAR-files of VASP are provided in Table A.5. Previous work already showed that physical properties calculated with these settings are converged well.

Table A.5: Computational settings for the calculation of the adsorption, substitution, and surface energies of titania/hydrohalic-acid interfaces in Chapter 5 with VASP. M is the number of atoms in the structure.

Setting	Step	Value	Description
`GGA`	all	BO	settings for optB88-vdW XC-functional
`PARAM1`	all	0.1833333	
`PARAM2`	all	0.2200000	
`LUSE_VDW`	all	.TRUE.	
`AGGAC`	all	0.0000	
`ENCUT`	all	520	cut-off energy (in eV)
`PREC`	all	Accurate	precision setting
`LREAL`	all	Auto	real-space projection
`ISMEAR`	initial	0	gaussian smearing
	refined	0	
	static	-5	no smearing (tetrahedron method with Blöchl corrections)
`SIGMA`	all	0.05	width for gaussian smearing
`IBRION`	initial	2	relax with conjugate gradient algorithm
	refined	1	relax with quasi-Newton algorithm
	static	-1	no relaxation
`ISIF`	all	2	relax atomic positions, but not unit cell
`NSW`	initial	100	maximum number of relaxation steps
	refined	600	
	static	0	
`NELMIN`	initial	3	minimum number of electronic steps
	refined	4	
	static	5	
`NELM`	all	60	maximum number of electronic steps
`EDIFF`	initial	$M \cdot 10^{-3}$	energy convergence limit (in eV)
	refined	$M \cdot 10^{-3}$	
	static	$M \cdot 10^{-6}$	
`EDIFFG`	all	-5×10^{-3}	force convergence limit (in eV Å^{-1})
`LWAVE`	all	.FALSE.	do not write wave function
`LCHARG`	all	.FALSE.	do not write charge density

A.3 Settings for virtual mechanical tests of titania/carboxylic-acid interfaces

In order to limit the computational costs, only one DFT calculation is performed at each displacement step for the simulations presented in Chapter 6. As described in that Chapter, the atomic positions of all atoms in the interface region are relaxed to their local energy minimum, and the PBE [30] XC-functional is used. For interfaces built with the (101) and (100) surfaces of anatase TiO_2, a k-point grid of $7 \times 3 \times 1$ was employed, while for interfaces built with the (001) surface a grid of $7 \times 5 \times 1$ was used. The atomic core and the inner electrons were described by pseudopotentials. Only the outer 12, 6, 4, and 1 valence electrons of Ti, O, C, and H, respectively, were treated explicitly. The remaining settings are shown in Table A.6 as defined in the INCAR-file in VASP.

Table A.6: Computational settings for the calculation of mechanical properties of titania/carboxylic-acid interfaces in Chapter 6 with VASP.

Setting	Value	Description
`ENCUT`	520	cut-off energy (in eV)
`PREC`	Accurate	precision setting
`LREAL`	Auto	real-space projection
`ISMEAR`	0	gaussian smearing
`SIGMA`	0.05	width for gaussian smearing
`IBRION`	2	relax with conjugate gradient algorithm
`ISIF`	2	relax atomic positions, but not unit cell
`NSW`	500	maximum number of relaxation steps
`NELMIN`	4	minimum number of electronic steps
`NELM`	500	maximum number of electronic steps
`EDIFF`	10^{-4}	energy convergence limit (in eV)
`EDIFFG`	-5×10^{-3}	force convergence limit (in eV Å^{-1})
`GGA`	PE	use PBE XC-functional
`LDIPOL`	.TRUE.	include dipole corrections
`IDIPOL`	3	correct dipole along surface normal
`DIPOL`	xx yy zz	coordinates of the centre of mass
`LWAVE`	.FALSE.	do not write wave function
`LCHARG`	.FALSE.	do not write charge density

B

Convergence tests

In order to balance the accuracy of the computational results with the computational costs needed to obtain these results, the employed methods need to be converged with respect to some settings, such as the cut-off energy or the number of k-points. The key convergence tests for interfaces between TiO_2 and hydrohalic or carboxylic acids have already been performed in previous work, which is why this appendix focuses on convergence tests for magnetite interfaces. Furthermore, the surface energy is one of the most important quantities for the analysis of the results in this thesis. Therefore, not only the convergence of total energies, but also the convergence of surface energies with respect to the cut-off energy and the number of atomic layers in the surface slab is highlighted in this appendix. Moreover, the calculation of mechanical properties in Chapter 6 necessitated a convergence test with respect to the step size of the displacement algorithm, which is also presented here.

B.1 Bulk magnetite, magnetite surfaces, and interfaces

Number of k-points

Convergence of the total energies with respect to the number of k-points was tested for bulk magnetite, and the clean (001) and (111) surfaces. On the (001) surface, both the bulk truncation and the reconstructed (SCV) structure were tested, while on the (111) surface only the Fe_{tet1} termination was examined due to the equal sizes of the unit cells for different terminations. Figure B.1 shows the results of the convergence tests. Most computational studies try to achieve a convergence within 1 meV/atom. From Figure B.1 it becomes obvious that this limit can be achieved easily with only 20 irreducible k-points and less for the systems studied in this thesis.

Cut-off energy

The convergence of the total energy with respect to the cut-off energy was tested for several reference systems that are needed to calculate the adsorption and surface energies in Chapter 4. The results of these tests are shown in Figure B.2a, and reveal that achieving a convergence within ±1 meV/atom

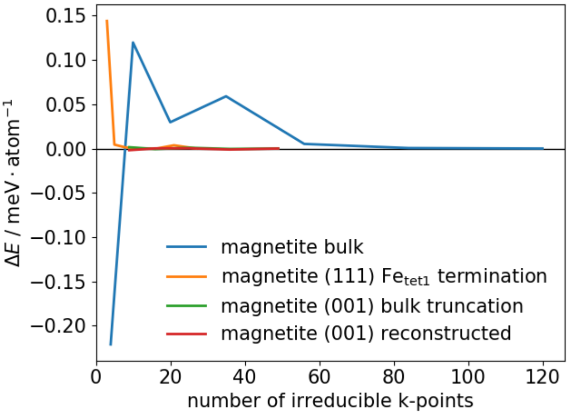

Figure B.1: Convergence of the total energy of bulk magnetite and different magnetite surface structures with respect to the number of irreducible, i.e. symmetrically inequivalent, k-points. The energy difference ΔE in each dataset is referenced against the energy for the maximum number of k-points studied in the dataset.

requires cut-off energies larger than 700 eV. However, the total energy calculated with DFT does not have any physical meaning. Quantities that are practically relevant, such as surface energies, are always based on differences between total energies. The curves in Figure B.2a already indicate that these energy differences may converge much faster. Plotting the surface energy of a magnetite/formic-acid interface in Figure B.2b shows that a cut-off of 520 eV gives a result converged within $\pm 1\,\mathrm{mJ\,m^{-2}}$. This is up to orders of magnitudes better than what is usually achieved for the convergence with respect to the number of atomic layers in the slab model, which is discussed in the next section.

Number of slab layers

The convergence of the calculated surface energies of the magnetite (001) and (111) surfaces with respect to the number of layers in the structures was carefully tested in order to obtain reliable results with a minimum amount of computational effort. Slabs with 9, 13, and 17 layers were tested for the magnetite (001) surface, which yielded a convergence of the surface energy within less than $0.1\,\mathrm{J\,m^{-2}}$ for the final chosen value of 13 layers. The same accuracy was reached on the (111) surface for a 17 layer slab from a comparison of slabs with 11, 17, and 23 layers.

As an additional convergence criterion the relaxation of the bulk like layers

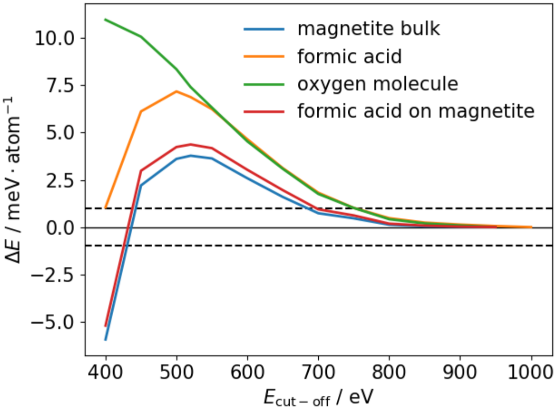

(a)

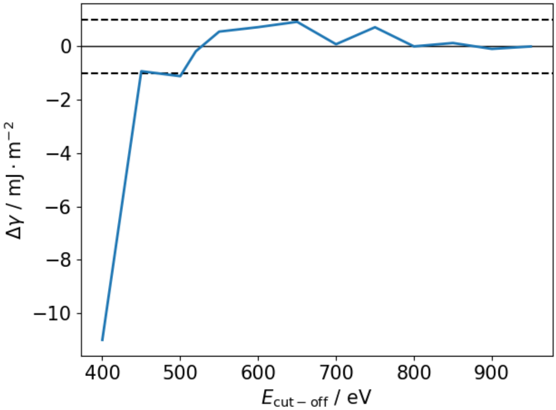

(b)

Figure B.2: Results of the convergence testing with respect to the cut-off energy $E_{\mathrm{cut-off}}$. (a) Total energy convergence of bulk magnetite, formic acid, molecular oxygen, and a magnetite/formic-acid interface (formic acid adsorbed on the tet-site of the bulk truncated 1×1 (001) surface). The energy difference ΔE in each dataset is referenced against the energy for the maximum $E_{\mathrm{cut-off}}$ studied in the dataset. (b) Convergence of the surface energy of the magnetite/formic-acid interface calculated from the energies in (a).

was used. Only when the atomic positions in these inner layers change by less than 0.1 Å compared to the original bulk positions, the structure can be employed to model a nanoparticle surface. This provides additional assurance that the interactions between the top and bottom of the slab are negligible. For both the 13 layer slab on the (001) surface and the 17 layer slab on the (111) surface this additional criterion was met, qualifying them for further modelling.

B.2 Mechanical properties of carboxylic acids

The set-up for the virtual mechanical testing of interfaces introduced in Chapter 6 has a few free parameters that need to be adjusted to optimise the balance between accuracy and computational costs. The most important one is the size of the displacement steps. Here, four different step sizes ranging from 0.05 Å to 0.4 Å are tested for the tensile stretching of 1,4−butanoic acid as an example. Figure B.3 shows the molecule and the resulting force-displacement-curves for the different step sizes. The mechanical response of the molecule is clearly distorted for the widest step size of 0.4 Å, and for a step size of 0.2 Å the breaking displacement and force do not seem to be converged yet. Comparing step sizes of 0.1 Å and 0.05 Å, the difference is rather small and the

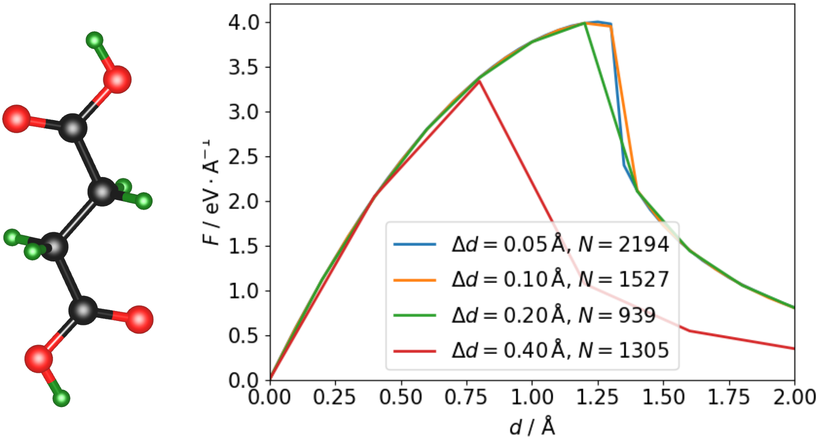

Figure B.3: Force (F) versus displacement (d) curves of the butanoic acid molecule shown on the left (colour code: O – red, C – black, H – green) stretched along its symmetry axis with the COGEF method using different step sizes Δd. The total number of relaxation steps N that was needed to obtain each curve is shown in the figure legend, too.

molecule breaks at the same displacement of 1.3 Å. Interestingly, the number of relaxation steps needed to obtain the forces for all displacements below 2 Å does not decrease monotonically with increasing step size. If the step size is too high, the difference between structures of two consecutive steps leads to an increased number of relaxation steps in between displacements steps. As a result of this convergence study, a step size of 0.1 Å is chosen for the investigation of mechanical properties of interfaces.

Another parameter that could be optimised is the force convergence limit for the relaxation of atomic positions in between two displacement steps. The relaxation is only stopped, when the forces on the atoms that are not fixed and displaced in each step fall below this limit. Tests with different values of the force convergence limit between 0.5 meV Å^{-1} and 10 meV Å^{-1} confirmed that the calculated forces on the fixed atoms vary in the same range as the convergence limit. However, since the total forces are typically of the order of some eV Å^{-1}, typical force convergence limits of 5 meV Å^{-1} to 10 meV Å^{-1} are accurate enough for the prediction of mechanical properties of interfaces.

C Comparison of different exchange-correlation functionals

The selection of the exchange-correlation (XC) functional influences the computational costs of a DFT calculation and how accurately it describes real-world systems. A comparison of results obtained with different functionals and experimental methods can help to choose a functional and assess the impact of this choice. This appendix presents comparisons of different XC functionals for many systems relevant in this thesis.

C.1 Properties of bulk magnetite

The properties of bulk magnetite were calculated with six different descriptions of the exchange-correlation potential: PBE, PBE+U, optB86b-vdW+U, optB88-vdW+U, optPBE-vdW+U, and SCAN. *PBE* stands for the GGA functional developed by J.P. Perdew, K. Burke, and M. Ernzerhof [30], while *optB86b-vdW*, *optB88-vdW*, and *optPBE-vdW* are the re-parametrisations of the corresponding GGA functionals by J. Klimeš, D.R. Bowler, and A. Michaelides [33, 34], which account for van-der-Waals interactions. The meta-GGA functional *SCAN* by J. Sun, A. Ruzsinszky, and J.P. Perdew [31] is the first to meet all constraints known for functionals in this type of approximation. The *+U* in the names stands for a Hubbard correction [35] in the description of Dudarev *et al.* [172] with an effective parameter U_{eff} of 4.0 eV applied to the d-orbitals of the iron atoms.

As can be seen from Table C.1, the inclusion of the Hubbard correction increases the lattice constant and band gap in the majority spin component of magnetite, while the parameter u, describing the distortion of oxygen polyhedra in the spinel structure, is almost unaffected by the choice of the functional. The best agreement with the measured lattice constant is achieved by the PBE functional, followed by the optB86b-vdW+U functional.

The magnetic moments of the different sites in magnetite are shown in Table C.2. The stronger localisation of electrons due to the Hubbard correction increases the local magnetic moments on iron atoms, which leads to a better agreement with the experimental result for functionals that apply the Hubbard correction.

The partial charges shown in Table C.3 show a similar trend, but since local charges are more difficult to measure than local magnetic moments, an

Table C.1: Comparison of the lattice constant a, distortion parameter u, and band gap E_G between valence and conduction band in the majority spin component of bulk magnetite calculated with different XC functionals.

Functional	a / Å	u / Å	E_G / eV
PBE	8.394	0.038	0.67
PBE+U	8.480	0.037	2.18
optB86b-vdW+U	8.429	0.038	2.13
optB88-vdW+U	8.445	0.038	2.10
optPBE-vdW+U	8.493	0.037	2.12
SCAN	8.334	0.041	1.43
Experimental [109]	8.396		

Table C.2: Comparison of the magnetic moments of the atomic sites in bulk magnetite calculated with different XC functionals and using the Bader formalism [173]. The total magnetic moment per formula unit is $4\,\mu_\mathrm{B}$, regardless of the XC functional. $\mu_\mathrm{tot,Fe}$ averages over all iron atoms in the cell and was included for comparison with the value measured in experiments.

Functional	$\mu_\mathrm{tot,Fe}$ / μ_B	$\mu_{\mathrm{Fe}_\mathrm{tet}}$ / μ_B	$\mu_{\mathrm{Fe}_\mathrm{oct}}$ / μ_B	μ_O / μ_B
PBE	3.64	-3.55	3.60	0.09
PBE+U	3.81	-4.08	3.95	0.05
optB86b-vdW+U	3.80	-4.05	3.93	0.05
optB88-vdW+U	3.80	-4.05	3.92	0.05
optPBE-vdW+U	3.81	-4.07	3.94	0.05
SCAN	3.72	-3.88	3.80	0.07
Experimental [106]	3.90 ± 0.09			

experimental comparison is not possible in this case. Interestingly, the distribution of partial charges obtained with the SCAN functional is similar to the distributions from the Hubbard corrected functionals, even though the local magnetic moments differ. This shows that the SCAN functional partially accounts for some effects that lead to a stronger localisation of electrons.

In summary, the differences between the Hubbard corrected functionals compared here are very small and independent of the inclusion of van-der-Waals interactions. Not including Hubbard corrections seems to alter the electronic structure significantly, even though the SCAN functional seems to account partially for similar effects. A recent paper showed that a smaller Hubbard correction applied to the SCAN functional can improve the accuracy of formation enthalpy predictions for different TiO_2 polymorphs [150]. Future studies on magnetite might follow this approach in order to improve the accuracy of atomic and electronic structure predictions.

Table C.3: Comparison of the partial charges of the atomic sites in bulk magnetite calculated with different XC functionals and using the Bader formalism [173]. The bulk unit cell is charge neutral in the calculation, deviations in the table may appear due to rounding errors.

Functional	$q_{\mathrm{Fe}_{\mathrm{tet}}}$ / e	$q_{\mathrm{Fe}_{\mathrm{oct}}}$ / e	q_{O} / e
PBE	+1.48	+1.44	-1.09
PBE+U	+1.65	+1.51	-1.17
optB86b-vdW+U	+1.64	+1.50	-1.16
optB88-vdW+U	+1.63	+1.50	-1.16
optPBE-vdW+U	+1.65	+1.50	-1.16
SCAN	+1.64	+1.53	-1.17

C.2 Formic acid adsorption on magnetite (001)

The discussion of formic acid adsorption on magnetite in Chapter 4 is based on the adsorption and surface energies calculated with the PBE+U functional. However, the adsorption can be largely affected by the atomic distances on the surface, and organic molecules can exhibit significant van-der-Waals interactions. Therefore, the results for some important structures are compared to results obtained with the optB86b-vdW+U functional, which shows a good agreement with the experimental lattice constant and includes van-der-Waals interactions (see Table C.4).

As expected, the adsorption energies are slightly larger with the optB86b-vdW+U functional due to the inclusion of van-der-Waals forces. Nevertheless, the preference for the *tet* adsorption site is the same with almost exactly the same energy difference. The comparison of surface energies calculated with the different functionals shows a similar trend: the absolute values differ significantly, while the difference in relative stabilities is in the range of the

Table C.4: Comparison of adsorption energies E_{ad} of formic acid on different sites of the bulk truncated (BT) magnetite (001) surface, and surface energies γ of the clean magnetite (001) surface in the reconstructed (SCV) and bulk truncated (BT) structure, obtained with different XC functionals.

Property	PBE+U	optB86b-vdW+U
E_{ad} (BT, int-site)	$-2.076\,\mathrm{eV}$	$-2.271\,\mathrm{eV}$
E_{ad} (BT, tet-site)	$-2.117\,\mathrm{eV}$	$-2.319\,\mathrm{eV}$
ΔE_{ad} (int-site vs. tet-site)	$0.041\,\mathrm{eV}$	$0.048\,\mathrm{eV}$
γ_{SCV} (clean)	$-0.636\,\mathrm{J\,m^{-2}}$	$-0.392\,\mathrm{J\,m^{-2}}$
γ_{BT} (clean)	$0.035\,\mathrm{J\,m^{-2}}$	$0.331\,\mathrm{J\,m^{-2}}$
$\lvert\gamma_{\mathrm{SCV}} - \gamma_{\mathrm{BT}}\rvert$ (clean)	$0.671\,\mathrm{J\,m^{-2}}$	$0.723\,\mathrm{J\,m^{-2}}$

convergence accuracy limit. Therefore, it can be concluded that the relative stabilities predicted with PBE+U are accurate enough and comparable to other functionals.

C.3 Hydrohalic acid adsorption and substitution on anatase TiO_2 surfaces

Inorganic systems, such as TiO_2 or hydrohalic acids, are often modelled using the PBE XC functional by J.P. Perdew, K. Burke, and M. Ernzerhof [30]. However, the comparison with results on carboxylic acids in Chapter 5 that show significant van-der-Waals interactions necessitated a modelling with the optB88-vdW functional by J. Klimeš, D.R. Bowler, and A. Michaelides [33, 34]. Here, results obtained with both functionals are compared to asses the differences.

The influence of the functionals on the adsorption energies of the different hydrohalic acids on anatase TiO_2 surfaces is shown in Table C.5. The inclusion of van-der-Waals interactions increases the absolute adsorption energies, especially for the larger halides up to the point where the order of adsorption energies changes. For example, hydrogen iodide adsorbs more strongly than hydrogen chloride on all surfaces using the optB88-vdW functional, while it is the other way around on most surfaces for calculations with the PBE functional. The hydroxyl group substitution energies, however, are not affected significantly by the choice of the XC functional (see Table C.6). Nevertheless, the inclusion of van-der-Waals interactions seems necessary for the modelling of hydrohalic acids in general, since they contribute significantly to the binding of larger hydrohalic acids.

Table C.5: Comparison of the adsorption energies E_{ad} for hydrohalic acids (HX, where $X = F, Cl, Br, I$) on the (001), (100), and (101) surfaces of anatase TiO_2 obtained with the optB88-vdW or PBE XC functional.

Species	Functional	$E_{\mathrm{ad}}(001)$	$E_{\mathrm{ad}}(100)$	$E_{\mathrm{ad}}(101)$
HF	optB88-vdW	−1.43	−1.33	−1.41
	PBE	−1.24	−1.10	−1.16
HCl	optB88-vdW	−1.12	−1.11	−1.25
	PBE	−0.83	−0.78	−0.87
HBr	optB88-vdW	−1.19	−1.21	−1.36
	PBE	−0.86	−0.84	−0.95
HI	optB88-vdW	−1.12	−1.17	−1.34
	PBE	−0.72	−0.75	−0.88

Table C.6: Comparison of the hydroxyl group substitution energies E_{sub} for hydrohalic acids (HX, where $X = F, Cl, Br, I$) on the (001), (100), and (101) surfaces of anatase TiO_2 obtained with the optB88-vdW or PBE XC functional.

Species	Functional	$E_{\text{sub}}(001)$	$E_{\text{sub}}(100)$	$E_{\text{sub}}(101)$
HF	optB88-vdW	−0.40	−0.24	−0.11
	PBE	−0.45	−0.33	−0.22
HCl	optB88-vdW	2.43	0.30	0.47
	PBE	2.45	0.34	0.49
HBr	optB88-vdW	1.83	0.60	0.77
	PBE	1.90	0.65	0.80
HI	optB88-vdW	1.06	1.11	1.19
	PBE	1.15	1.09	1.17

D

Supporting Information

Some data was not important enough to be shown in the main part of this thesis, but still could be interesting for a more detailed understanding of the topic. Therefore, some supporting information is provided in this appendix. It contains a detailed description of the conversion of chemical potential shifts to gas pressures for formic acid, additional information on the vibrational modes of formic acid on magnetite surfaces, and more illustrations of the atomic structures of interfaces with and without a mechanical load.

Additionally, animations were created to illustrate vibrational modes of formic acid on magnetite and the structural evolution of titania/carboxylic-acid interfaces under tensile load. These animations can be downloaded from `https://doi.org/10.15480/336.3408`, which can also be accessed by scanning the QR code on the right.

SCAN ME

D.1 Conversion of chemical potential to pressure for formic acid

As described in Chapter 2, the conversion of chemical potential shifts to ideal gas pressures is straightforward. Formic acid (f.a., HCOOH), however, is not an ideal gas, since two formic acid molecules interact significantly, which leads to the formation of formic acid dimers in standard conditions. Nevertheless, the phase diagrams shown in Chapter 4 connected the formic acid potential shift to gas pressures. Here, this connection is derived for the more complex case of a dimer forming gas.

Assuming that the dimer and monomer variants of formic acid are in a thermodynamic equilibrium state at all times, the ratio between monomer and dimer can be calculated from the equilibrium constant

$$K_p = \exp\left(-\frac{\Delta_r G_f(p,T)}{k_\mathrm{B}T}\right) = \frac{p_\mathrm{monomer}^2}{p_\mathrm{dimer}}, \tag{D.1}$$

where $\Delta_r G_f(p,T)$ is the reaction free enthalpy at formic acid pressure p and temperature T of the equilibrium reaction

$$\mathrm{dimer} \rightleftharpoons 2 \cdot \mathrm{monomer}, \tag{D.2}$$

which can be determined from the difference in formation enthalpies, and k_B is Boltzmann's constant. The total formic acid pressure p is the sum of the partial pressures of the dimer and monomer components of the gas ($p = p_\mathrm{dimer} + p_\mathrm{monomer}$). Introducing the abbreviation $x_p = \frac{p_\mathrm{dimer}}{p}$ for the dimer content in the gas, and inserting this into equation (D.1), a quadratic equation is obtained that has only one solution for $0 < x_p < 1$:

$$x_p = 1 + \frac{K_p}{2p} - \sqrt{\left(\frac{K_p}{2p}\right)^2 + \frac{K_p}{p}} \tag{D.3}$$

The change of the dimer content with pressure and temperature is illustrated in Figure D.1a using thermochemical data from J. Chao and B.J. Zwolinski [135]. As expected intuitively, the dimer content increases with increasing pressure, and decreases with increasing temperature.

The chemical potential of a formic acid molecule $\mu_\mathrm{f.a.}$ can be written as a sum of contributions from formic acid molecules in dimer and monomer configurations, since this represents a simple sum of Gibbs free enthalpies:

$$\mu_\mathrm{f.a.} = \frac{N_\mathrm{dimer}}{N_\mathrm{f.a.}} \cdot \mu_\mathrm{dimer} + \frac{N_\mathrm{monomer}}{N_\mathrm{f.a.}} \cdot \mu_\mathrm{monomer} \tag{D.4}$$

Here, N_dimer and N_monomer denote the number of dimers and monomers, respectively, while $N_\mathrm{f.a.} = 2N_\mathrm{dimer} + N_\mathrm{monomer}$ is the total number of formic acid molecules. For practical reasons, the chemical potential shift $\Delta\mu_\mathrm{f.a.}$ is defined

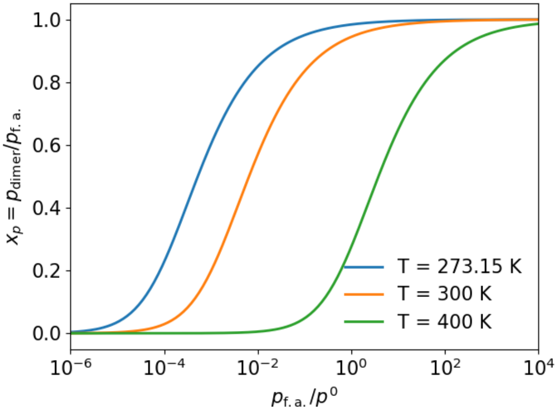

(a)

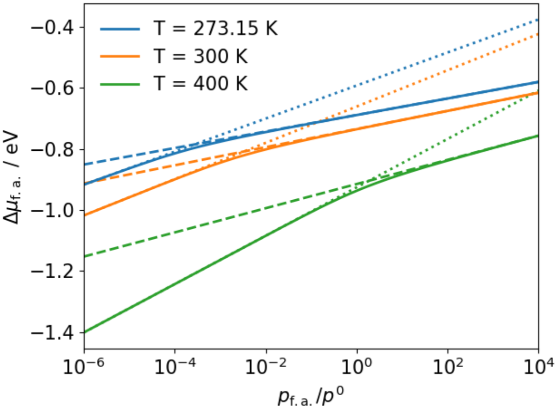

(b)

Figure D.1: Conversion of formic acid pressure $p_{\mathrm{f.a.}}$ to the dimer content $x_p = p_{\mathrm{dimer}}/p_{\mathrm{f.a.}}$ (a), and to the chemical potential shift $\Delta\mu_{\mathrm{f.a.}}$ (b) for different temperatures. The curves are calculated from equations (D.3) and (D.8) using thermochemical data from [135] for parametrisation. Dashed and dotted lines in (b) depict the curves of pure formic acid monomers and pure formic acid dimers, respectively.

with reference to the energy of a single formic acid molecule in vacuum at 0 K $E_{\text{f.a.}}$, which can be calculated with DFT, leading to

$$\begin{aligned}\Delta\mu_{\text{f.a.}} &= \mu_{\text{f.a.}} - E_{\text{f.a.}} \\ &= \frac{N_{\text{dimer}}}{N_{\text{f.a.}}} \cdot (E_b + \Delta\mu_{\text{dimer}}(p,T)) + \frac{N_{\text{monomer}}}{N_{\text{f.a.}}} \cdot \Delta\mu_{\text{monomer}}(p,T),\end{aligned} \tag{D.5}$$

where $E_b = E_{\text{dimer}} - 2E_{\text{f.a.}}$ is the binding energy of the formic acid dimer, accounting for the difference to the monomer reference state.

In the following it is assumed that the pure monomer gas and the pure dimer gas can be approximated by the ideal gas equations and that both gasses form an ideal mixture. This is justified due to the absence of a transition to trimers or tetramers, which would indicate further monomer–dimer or dimer–dimer interactions. With these assumptions, the chemical potential shifts of the dimer and monomer gas can be calculated from

$$\Delta\mu(p,T) = \Delta\mu(p^\circ,T) + k_{\text{B}}T\ln(p/p^\circ), \tag{D.6}$$

where p° is the standard pressure of 1 bar. Furthermore, the dimer content can be expressed in terms of the number of dimers and monomers, yielding

$$\frac{N_{\text{dimer}}}{N_{\text{f.a.}}} = \frac{x_p}{1+x_p} \quad \text{and} \quad \frac{N_{\text{monomer}}}{N_{\text{f.a.}}} = \frac{1-x_p}{1+x_p}. \tag{D.7}$$

Inserting these formulas into equation (D.5) finally gives the expression that connects the formic acid pressure to its shift in chemical potential:

$$\begin{aligned}\Delta\mu_{\text{f.a.}}(p,T) = \frac{1}{1+x_p} \cdot [&x_p \cdot (E_b + \Delta\mu_{\text{dimer}}(p^\circ,T)) \\ &+ (1-x_p)\cdot\Delta\mu_{\text{monomer}}(p^\circ,T) \\ &+ \text{k}_{\text{B}}T\ln(p/p^\circ) \\ &+ \text{k}_{\text{B}}T\cdot(x_p\ln(x_p) + (1-x_p)\ln(1-x_p))]\end{aligned} \tag{D.8}$$

The first two lines of this expression can be understood as the weighted contributions of the dimer and monomer to the temperature dependent chemical potential shift at standard pressure. The third line includes the contribution of a pure increase of the pressure at a given temperature, although it should be noted that the dimer content changes with pressure, leading to an additional influence of pressure through x_p. The last line corresponds to the entropy contribution of an ideal gas mixture with two components.

The influence of temperature and pressure on the chemical potential shift as predicted from equation (D.8) is illustrated in Figure D.1b. For the binding energy E_b, the experimental value of -0.638 eV is used instead of the DFT result of -0.759 eV, in order to be consistent with the thermochemical data used for parametrising the other quantities. Even though the transition from a gas containing mainly monomers to a gas dominated by dimers happens over a broad pressure range, Figure D.1 shows that the deviations from the ideal gas behaviours of pure formic acid monomer and pure formic acid dimer are low. Therefore, the ideal gas equations of the dominating species can be used as an approximation in most cases.

D.2 Vibrational modes of formic acid on magnetite surfaces

The computed vibrational spectra of formic acid on magnetite surfaces were shown in Chapter 4 and compared to experimental data. Sometimes, however, the actual numbers of the vibrational modes become important for further analysis. Therefore, the full lists of calculated vibrational modes, along with their frequencies and intensities, are shown in Tables D.1 to D.3. For the {111}

Table D.1: Calculated vibrational frequencies (in cm^{-1}) of formic acid adsorbed on the int- and tet-site of the SCV $\left(\sqrt{2} \times \sqrt{2}\right)$R45° reconstructed (001) surface of magnetite. The relative intensity derived from the Born effective charges is given in brackets. The modes are labelled according to the corresponding eigenvector of displacements. Note that most modes split into an *in-phase* mode and an *opposing-phase* mode, since two molecules are adsorbed per surface unit cell. Modes with frequencies below 500 cm^{-1} are mainly surface vibrations.

Mode description	int-site	tet-site
$O_{surf}-H_{ad}$ stretching (at Fe_{int})	3684.6 (0.042)	3692.0 (0.031)
$O_{surf}-H_{ad}$ stretching (not at Fe_{int})	3662.6 (0.059)	3670.9 (0.030)
C–H stretching (op.-phase)	2937.8 (0.001)	2940.8 (0.000)
C–H stretching (in-phase)	2929.6 (0.048)	2933.1 (0.067)
O–C–O asym. stretching (op.-phase)	1537.4 (0.000)	1539.5 (0.002)
O–C–O asym. stretching (in-phase)	1522.1 (0.013)	1525.0 (0.098)
O–C–H bending (op.-phase)	1345.9 (0.000)	1344.4 (0.000)
O–C–H bending (in-phase)	1341.3 (0.000)	1343.4 (0.003)
O–C–O sym. stretching (in-phase)	1331.7 (1.000)	1331.9 (1.000)
O–C–O sym. stretching (op.-phase)	1326.0 (0.011)	1331.3 (0.000)
C–H wagging (op.-phase)	1004.4 (0.001)	1000.8 (0.000)
C–H wagging (in-phase)	1000.8 (0.000)	1000.7 (0.000)
$O_{surf}-H_{ad}$ bending (at Fe_{int})	872.2 (0.017)	825.0 (0.011)
O–C–O bending (in-phase)	742.0 (0.730)	750.5 (0.890)
O–C–O bending (op.-phase)	721.1 (0.001)	727.3 (0.000)
$O_{surf}-H_{ad}$ twisting (not at Fe_{int})	697.3 (0.001)	708.2 (0.009)
$O_{surf}-H_{ad}$ bending (not at Fe_{int})	673.9 (0.082)	650.9 (0.016)
$O_{surf}-H_{ad}$ twisting (at Fe_{int})	604.8 (0.000)	648.0 (0.096)

Table D.2: Calculated vibrational frequencies (in cm^{-1}) of formic acid adsorbed on the int- and tet-site of the bulk truncated 1 × 1 (001) surface of magnetite. The relative intensity derived from the Born effective charges is given in brackets. The modes are labelled according to the corresponding eigenvector of displacements. Modes with frequencies below 500 cm^{-1} are mainly surface vibrations.

Mode description	int-site	tet-site
$\mathrm{O_{surf}}$–$\mathrm{H_{ad}}$ stretching	3630.2 (0.127)	3640.0 (0.142)
C–H stretching	2934.1 (0.061)	2942.8 (0.060)
O–C–O asymmetric stretching	1525.2 (0.263)	1529.5 (0.315)
O–C–H bending	1346.8 (0.004)	1342.6 (0.010)
O–C–O symmetric stretching	1333.8 (1.000)	1337.9 (0.664)
C–H wagging	1002.6 (0.000)	1002.3 (0.000)
O–C–O and $\mathrm{H_{ad}}$ bending	748.2 (0.825)	758.1 (1.000)
$\mathrm{O_{surf}}$–$\mathrm{H_{ad}}$ bending	723.8 (0.647)	742.9 (0.057)
O–C–O and $\mathrm{H_{ad}}$ bending	721.9 (0.054)	705.3 (0.294)

Table D.3: Calculated vibrational frequencies (in cm^{-1}) of formic acid adsorbed on the $\mathrm{Fe_{tet1}}$ terminated (111) surface of magnetite at 1/3 monolayer coverage in different quasi-bi-dentate (qbd-↿↾, qbd-↿⇂, and qbd-3NN) and chelating (chel) binding configurations. The relative intensity derived from the Born effective charges is given in brackets. The modes are labelled according to the corresponding eigenvector of displacements. Modes with frequencies below 500 cm^{-1} are mainly surface vibrations. Note that the frequencies are not always in strictly descending order.

Mode description	qbd-↿↾	qbd-↿⇂	qbd-3NN	chel
$\mathrm{O_{surf}}$–$\mathrm{H_{ad}}$ stretching	2935 (0.041)	2919 (0.044)	2944 (0.029)	3557 (0.402)
C–H stretching	2493 (0.006)	2651 (0.030)	2897 (0.047)	2959 (0.050)
O–C–O asym. stretching	1575 (0.288)	1571 (0.160)	1599 (0.130)	1537 (0.107)
C–H bending	1338 (0.097)	1351 (0.013)	1355 (0.025)	1269 (0.007)
O–C–O sym. stretching	1281 (0.503)	1294 (0.760)	1257 (0.462)	1347 (1.000)
$\mathrm{O_{surf}}$–$\mathrm{H_{ad}}$ bending	1153 (0.039)	1049 (0.003)	1033 (0.003)	768 (0.005)
$\mathrm{O_{surf}}$–$\mathrm{H_{ad}}$ bending	1052 (0.003)	1027 (0.012)	919 (0.005)	634 (0.007)
C–H wagging	1002 (0.000)	1000 (0.000)	1001 (0.000)	1011 (0.003)
O–C–O bending	721 (1.000)	713 (1.000)	695 (1.000)	786 (0.392)

facet, only the results for 1/3 monolayer coverage are included, since the structures all have the same stoichiometry and hence, allow for an unambiguous comparison of the frequencies depending on the binding mode. Furthermore, the frequencies for full coverage adsorption are only shifted slightly compared to the 1/3 monolayer structures.

In addition to the tables, some vibrational modes were animated in order to visualize the modes more clearly. These videos can be found on `https:`

`//doi.org/10.15480/336.3408`, which is also accessible via the QR code provided at the beginning of this chapter. For the magnetite (111) surface, the videos show an interesting phenomenon for the triangular adsorption modes at full coverage. In this case, the O−C−O stretching and bending vibrations split up into a *circular* mode and a *non-circular* mode. In the circular mode, all molecules vibrate in-phase, leading to a circular motion for the asymmetric stretching mode, and a combined up-and-down movement in the symmetric stretching and bending modes. Therefore, dynamic dipoles perpendicular to the surface are enhanced in these circular modes, while dynamic dipoles parallel to the surface are suppressed. The opposite happens for the non-circular mode, where two of the adsorbed molecules vibrate in-phase and the remaining molecule vibrates with an opposing phase. Therefore, the non-circular mode has a smaller dynamic dipole perpendicular to the surface, and an increased dynamic dipole parallel to the surface.

A similar, but less complicated vibrational pattern can be observed in the animations of the vibrational modes on the SCV reconstructed surface of magnetite (001). There, the two molecules per surface unit cell can also vibrate in-phase or with opposing phase. However, due to the even number of adsorbate molecules, the opposing-phase modes always have a negligible dynamic dipole moment, while the in-phase modes are enhanced by the concerted motion regardless of the direction of the dynamic dipole.

D.3 Deformation of titania/carboxylic-acid interfaces

In Chapter 6, only some representative atomic structures of anatase-TiO_2/carboxylic-acid interfaces were shown to illustrate the binding modes and failure mechanisms in these interfaces. However, in order to allow the reader to gain the full picture, all starting configurations without an external load and all final configurations after the interface failed under a tensile load, are shown here. This includes the structures already shown in Chapter 6, simplifying the comparison between initial and final state. Additionally, the simulated structural evolution during the tensile loading was animated in short videos, which can be watched and downloaded at `https://doi.org/10.15480/336.3408`, which is also accessible via the QR code provided at the beginning of this chapter.

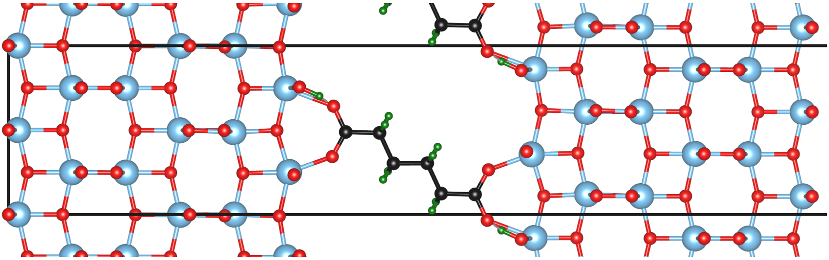

(a) bi-dentate (bd) binding mode

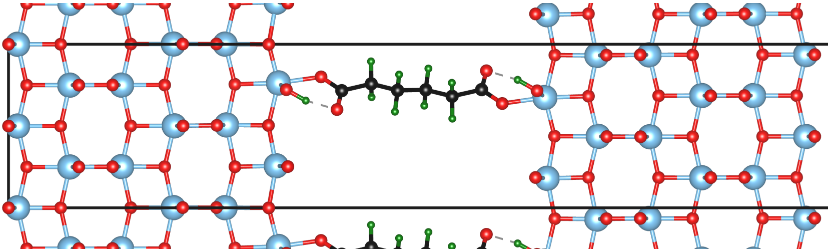

(b) quasi-bi-dentate (qbd) binding mode

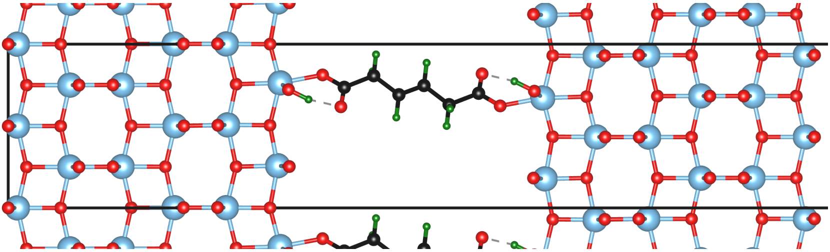

(c) qbd binding mode with a double bond between the third and fourth carbon atom

Figure D.2: Different binding modes of carboxylic acids on anatase TiO_2 (001) studied in Chapter 6. Colour code: Ti – blue, O – red, C – black, H – green.

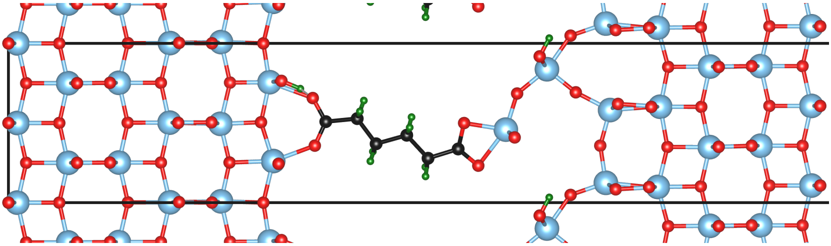

(a) failure of bi-dentate (bd) binding mode

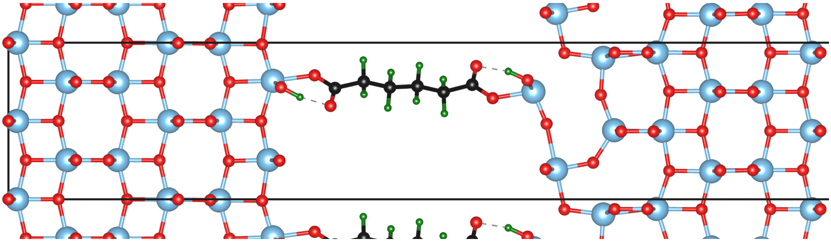

(b) failure of quasi-bi-dentate (qbd) binding mode

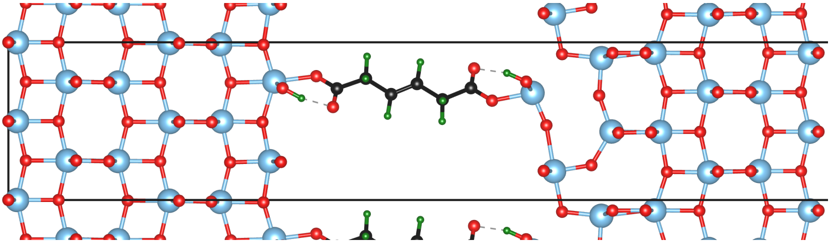

(c) failure of qbd binding mode with a double bond

Figure D.3: Different interface failure geometries of interfaces between anatase TiO_2 (001) and carboxylic acids studied in Chapter 6. Colour code: Ti – blue, O – red, C – black, H – green.

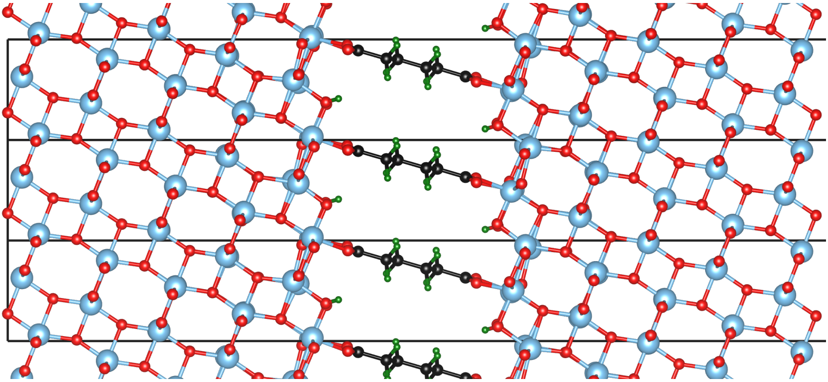

(a) bi-dentate (bd) binding mode

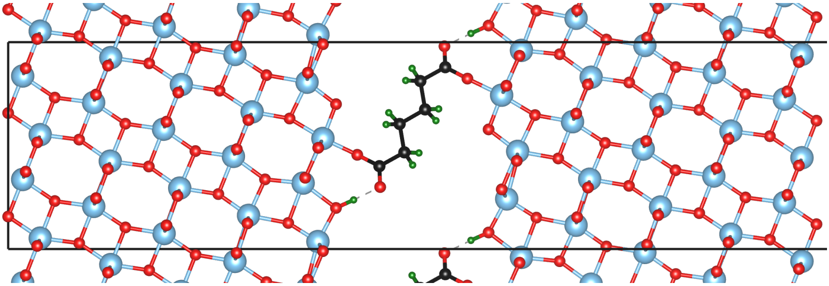

(b) quasi-bi-dentate (qbd) binding mode

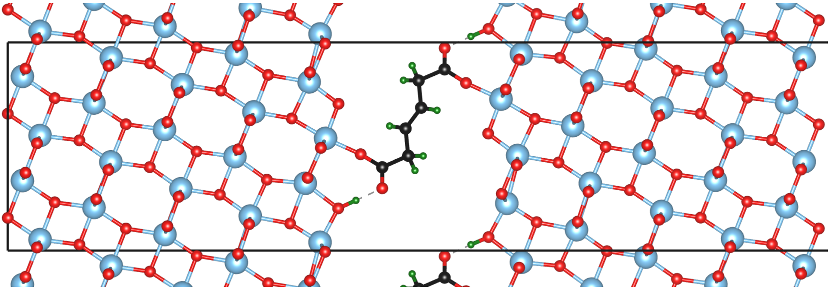

(c) qbd binding mode with a double bond between the third and fourth carbon atom

Figure D.4: Different binding modes of carboxylic acids on anatase TiO_2 (101) studied in Chapter 6. Note that the unit cell for modelling the bi-dentate adsorption mode is not orthogonal, which is why more black lines and molecules appear in that image even though the number of molecules per surface area is the same as in the other structures. Colour code: Ti – blue, O – red, C – black, H – green.

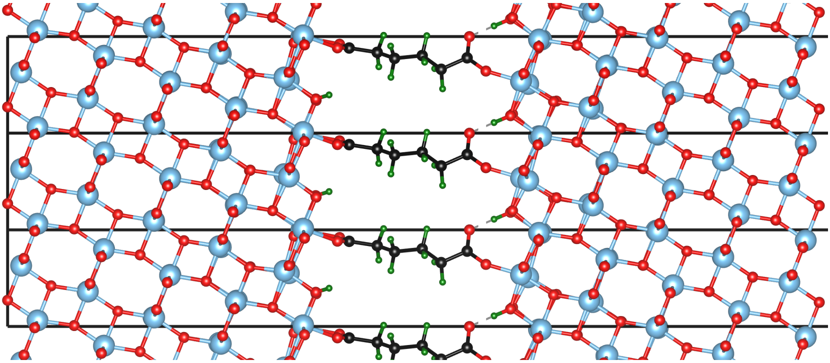

(a) failure of bi-dentate (bd) binding mode

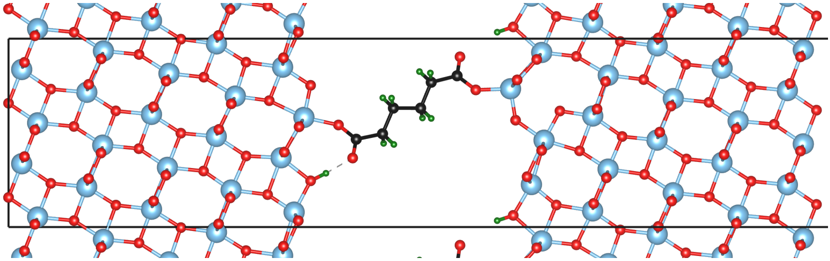

(b) failure of quasi-bi-dentate (qbd) binding mode

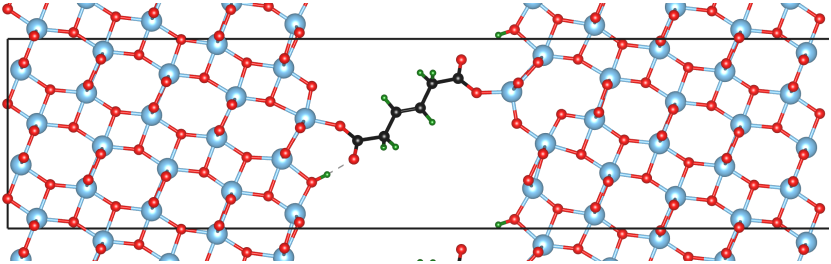

(c) failure of qbd binding mode with a double bond

Figure D.5: Different interface failure geometries of interfaces between anatase TiO_2 (101) and carboxylic acids studied in Chapter 6. Note that the unit cell for modelling the bi-dentate adsorption mode is not orthogonal, which is why more black lines and molecules appear in that image even though the number of molecules per surface area is the same as in the other structures. Colour code: Ti – blue, O – red, C – black, H – green.

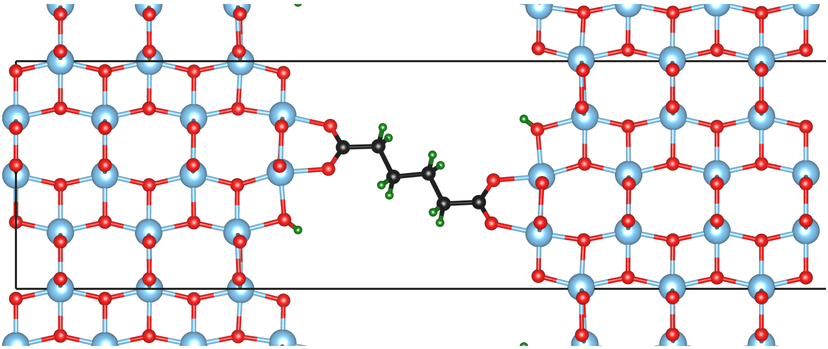

(a) bi-dentate (bd) binding mode

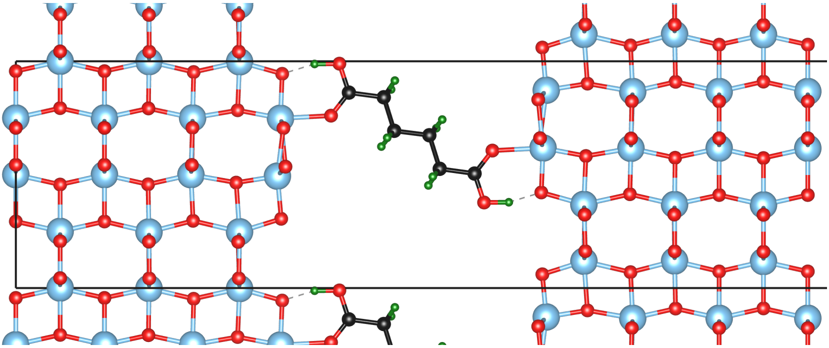

(b) quasi-bi-dentate (qbd) binding mode

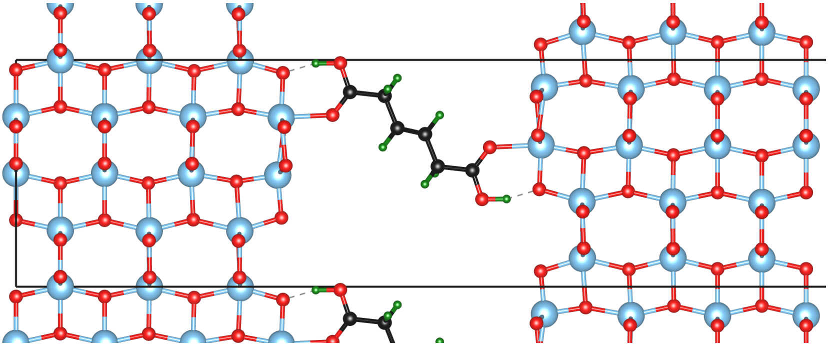

(c) qbd binding mode with a double bond between the third and fourth carbon atom

Figure D.6: Different binding modes of carboxylic acids on anatase TiO_2 (100) studied in Chapter 6. Colour code: Ti – blue, O – red, C – black, H – green.

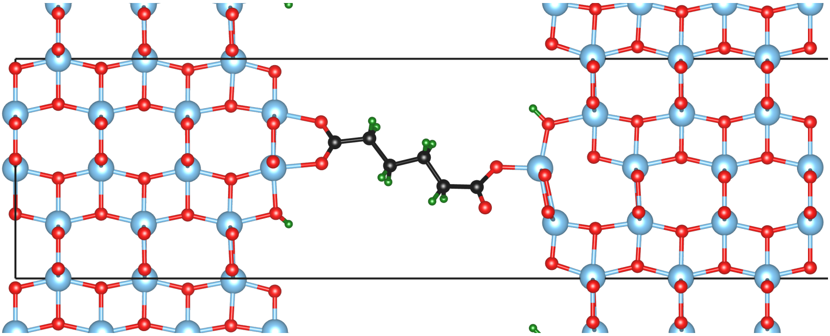

(a) failure of bi-dentate (bd) binding mode

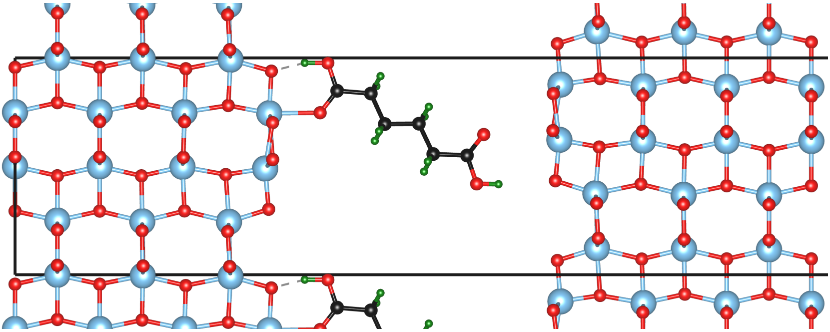

(b) failure of quasi-bi-dentate (qbd) binding mode

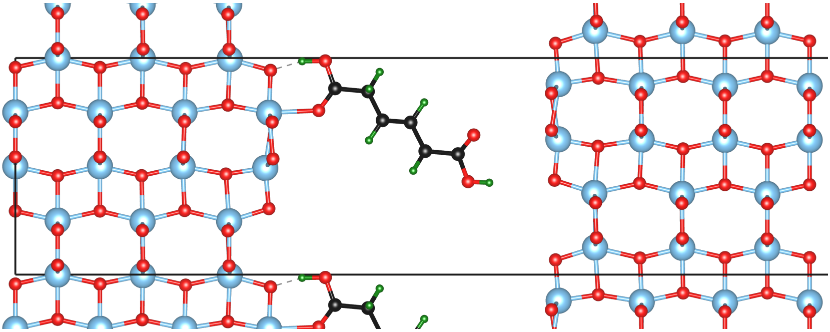

(c) failure of qbd binding mode with a double bond

Figure D.7: Different interface failure geometries of interfaces between anatase TiO_2 (100) and carboxylic acids studied in Chapter 6. Colour code: Ti – blue, O – red, C – black, H – green.

Bibliography

[1] R. Bhateria and R. Singh, "A Review on Nanotechnological Application of Magnetic Iron Oxides for Heavy Metal Removal", *Journal of Water Process Engineering* **31**, 100845 (2019), DOI: `10.1016/j.jwpe.2019.100845`.

[2] W. Wu, Z. Wu, T. Yu, et al., "Recent Progress on Magnetic Iron Oxide Nanoparticles: Synthesis, Surface Functional Strategies and Biomedical Applications", *Science and Technology of Advanced Materials* **16** (2), 023501 (2015), DOI: `10.1088/1468-6996/16/2/023501`.

[3] C. R. F. Lund, J. E. Kubsh, and J. A. Dumesic, "Water Gas Shift over Magnetite-Based Catalysts", in: *Solid State Chemistry in Catalysis*, ACS Symposium Series 279, American Chemical Society, 1985, pp. 313–338, DOI: `10.1021/bk-1985-0279.ch019`.

[4] K. R. P. M. Rao, F. E. Huggins, V. Mahajan, et al., "The Role of Magnetite in Fischer-Tropsch Synthesis", *Hyperfine Interactions* **93** (1), 1745–1749 (1994), DOI: `10.1007/BF02072939`.

[5] G. S. Parkinson, "Single-Atom Catalysis: How Structure Influences Catalytic Performance", *Catalysis Letters* **149** (5), 1137–1146 (2019), DOI: `10.1007/s10562-019-02709-7`.

[6] R. Bliem, J. Pavelec, O. Gamba, et al., "Adsorption and Incorporation of Transition Metals at the Magnetite Fe_3O_4 (001) Surface", *Physical Review B* **92** (7), 075440 (2015), DOI: `10.1103/PhysRevB.92.075440`.

[7] X. Chen and S. S. Mao, "Titanium Dioxide Nanomaterials: Synthesis, Properties, Modifications, and Applications", *Chemical Reviews* **107** (7), 2891–2959 (2007), DOI: `10.1021/cr0500535`.

[8] D. O. Scanlon, C. W. Dunnill, J. Buckeridge, et al., "Band Alignment of Rutile and Anatase TiO_2", *Nature Materials* **12** (9), 798–801 (2013), DOI: `10.1038/nmat3697`.

[9] A. Fujishima and K. Honda, "Electrochemical Photolysis of Water at a Semiconductor Electrode", *Nature* **238** (5358), 37 (1972), DOI: `10.1038/238037a0`.

[10] X. Chen, S. Shen, L. Guo, et al., "Semiconductor-Based Photocatalytic Hydrogen Generation", *Chemical Reviews* **110** (11), 6503–6570 (2010), DOI: `10.1021/cr1001645`.

[11] A. Fujishima, X. Zhang, and D. A. Tryk, "TiO_2 Photocatalysis and Related Surface Phenomena", *Surface Science Reports* **63** (12), 515–582 (2008), DOI: `10.1016/j.surfrep.2008.10.001`.

[12] M. Dilla, A. Jakubowski, S. Ristig, et al., "The Fate of O_2 in Photocatalytic CO_2 Reduction on TiO_2 under Conditions of Highest Purity", *Physical Chemistry Chemical Physics* **21** (29), 15949–15957 (2019), DOI: `10.1039/C8CP07765G`.

[13] S. U. M. Khan, M. Al-Shahry, and W. B. Ingler, "Efficient Photochemical Water Splitting by a Chemically Modified N-TiO_2", *Science* **297** (5590), 2243–2245 (2002), DOI: `10.1126/science.1075035`.

[14] L. DeRita, J. Resasco, S. Dai, et al., "Structural Evolution of Atomically Dispersed Pt Catalysts Dictates Reactivity", *Nature Materials* **18** (7), 746 (2019), DOI: `10.1038/s41563-019-0349-9`.

[15] J. Liu, M. Weng, S. Li, et al., "High-Throughput HSE Study on the Doping Effect in Anatase TiO_2", *Physical Chemistry Chemical Physics* (2019), DOI: `10.1039/C9CP04591K`.

[16] B. Domènech, M. Kampferbeck, E. Larsson, et al., "Hierarchical Supercrystalline Nanocomposites through the Self-Assembly of Organically-Modified Ceramic Nanoparticles", *Scientific Reports* **9** (1), 1–11 (2019), DOI: `10.1038/s41598-019-39934-4`.

[17] A. Dreyer, A. Feld, A. Kornowski, et al., "Organically Linked Iron Oxide Nanoparticle Supercrystals with Exceptional Isotropic Mechanical Properties", *Nature Materials* **15** (5), 522–528 (2016), DOI: `10.1038/nmat4553`.

[18] A. Hensel, C. J. Schröter, H. Schlicke, et al., "Elasticity of Cross-Linked Titania Nanocrystal Assemblies Probed by AFM-Bulge Tests", *Nanomaterials* **9** (9), 1230 (2019), DOI: `10.3390/nano9091230`.

[19] B. Domènech, A. Plunkett, M. Kampferbeck, et al., "Modulating the Mechanical Properties of Supercrystalline Nanocomposite Materials via Solvent–Ligand Interactions", *Langmuir* **35** (43), 13893–13903 (2019), DOI: `10.1021/acs.langmuir.9b01938`.

[20] D. Giuntini, E. Torresani, K. T. Chan, et al., "Iron Oxide-Based Nanostructured Ceramics with Tailored Magnetic and Mechanical Properties: Development of Mechanically Robust, Bulk Superparamagnetic Materials", *Nanoscale Advances* **1** (8), 3139–3150 (2019), DOI: `10.1039/C9NA00222G`.

[21] C. Kittel, *Introduction to Solid State Physics*, Wiley, 2004, 704 pp., ISBN: 978-0-471-41526-8.

[22] G. Gottstein, *Physical Foundations of Materials Science*, Springer Science & Business Media, 2013, 511 pp., ISBN: 978-3-662-09291-0.

[23] R. P. Feynman, R. B. Leighton, and M. Sands, *The Feynman Lectures on Physics, Vol. III: The New Millennium Edition: Quantum Mechanics*, Hachette UK, 2015, 799 pp., ISBN: 978-0-465-04083-4.

[24] A. Gross, *Theoretical Surface Science: A Microscopic Perspective*, 2nd ed, Springer (Berlin ; London), 2009, 342 pp., ISBN: 978-3-540-68966-9.

[25] P. Hohenberg and W. Kohn, "Inhomogeneous Electron Gas", *Physical Review* **136** (3B), B864–B871 (1964), DOI: `10.1103/PhysRev.136.B864`.

[26] W. Kohn and L. J. Sham, "Self-Consistent Equations Including Exchange and Correlation Effects", *Physical Review* **140** (4A), A1133–A1138 (1965), DOI: `10.1103/PhysRev.140.A1133`.

[27] D. M. Ceperley and B. J. Alder, "Ground State of the Electron Gas by a Stochastic Method", *Physical Review Letters* **45** (7), 566–569 (1980), DOI: `10.1103/PhysRevLett.45.566`.

[28] N. Mardirossian and M. Head-Gordon, "Thirty Years of Density Functional Theory in Computational Chemistry: An Overview and Extensive Assessment of 200 Density Functionals", *Molecular Physics* **115** (19), 2315–2372 (2017), DOI: `10.1080/00268976.2017.1333644`.

[29] M. Swart, M. Bickelhaupt, and M. Duran, *The Annual Popularity Poll for Density Functionals: Edition 2019*, URL: `https://www.marcelswart.eu/dft-poll/news2019.pdf` (visited on 09/24/2020).

[30] J. P. Perdew, K. Burke, and M. Ernzerhof, "Generalized Gradient Approximation Made Simple", *Physical Review Letters* **77** (18), 3865–3868 (1996), DOI: `10.1103/PhysRevLett.77.3865`.

[31] J. Sun, A. Ruzsinszky, and J. P. Perdew, "Strongly Constrained and Appropriately Normed Semilocal Density Functional", *Physical Review Letters* **115** (3), 036402 (2015), DOI: `10.1103/PhysRevLett.115.036402`.

[32] M. Dion, H. Rydberg, E. Schröder, et al., "Van Der Waals Density Functional for General Geometries", *Physical Review Letters* **92** (24), 246401 (2004), DOI: `10.1103/PhysRevLett.92.246401`.

[33] J. Klimeš, D. R. Bowler, and A. Michaelides, "Chemical Accuracy for the van Der Waals Density Functional", *Journal of Physics: Condensed Matter* **22** (2), 022201 (2010), DOI: `10.1088/0953-8984/22/2/022201`.

[34] J. Klimeš, D. R. Bowler, and A. Michaelides, "Van Der Waals Density Functionals Applied to Solids", *Physical Review B* **83** (19), 195131 (2011), DOI: `10.1103/PhysRevB.83.195131`.

[35] J. Hubbard, "Electron Correlations in Narrow Energy Bands", *Proceedings of the Royal Society of London A: Mathematical, Physical and Engineering Sciences* **276** (1365), 238–257 (1963), DOI: `10.1098/rspa.1963.0204`.

[36] G. Kresse and J. Furthmüller, “Efficiency of Ab-Initio Total Energy Calculations for Metals and Semiconductors Using a Plane-Wave Basis Set”, *Computational Materials Science* **6** (1), 15–50 (1996), DOI: `10.1016/0927-0256(96)00008-0`.

[37] G. Kresse and J. Furthmüller, “Efficient Iterative Schemes for Ab Initio Total-Energy Calculations Using a Plane-Wave Basis Set”, *Physical Review B* **54** (16), 11169–11186 (1996), DOI: `10.1103/PhysRevB.54.11169`.

[38] D. J. Singh and L. Nordstrom, *Planewaves, Pseudopotentials, and the LAPW Method*, 2nd ed., Springer US, 2006, DOI: `10.1007/978-0-387-29684-5`.

[39] P. E. Blöchl, “Projector Augmented-Wave Method”, *Physical Review B* **50** (24), 17953–17979 (1994), DOI: `10.1103/PhysRevB.50.17953`.

[40] P. Giannozzi and S. Baroni, “Density-Functional Perturbation Theory”, in: *Handbook of Materials Modeling*, Springer, Dordrecht, 2005, pp. 195–214, DOI: `10.1007/978-1-4020-3286-8_11`.

[41] M. Born and K. Huang, *Dynamical Theory of Crystal Lattices*, Oxford University Press (Oxford, New York), 1954, ISBN: 978-0-19-850369-9.

[42] X. Gonze and C. Lee, “Dynamical Matrices, Born Effective Charges, Dielectric Permittivity Tensors, and Interatomic Force Constants from Density-Functional Perturbation Theory”, *Physical Review B* **55** (16), 10355–10368 (1997), DOI: `10.1103/PhysRevB.55.10355`.

[43] T. Würger, W. Heckel, K. Sellschopp, et al., “Adsorption of Acetone on Rutile TiO_2: A DFT and FTIRS Study”, *The Journal of Physical Chemistry C* **122** (34), 19481–19490 (2018), DOI: `10.1021/acs.jpcc.8b04222`.

[44] J. Kiss, J. Frenzel, B. Meyer, et al., “Methanol Synthesis on ZnO($000\bar{1}$). II. Structure, Energetics, and Vibrational Signature of Reaction Intermediates”, *The Journal of Chemical Physics* **139** (4), 044705 (2013), DOI: `10.1063/1.4813404`.

[45] J. A. G. Torres, J. P. Götze, F. Grillo, et al., “Calculating the Frequencies and Intensities of Strongly Anharmonic Modes of Adsorbates on Surfaces: A Low-Cost but Accurate Computational Approach”, *Physical Review B* **100** (3), 035433 (2019), DOI: `10.1103/PhysRevB.100.035433`.

[46] V. Kapil, D. M. Wilkins, J. Lan, et al., “Inexpensive Modeling of Quantum Dynamics Using Path Integral Generalized Langevin Equation Thermostats”, *The Journal of Chemical Physics* **152** (12), 124104 (2020), DOI: `10.1063/1.5141950`.

[47] A. Michl, J. Weissmüller, and S. Müller, “Sign-Inverted Response of Aluminum Work Function to Tangential Strain”, *Journal of Physics: Condensed Matter* **25** (44), 445012 (2013), DOI: `10.1088/0953-8984/25/44/445012`.

[48] K. Takayanagi, Y. Tanishiro, S. Takahashi, et al., “Structure Analysis of Si(111)-7 x 7 Reconstructed Surface by Transmission Electron Diffraction”, *Surface Science* **164** (2), 367–392 (1985), DOI: `10.1016/0039-6028(85)90753-8`.

[49] U. Diebold, “The Surface Science of Titanium Dioxide”, *Surface Science Reports* **48** (5–8), 53–229 (2003), DOI: `10.1016/S0167-5729(02)00100-0`.

[50] K. Reuter and M. Scheffler, “Composition, Structure, and Stability of RuO_2(110) as a Function of Oxygen Pressure”, *Physical Review B* **65** (3), 035406 (2001), DOI: `10.1103/PhysRevB.65.035406`.

[51] M. W. Chase, “NIST-JANAF Thermochemical Tables, 4th Edition | NIST”, *NIST-JANAF Thermochemical Tables 2 Volume-Set (Journal of Physical and Chemical Reference Data Monographs)* (1998).

[52] G. Wulff, “XXV. Zur Frage Der Geschwindigkeit Des Wachsthums Und Der Auflösung Der Krystallflächen”, *Zeitschrift für Kristallographie - Crystalline Materials* **34** (1-6), 449–530 (1901), DOI: `10.1524/zkri.1901.34.1.449`.

[53] M. v. Laue, “Der Wulffsche Satz für die Gleichgewichtsform von Kristallen”, *Zeitschrift für Kristallographie - Crystalline Materials* **105** (1-6), 124–133 (1943), DOI: `10.1524/zkri.1943.105.1.124`.

[54] R. F. Strickland-Constable, *Kinetics and Mechanism of Crystallization*, Acad. Pr., 1968.

[55] R. Cerf, *The Wulff Crystal in Ising and Percolation Models: Ecole d’Eté de Probabilités de Saint-Flour XXXIV - 2004*, ed. by J. Picard, École d’Été de Probabilités de Saint-Flour, Springer-Verlag (Berlin Heidelberg), 2006, DOI: `10.1007/b128410`.

[56] A. Kawska, J. Brickmann, R. Kniep, et al., “An Atomistic Simulation Scheme for Modeling Crystal Formation from Solution”, *The Journal of Chemical Physics* **124** (2), 024513 (2006), DOI: `10.1063/1.2145677`.

[57] J. Anwar and D. Zahn, “Uncovering Molecular Processes in Crystal Nucleation and Growth by Using Molecular Simulation”, *Angewandte Chemie International Edition* **50** (9), 1996–2013 (2011), DOI: `10.1002/anie.201000463`.

[58] B. A. M. Elsner, “Einfluss von Carboxylgruppen Auf Die Stabilität von Hybridmaterialien”, Diplomarbeit, Technische Universität Hamburg (Hamburg), 2012, 61 pp.

[59] W. Heckel, “Funktionalisierung von Metalloxiden: Modellierung Auf Quantenmechanischer Basis”, Dissertation, Technische Universität Hamburg (Hamburg), 2015.

[60] F. H. Stillinger, “Exponential Multiplicity of Inherent Structures”, *Physical Review E* **59** (1), 48–51 (1999), DOI: `10.1103/PhysRevE.59.48`.

[61] C. J. Pickard and R. J. Needs, “High-Pressure Phases of Silane”, *Physical Review Letters* **97** (4), 045504 (2006), doi: `10.1103/PhysRevLett.97.045504`.

[62] C. J. Pickard and R. J. Needs, “Ab Initio Random Structure Searching”, *Journal of Physics: Condensed Matter* **23** (5), 053201 (2011), doi: `10.1088/0953-8984/23/5/053201`.

[63] C. J. Pickard and R. J. Needs, “Aluminium at Terapascal Pressures”, *Nature Materials* **9** (8), 624–627 (2010), doi: `10.1038/nmat2796`.

[64] C. J. Pickard and R. J. Needs, “Highly Compressed Ammonia Forms an Ionic Crystal”, *Nature Materials* **7** (10), 775–779 (2008), doi: `10.1038/nmat2261`.

[65] M.-H. Wu, W.-J. Chou, J.-S. Huang, et al., “First-Principles Investigation of the Hydrogen Evolution Reaction on Different Surfaces of Pyrites MnS_2, FeS_2, CoS_2, NiS_2”, *Physical Chemistry Chemical Physics* **21** (38), 21561–21567 (2019), doi: `10.1039/C9CP03893K`.

[66] D. B. Putungan, S.-H. Lin, C.-M. Wei, et al., “Li Adsorption, Hydrogen Storage and Dissociation Using Monolayer MoS_2: An Ab Initio Random Structure Searching Approach”, *Physical Chemistry Chemical Physics* **17** (17), 11367–11374 (2015), doi: `10.1039/C5CP00977D`.

[67] S. Deshpande, T. Maxson, and J. Greeley, “Graph Theory Approach to Determine Configurations of Multidentate and High Coverage Adsorbates for Heterogeneous Catalysis”, *npj Computational Materials* **6** (1), 1–6 (2020), doi: `10.1038/s41524-020-0345-2`.

[68] M. Todorović, M. U. Gutmann, J. Corander, et al., “Bayesian Inference of Atomistic Structure in Functional Materials”, *npj Computational Materials* **5** (1), 1–7 (2019), doi: `10.1038/s41524-019-0175-2`.

[69] J. Järvi, P. Rinke, and M. Todorović, “Detecting Stable Adsorbates of (1S)-Camphor on Cu(111) with Bayesian Optimization”, *Beilstein Journal of Nanotechnology* **11** (1), 1577–1589 (2020), doi: `10.3762/bjnano.11.140`.

[70] A. T. Egger, L. Hörmann, A. Jeindl, et al., “Charge Transfer into Organic Thin Films: A Deeper Insight through Machine-Learning-Assisted Structure Search”, *Advanced Science* **7** (15), 2000992 (2020), doi: `10.1002/advs.202000992`.

[71] S. Kirkpatrick, C. D. Gelatt, and M. P. Vecchi, “Optimization by Simulated Annealing”, *Science* **220** (4598), 671–680 (1983), doi: `10.1126/science.220.4598.671`.

[72] A. Laio and M. Parrinello, “Escaping Free-Energy Minima”, *Proceedings of the National Academy of Sciences* **99** (20), 12562–12566 (2002), doi: `10.1073/pnas.202427399`.

[73] S. Awasthi, V. Kapil, and N. N. Nair, “Sampling Free Energy Surfaces as Slices by Combining Umbrella Sampling and Metadynamics”, *Journal of Computational Chemistry* **37** (16), 1413–1424 (2016), doi: `10.1002/jcc.24349`.

[74] W. Heckel, T. Würger, S. Müller, et al., "Van Der Waals Interaction Really Matters: Energetics of Benzoic Acid on TiO_2 Rutile Surfaces", *The Journal of Physical Chemistry C* **121** (32), 17207–17214 (2017), DOI: `10.1021/acs.jpcc.7b03149`.

[75] D. Lerch, O. Wieckhorst, G. L. W. Hart, et al., "UNCLE: A Code for Constructing Cluster Expansions for Arbitrary Lattices with Minimal User-Input", *Modelling and Simulation in Materials Science and Engineering* **17** (5), 055003 (2009), DOI: `10.1088/0965-0393/17/5/055003`.

[76] F. Musil, A. Grisafi, A. P. Bartók, et al., *Physics-Inspired Structural Representations for Molecules and Materials*, 2021, URL: `http://arxiv.org/abs/2101.04673` (visited on 02/16/2021).

[77] A. C. Müller and S. Guido, *Introduction to Machine Learning with Python*, First edition, Python/Machine Learning, O'Reilly, 2016, ISBN: 978-1-4493-6941-5.

[78] A. Burkov, *The Hundred-Page Machine Learning Book*, Andriy Burkov, 2019, ISBN: 978-1-9995795-0-0.

[79] M. Lutz, *Learning Python*, 4th ed., O'Reilly, 2009, ISBN: 978-0-596-15806-4.

[80] A. Sadeghi, S. A. Ghasemi, B. Schaefer, et al., "Metrics for Measuring Distances in Configuration Spaces", *The Journal of Chemical Physics* **139** (18), 184118 (2013), DOI: `10.1063/1.4828704`.

[81] L. Himanen, A. Geurts, A. S. Foster, et al., "Data-Driven Materials Science: Status, Challenges, and Perspectives", *Advanced Science* **7** (2), 1903667 (2020), DOI: `10.1002/advs.201903667`.

[82] A. P. Bartók, R. Kondor, and G. Csányi, "On Representing Chemical Environments", *Physical Review B* **87** (18), 184115 (2013), DOI: `10.1103/PhysRevB.87.184115`.

[83] S. De, A. P. Bartók, G. Csányi, et al., "Comparing Molecules and Solids across Structural and Alchemical Space", *Physical Chemistry Chemical Physics* **18** (20), 13754–13769 (2016), DOI: `10.1039/C6CP00415F`.

[84] B. A. Helfrecht, R. K. Cersonsky, G. Fraux, et al., "Structure-Property Maps with Kernel Principal Covariates Regression", *Machine Learning: Science and Technology* **1** (4), 045021 (2020), DOI: `10.1088/2632-2153/aba9ef`.

[85] S. N. Pozdnyakov, M. J. Willatt, A. P. Bartók, et al., "Incompleteness of Atomic Structure Representations", *Physical Review Letters* **125** (16), 166001 (2020), DOI: `10.1103/PhysRevLett.125.166001`.

[86] F. Musil, S. De, J. Yang, et al., "Machine Learning for the Structure–Energy–Property Landscapes of Molecular Crystals", *Chemical Science* **9** (5), 1289–1300 (2018), DOI: `10.1039/C7SC04665K`.

[87] Y. Zuo, C. Chen, X. Li, et al., "Performance and Cost Assessment of Machine Learning Interatomic Potentials", *The Journal of Physical Chemistry A* **124** (4), 731–745 (2020), DOI: `10.1021/acs.jpca.9b08723`.

[88] F. Pietrucci and W. Andreoni, "Graph Theory Meets Ab Initio Molecular Dynamics: Atomic Structures and Transformations at the Nanoscale", *Physical Review Letters* **107** (8), 085504 (2011), DOI: `10.1103/PhysRevLett.107.085504`.

[89] M. Rupp, A. Tkatchenko, K.-R. Müller, et al., "Fast and Accurate Modeling of Molecular Atomization Energies with Machine Learning", *Physical Review Letters* **108** (5), 058301 (2012), DOI: `10.1103/PhysRevLett.108.058301`.

[90] J. Behler, "Atom-Centered Symmetry Functions for Constructing High-Dimensional Neural Network Potentials", *The Journal of Chemical Physics* **134** (7), 074106 (2011), DOI: `10.1063/1.3553717`.

[91] C. R. Harris, K. J. Millman, S. J. van der Walt, et al., "Array Programming with NumPy", *Nature* **585** (7825), 357–362 (2020), DOI: `10.1038/s41586-020-2649-2`.

[92] A. H. Larsen, J. J. Mortensen, J. Blomqvist, et al., "The Atomic Simulation Environment—a Python Library for Working with Atoms", *Journal of Physics: Condensed Matter* **29** (27), 273002 (2017), DOI: `10.1088/1361-648X/aa680e`.

[93] F. Musil, M. Veit, A. Goscinski, et al., "Efficient Implementation of Atom-Density Representations", *The Journal of Chemical Physics* **154** (11), 114109 (2021), DOI: `10.1063/5.0044689`.

[94] F. Pedregosa, G. Varoquaux, A. Gramfort, et al., "Scikit-Learn: Machine Learning in Python", *Journal of Machine Learning Research* **12** (85), 2825–2830 (2011).

[95] I. Lung, M. Stan, O. Opris, et al., "Removal of Lead(II), Cadmium(II), and Arsenic(III) from Aqueous Solution Using Magnetite Nanoparticles Prepared by Green Synthesis with Box–Behnken Design", *Analytical Letters* **51** (16), 2517–2529 (2018), DOI: `10.1080/00032719.2018.1446974`.

[96] H. J. Krebs, H. P. Bonzel, W. Schwarting, et al., "Microreactor and Electron Spectroscopy Studies of Fischer-Tropsch Synthesis on Magnetite", *Journal of Catalysis* **72** (2), 199–209 (1981), DOI: `10.1016/0021-9517(81)90002-6`.

[97] B. Arndt, K. Sellschopp, M. Creutzburg, et al., "Carboxylic Acid Induced Near-Surface Restructuring of a Magnetite Surface", *Communications Chemistry* **2** (1), 1–8 (2019), DOI: `10.1038/s42004-019-0197-1`.

[98] M. Creutzburg, K. Sellschopp, S. Tober, et al., “Heterogeneous Adsorption and Local Ordering of Formate on a Magnetite Surface”, *The Journal of Physical Chemistry Letters* **12** (15), 3837–3852 (2021), DOI: `10.1021/acs.jpclett.1c00209`.

[99] E. J. W. Verwey, “Electronic Conduction of Magnetite (Fe_3O_4) and Its Transition Point at Low Temperatures”, *Nature* **144** (3642), 327–328 (1939), DOI: `10.1038/144327b0`.

[100] Z. Zhang and S. Satpathy, “Electron States, Magnetism, and the Verwey Transition in Magnetite”, *Physical Review B* **44** (24), 13319–13331 (1991), DOI: `10.1103/PhysRevB.44.13319`.

[101] J. G. Tobin, S. A. Morton, S. W. Yu, et al., “Spin Resolved Photoelectron Spectroscopy of Fe_3O_4: The Case against Half-Metallicity”, *Journal of Physics: Condensed Matter* **19** (31), 315218 (2007), DOI: `10.1088/0953-8984/19/31/315218`.

[102] H. Liu and C. Di Valentin, “Band Gap in Magnetite above Verwey Temperature Induced by Symmetry Breaking”, *The Journal of Physical Chemistry C* **121** (46), 25736–25742 (2017), DOI: `10.1021/acs.jpcc.7b09387`.

[103] F. Walz, “The Verwey Transition - a Topical Review”, *Journal of Physics: Condensed Matter* **14** (12), R285 (2002), DOI: `10.1088/0953-8984/14/12/203`.

[104] G. Perversi, J. Cumby, E. Pachoud, et al., “The Verwey Structure of a Natural Magnetite”, *Chemical Communications* **52** (27), 4864–4867 (2016), DOI: `10.1039/C5CC10495E`.

[105] K. E. Sickafus, J. M. Wills, and N. W. Grimes, “Structure of Spinel”, *Journal of the American Ceramic Society* **82** (12), 3279–3292 (1999), DOI: `10.1111/j.1151-2916.1999.tb02241.x`.

[106] E. Goering, S. Gold, M. Lafkioti, et al., “Vanishing Fe 3d Orbital Moments in Single-Crystalline Magnetite”, *EPL (Europhysics Letters)* **73** (1), 97 (2005), DOI: `10.1209/epl/i2005-10359-8`.

[107] Y. Meng, X.-W. Liu, C.-F. Huo, et al., “When Density Functional Approximations Meet Iron Oxides”, *Journal of Chemical Theory and Computation* **12** (10), 5132–5144 (2016), DOI: `10.1021/acs.jctc.6b00640`.

[108] M. Meier, Z. Jakub, J. Balajka, et al., “Probing the Geometry of Copper and Silver Adatoms on Magnetite: Quantitative Experiment versus Theory”, *Nanoscale* **10** (5), 2226–2230 (2018), DOI: `10.1039/C7NR07319D`.

[109] R. M. Cornell and U. Schwertmann, *The Iron Oxides: Structure, Properties, Reactions, Occurrences, and Uses*, 2nd, completely rev. and extended ed, Wiley-VCH (Weinheim), 2003, 664 pp., ISBN: 978-3-527-30274-1.

[110] J. Noh, O. I. Osman, S. G. Aziz, et al., "A Density Functional Theory Investigation of the Electronic Structure and Spin Moments of Magnetite", *Science and Technology of Advanced Materials* **15** (4), 044202 (2014), DOI: `10.1088/1468-6996/15/4/044202`.

[111] A. Feld, A. Weimer, A. Kornowski, et al., "Chemistry of Shape-Controlled Iron Oxide Nanocrystal Formation", *ACS Nano* (2018), DOI: `10.1021/acsnano.8b05032`.

[112] G. S. Parkinson, "Iron Oxide Surfaces", *Surface Science Reports* **71** (1), 272–365 (2016), DOI: `10.1016/j.surfrep.2016.02.001`.

[113] R. Pentcheva, F. Wendler, H. L. Meyerheim, et al., "Jahn-Teller Stabilization of a "Polar" Metal Oxide Surface: $Fe_3O_4(001)$", *Physical Review Letters* **94** (12), 126101 (2005), DOI: `10.1103/PhysRevLett.94.126101`.

[114] M. Fonin, R. Pentcheva, Y. S. Dedkov, et al., "Surface Electronic Structure of the $Fe_3O_4(100)$: Evidence of a Half-Metal to Metal Transition", *Physical Review B* **72** (10), 104436 (2005), DOI: `10.1103/PhysRevB.72.104436`.

[115] G. Tarrach, D. Bürgler, T. Schaub, et al., "Atomic Surface Structure of $Fe_3O_4(001)$ in Different Preparation Stages Studied by Scanning Tunneling Microscopy", *Surface Science* **285** (1), 1–14 (1993), DOI: `10.1016/0039-6028(93)90908-3`.

[116] B. Stanka, W. Hebenstreit, U. Diebold, et al., "Surface Reconstruction of $Fe_3O_4(001)$", *Surface Science* **448** (1), 49–63 (2000), DOI: `10.1016/S0039-6028(99)01182-6`.

[117] R. Pentcheva, W. Moritz, J. Rundgren, et al., "A Combined DFT/LEED-Approach for Complex Oxide Surface Structure Determination: Fe_3O_4 (001)", *Surface Science* **602** (7), 1299–1305 (2008).

[118] R. Bliem, E. McDermott, P. Ferstl, et al., "Subsurface Cation Vacancy Stabilization of the Magnetite (001) Surface", *Science* **346** (6214), 1215–1218 (2014), DOI: `10.1126/science.1260556`.

[119] M. Meier, J. Hulva, Z. Jakub, et al., "Water Agglomerates on Fe_3O_4 (001)", *Proceedings of the National Academy of Sciences*, 201801661 (2018), DOI: `10.1073/pnas.1801661115`.

[120] O. Gamba, J. Hulva, J. Pavelec, et al., "The Role of Surface Defects in the Adsorption of Methanol on $Fe_3O_4(001)$", *Topics in Catalysis* **60** (6-7), 420–430 (2017), DOI: `10.1007/s11244-016-0713-9`.

[121] M. Sun, D. Zheng, X. Wang, et al., "Electric Field Tunable Magnetism at C_6H_6-Adsorbed $Fe_3O_4(001)$ Surface", *The Journal of Physical Chemistry C* **121** (9), 5178–5184 (2017), DOI: `10.1021/acs.jpcc.7b00617`.

[122] J. Pavelec, J. Hulva, D. Halwidl, et al., "A Multi-Technique Study of CO_2 Adsorption on Fe_3O_4 Magnetite", *The Journal of Chemical Physics* **146** (1), 014701 (2017), DOI: `10.1063/1.4973241`.

[123] J. Hulva, Z. Jakub, Z. Novotny, et al., “Adsorption of CO on the Fe_3O_4(001) Surface”, *The Journal of Physical Chemistry B* **122** (2), 721–729 (2018), DOI: `10.1021/acs.jpcb.7b06349`.

[124] Z. Li, M. Jibran, X. Sun, et al., “Enhancement of the Spin Polarization of an Fe_3O_4(100) Surface by Nitric Oxide Adsorption”, *Physical Chemistry Chemical Physics* (2018), DOI: `10.1039/C8CP02361A`.

[125] A. Kiejna, T. Ossowski, and T. Pabisiak, “Surface Properties of the Clean and Au/Pd Covered Fe_3O_4(111): DFT and DFT+U Study”, *Physical Review B* **85** (12), 125414 (2012), DOI: `10.1103/PhysRevB.85.125414`.

[126] J. Noh, O. I. Osman, S. G. Aziz, et al., “Magnetite Fe_3O_4 (111) Surfaces: Impact of Defects on Structure, Stability, and Electronic Properties”, *Chemistry of Materials* **27** (17), 5856–5867 (2015), DOI: `10.1021/acs.chemmater.5b02885`.

[127] Y. Liu, Z. Wu, M. Naschitzki, et al., “Elucidating Surface Structure with Action Spectroscopy”, *Journal of the American Chemical Society* **142** (5), 2665–2671 (2020), DOI: `10.1021/jacs.9b13164`.

[128] O. Gamba, H. Noei, J. Pavelec, et al., “Adsorption of Formic Acid on the Fe_3O_4(001) Surface”, *The Journal of Physical Chemistry C* **119** (35), 20459–20465 (2015), DOI: `10.1021/acs.jpcc.5b05560`.

[129] M. Kurahashi, X. Sun, and Y. Yamauchi, “Recovery of the Half-Metallicity of an Fe_3O_4(100) Surface by Atomic Hydrogen Adsorption”, *Physical Review B* **81** (19), 193402 (2010), DOI: `10.1103/PhysRevB.81.193402`.

[130] G. S. Parkinson, N. Mulakaluri, Y. Losovyj, et al., “Semiconductor–Half Metal Transition at the Fe_3O_4(001) Surface upon Hydrogen Adsorption”, *Physical Review B* **82** (12), 125413 (2010), DOI: `10.1103/PhysRevB.82.125413`.

[131] X. Sun, M. Kurahashi, A. Pratt, et al., “First-Principles Study of Atomic Hydrogen Adsorption on Fe_3O_4(100)”, *Surface Science* **605** (11–12), 1067–1073 (2011), DOI: `10.1016/j.susc.2011.03.006`.

[132] N. Mulakaluri and R. Pentcheva, “Hydrogen Adsorption and Site-Selective Reduction of the Fe_3O_4(001) Surface: Insights From First Principles”, *The Journal of Physical Chemistry C* **116** (31), 16447–16453 (2012), DOI: `10.1021/jp302259d`.

[133] N. Mulakaluri, R. Pentcheva, and M. Scheffler, “Coverage-Dependent Adsorption Mode of Water on Fe_3O_4(001): Insights from First Principles Calculations”, *The Journal of Physical Chemistry C* **114** (25), 11148–11156 (2010), DOI: `10.1021/jp100344n`.

[134] C. L. Muhich, V. J. Aston, R. M. Trottier, et al., “First-Principles Analysis of Cation Diffusion in Mixed Metal Ferrite Spinels”, *Chemistry of Materials* **28** (1), 214–226 (2016), DOI: `10.1021/acs.chemmater.5b03911`.

[135] J. Chao and B. J. Zwolinski, "Ideal Gas Thermodynamic Properties of Methanoic and Ethanoic Acids", *Journal of Physical and Chemical Reference Data* **7** (1), 363–377 (1978), doi: `10.1063/1.555571`.

[136] G. Righi and R. Magri, "Reduction and Oxidation of Maghemite (001) Surfaces: The Role of Iron Vacancies", *The Journal of Physical Chemistry C* **123** (25), 15648–15658 (2019), doi: `10.1021/acs.jpcc.9b03657`.

[137] S. Tober, M. Creutzburg, B. Arndt, et al., "Observation of Iron Diffusion in the Near-Surface Region of Magnetite at 470 K", *Physical Review Research* **2** (2), 023406 (2020), doi: `10.1103/PhysRevResearch.2.023406`.

[138] R. S. Cutting, C. A. Muryn, G. Thornton, et al., "Molecular Scale Investigations of the Reactivity of Magnetite with Formic Acid, Pyridine, and Carbon Tetrachloride", *Geochimica et Cosmochimica Acta* **70** (14), 3593–3612 (2006), doi: `10.1016/j.gca.2006.04.034`.

[139] M. Buchholz, Q. Li, H. Noei, et al., "The Interaction of Formic Acid with Zinc Oxide: A Combined Experimental and Theoretical Study on Single Crystal and Powder Samples", *Topics in Catalysis* **58** (2-3), 174–183 (2015), doi: `10.1007/s11244-014-0356-7`.

[140] G. Tabacchi, M. Fabbiani, L. Mino, et al., "The Case of Formic Acid on Anatase TiO_2(101): Where Is the Acid Proton?", *Angewandte Chemie International Edition* **58** (36), 12431–12434 (2019), doi: `10.1002/anie.201906709`.

[141] X.-Q. Gong, A. Selloni, and A. Vittadini, "Density Functional Theory Study of Formic Acid Adsorption on Anatase TiO_2(001): Geometries, Energetics, and Effects of Coverage, Hydration, and Reconstruction", *The Journal of Physical Chemistry B* **110** (6), 2804–2811 (2006), doi: `10.1021/jp056572t`.

[142] W.-K. Li, X.-Q. Gong, G. Lu, et al., "Different Reactivities of TiO_2 Polymorphs: Comparative DFT Calculations of Water and Formic Acid Adsorption at Anatase and Brookite TiO_2 Surfaces", *The Journal of Physical Chemistry C* **112** (17), 6594–6596 (2008), doi: `10.1021/jp802335h`.

[143] M. Konuk, K. Sellschopp, G. B. Vonbun-Feldbauer, et al., "Modeling Charge Redistribution at Magnetite Interfaces in Empirical Force Fields", *The Journal of Physical Chemistry C* **125** (8), 4794–4805 (2021), doi: `10.1021/acs.jpcc.0c10338`.

[144] A. Vittadini, M. Casarin, and A. Selloni, "Chemistry of and on TiO_2-Anatase Surfaces by DFT Calculations: A Partial Review", *Theoretical Chemistry Accounts* **117** (5), 663–671 (2007), doi: `10.1007/s00214-006-0191-4`.

[145] H. G. Yang, C. H. Sun, S. Z. Qiao, et al., "Anatase TiO_2 Single Crystals with a Large Percentage of Reactive Facets", *Nature* **453** (7195), 638–641 (2008), doi: `10.1038/nature06964`.

[146] B. Weise, K. Sellschopp, M. Bierdel, et al., "Anisotropic Thermal Conductivity in Epoxy-Bonded Magnetocaloric Composites", *Journal of Applied Physics* **120** (12), 125103 (2016), DOI: `10.1063/1.4962972`.

[147] K. Sellschopp, W. Heckel, J. Gäding, et al., "Shape-Controlling Effects of Hydrohalic and Carboxylic Acids in TiO_2 Nanoparticle Synthesis", *The Journal of Chemical Physics* **152** (6), 064702 (2020), DOI: `10.1063/1.5138717`.

[148] D. Reyes-Coronado, G. Rodríguez-Gattorno, M. E. Espinosa-Pesqueira, et al., "Phase-Pure TiO_2 Nanoparticles: Anatase, Brookite and Rutile", *Nanotechnology* **19** (14), 145605 (2008), DOI: `10.1088/0957-4484/19/14/145605`.

[149] T. R. Gordon, M. Cargnello, T. Paik, et al., "Nonaqueous Synthesis of TiO_2 Nanocrystals Using TiF_4 to Engineer Morphology, Oxygen Vacancy Concentration, and Photocatalytic Activity", *Journal of the American Chemical Society* **134** (15), 6751–6761 (2012), DOI: `10.1021/ja300823a`.

[150] Y. Zhang, J. W. Furness, B. Xiao, et al., "Subtlety of TiO_2 Phase Stability: Reliability of the Density Functional Theory Predictions and Persistence of the Self-Interaction Error", *The Journal of Chemical Physics* **150** (1), 014105 (2019), DOI: `10.1063/1.5055623`.

[151] P. D. Cozzoli, A. Kornowski, and H. Weller, "Low-Temperature Synthesis of Soluble and Processable Organic-Capped Anatase TiO_2 Nanorods", *Journal of the American Chemical Society* **125** (47), 14539–14548 (2003), DOI: `10.1021/ja036505h`.

[152] M.-H. Yang, P.-C. Chen, M.-C. Tsai, et al., "Alkali Metal Ion Assisted Synthesis of Faceted Anatase TiO_2", *CrystEngComm* **15** (15), 2966–2971 (2013), DOI: `10.1039/C3CE26965E`.

[153] M. Lazzeri, A. Vittadini, and A. Selloni, "Structure and Energetics of Stoichiometric TiO_2 Anatase Surfaces", *Physical Review B* **63** (15), 155409 (2001), DOI: `10.1103/PhysRevB.63.155409`.

[154] M. Lazzeri and A. Selloni, "Stress-Driven Reconstruction of an Oxide Surface: The Anatase TiO_2(001)-(1 x 4) Surface", *Physical Review Letters* **87** (26), 266105 (2001), DOI: `10.1103/PhysRevLett.87.266105`.

[155] W. J. I. DeBenedetti, E. S. Skibinski, D. Jing, et al., "Atomic-Scale Understanding of Catalyst Activation: Carboxylic Acid Solutions, but Not the Acid Itself, Increase the Reactivity of Anatase (001) Faceted Nanocatalysts", *The Journal of Physical Chemistry C* **122** (8), 4307–4314 (2018), DOI: `10.1021/acs.jpcc.7b11054`.

[156] Y. Wang, H. Zhang, Y. Han, et al., "A Selective Etching Phenomenon on {001} Faceted Anatase Titanium Dioxide Single Crystal Surfaces by Hydrofluoric Acid", *Chemical Communications* **47** (10), 2829–2831 (2011), DOI: `10.1039/C0CC04848H`.

[157] Z. Lai, F. Peng, Y. Wang, et al., "Low Temperature Solvothermal Synthesis of Anatase TiO_2 Single Crystals with Wholly {100} and {001} Faceted Surfaces", *Journal of Materials Chemistry* **22** (45), 23906–23912 (2012), DOI: `10.1039/C2JM34880B`.

[158] B. Zhang, F. Wei, Q. Wu, et al., "Formation and Evolution of the High-Surface-Energy Facets of Anatase TiO_2", *The Journal of Physical Chemistry C* **119** (11), 6094–6100 (2015), DOI: `10.1021/acs.jpcc.5b00087`.

[159] L. Wu, B. X. Yang, X. H. Yang, et al., "On the Synergistic Effect of Hydrohalic Acids in the Shape-Controlled Synthesis of Anatase TiO_2 Single Crystals", *CrystEngComm* **15** (17), 3252–3255 (2013), DOI: `10.1039/C2CE26744F`.

[160] S. Selçuk and A. Selloni, "Surface Structure and Reactivity of Anatase TiO_2 Crystals with Dominant {001} Facets", *The Journal of Physical Chemistry C* **117** (12), 6358–6362 (2013), DOI: `10.1021/jp402100v`.

[161] J. Balajka, M. A. Hines, W. J. I. DeBenedetti, et al., "High-Affinity Adsorption Leads to Molecularly Ordered Interfaces on TiO_2 in Air and Solution", *Science* **361** (6404), 786–789 (2018), DOI: `10.1126/science.aat6752`.

[162] M. Li, I. Scheider, B. Bor, et al., "Ultra-Thin and Ultra-Strong Organic Interphase in Nanocomposites with Supercrystalline Particle Arrangement: Mechanical Behavior Identification via Multiscale Numerical Modeling", *Composites Science and Technology*, 108283 (2020), DOI: `10.1016/j.compscitech.2020.108283`.

[163] T. Stauch and A. Dreuw, "Advances in Quantum Mechanochemistry: Electronic Structure Methods and Force Analysis", *Chemical Reviews* **116** (22), 14137–14180 (2016), DOI: `10.1021/acs.chemrev.6b00458`.

[164] M. K. Beyer, "The Mechanical Strength of a Covalent Bond Calculated by Density Functional Theory", *The Journal of Chemical Physics* **112** (17), 7307–7312 (2000), DOI: `10.1063/1.481330`.

[165] P. Vélez, S. A. Dassie, and E. P. M. Leiva, "First Principles Calculations of Mechanical Properties of 4,4'-Bipyridine Attached to Au Nanowires", *Physical Review Letters* **95** (4), 045503 (2005), DOI: `10.1103/PhysRevLett.95.045503`.

[166] J. Ribas-Arino, M. Shiga, and D. Marx, "Understanding Covalent Mechanochemistry", *Angewandte Chemie International Edition* **48** (23), 4190–4193 (2009), DOI: `10.1002/anie.200900673`.

[167] G. Feldbauer, M. Wolloch, P. O. Bedolla, et al., "Adhesion and Material Transfer between Contacting Al and TiN Surfaces from First Principles", *Physical Review B* **91** (16), 165413 (2015), DOI: `10.1103/PhysRevB.91.165413`.

[168] K. Lee, É. D. Murray, L. Kong, et al., "Higher-Accuracy van Der Waals Density Functional", *Physical Review B* **82** (8), 081101 (2010), DOI: `10.1103/PhysRevB.82.081101`.

[169] A. Tkatchenko and M. Scheffler, “Accurate Molecular Van Der Waals Interactions from Ground-State Electron Density and Free-Atom Reference Data”, *Physical Review Letters* **102** (7), 073005 (2009), DOI: `10.1103/PhysRevLett.102.073005`.

[170] S. Grimme, “Semiempirical GGA-type density functional constructed with a long-range dispersion correction”, *Journal of Computational Chemistry* **27** (15), 1787–1799 (2006), DOI: `10.1002/jcc.20495`.

[171] S. Grimme, J. Antony, S. Ehrlich, et al., “A Consistent and Accurate Ab Initio Parametrization of Density Functional Dispersion Correction (DFT-D) for the 94 Elements H-Pu”, *The Journal of Chemical Physics* **132** (15), 154104 (2010), DOI: `10.1063/1.3382344`.

[172] S. L. Dudarev, G. A. Botton, S. Y. Savrasov, et al., “Electron-Energy-Loss Spectra and the Structural Stability of Nickel Oxide: An LSDA+U Study”, *Physical Review B* **57** (3), 1505–1509 (1998), DOI: `10.1103/PhysRevB.57.1505`.

[173] R. F. W. Bader, A. Larouche, C. Gatti, et al., “Properties of Atoms in Molecules: Dipole Moments and Transferability of Properties”, *The Journal of Chemical Physics* **87** (2), 1142–1152 (1987), DOI: `10.1063/1.453294`.

Acknowledgements

Anyone who has ever written a thesis knows that it is hard work. Fortunately, I had supporters all along the way to get me through. Here, I would like to thank all of them. Making a comprehensive list of all the people that were there is very difficult though. So, ahead of all the other acknowledgements, here is a big thank you to everyone who I might have forgotten to mention.

First of all, I would like to thank my parents – *Anschela, Jürgen, and Claudia* – who did not only raise me, but also supported me all my life with their wisdom, money, and open arms. Then, of course, I would also like to thank my partner *Megan*, who had to endure my roller-coaster of emotions during the writing process and when dealing with all the organisational hurdles. English has almost become a second native language to me because of her, and writing in a global pandemic would have been a much bigger struggle without her love, encouragement, and incredible cakes.

Special thanks also go out to *Dr. Gregor Vonbun-Feldbauer*, who has led my research project, connected me to other experts, encouraged me to keep developing, and provided me with valuable feedback on the way. He was always there when needed, even if it was not about science, and at the same time provided the space and freedom to develop my own independent identity as a researcher.

As part of the Institute of Advanced Ceramics (M-9), led by *Prof. Gerold Schneider*, I had plenty of awesome colleagues. From the many people that I had the pleasure to work with at the institute, I would like to especially thank my office mates and tea buddies *Wernfried, Trixi, Tim, Sandra, Ludwig, and Anja* for everything they taught me (not only about tea) and the lively discussions we had (also not restricted to tea). Furthermore, I want to thank the students that I supervised – *Johannes, Franck, Aykut, Shreyas, and Somak* – for bringing some of my ideas to life and filling them with interesting science as well as their own ideas. I will always remember the regular coffee break foosball[1] matches with *Pia, Manfred, Anja, Ben, Hans, and Rolf* as well as the barbecues with grill master *Alex* at the pond. I also enjoyed exchanging the latest science, gossip, and funny animal pictures with *Yen, Berta, Diletta, Kaline, Büsra, and Jasmin* over coffee and cake, and I am thankful for all the help with organisational matters from *Sophia, Susanne, Andrea, and Bärbel.*

---

[1] also known as Kicker, Baby-Foot or Table Soccer

The work in this thesis was performed in a collaborative research centre, which made it possible to go beyond a pure theoretical picture. In this regard I want to thank the people from DESY – *Dr. Björn Arndt, Dr. Marcus Creutzburg, Dr. Heshmat Noei, and Prof. Andreas Stierle* – not only for performing surface science experiments that are directly comparable to my simulations, but also for asking the right questions and pushing for more insight. Furthermore, I would like to thank the group of *Prof. Horst Weller* at the University of Hamburg – especially *Clemens Schröter* and *Dr. Tobias Vossmeyer* – for always striving to acquire more precise data, even when that meant repeating several experiments.

Apart from the experimental collaborations, theoretical partners worked with me to bridge the scales. Here, I would like to thank *Prof. Robert Meißner* from TUHH, who seems to be a never-ending source of ideas and also became a reviewer for this thesis. Furthermore, *Dr. Mine Konuk* for her effort to create a more reliable force-field for magnetite, and *Dr. Ingo Scheider* from HZG, who managed to wrap his head around my idealised models and include their results into his continuum mechanics simulations.

The inclusion into the collaborative research centre also came with a graduate school (MGK), which was amazingly organized – first by *Dr. Ulrike Herzog* and *Dr. Alette Winter*, and later by *Dr. Nils Gayer* and *Dr. Layla Tulimat.* I want to thank all the MGK participants, who created insightful tutorials and made our annual summer schools and Christmas parties the amazing events that they were. With the help of the MGK I also went to Switzerland for a research visit to the COSMO lab of *Prof. Michele Ceriotti* at EPFL. I also want to thank him and the members of his group for the very welcoming atmosphere there, and making that visit a great experience.

Finally, I want to thank *Prof. Stefan Müller* for supervising my thesis, for trusting me to take over some of the teaching, and giving recommendations whenever I needed them, as well as my other reviewers and examiners *Prof. Robert Meißner* and *Prof. Lucio Colombi Ciacchi*, for keeping up a friendly atmosphere even during an examination.